

# The ADRIA Proposal

March 1992

ISTITUTO NAZIONALE DI FISICA NUCLEARE  
LABORATORI NAZIONALI DI LEGNARO

---

Via Romea 4 I-35020 Legnaro (Padova)

# The ADRIA Proposal

March 1992

ISTITUTO NAZIONALE DI FISICA NUCLEARE  
LABORATORI NAZIONALI DI LEGNARO

---

Via Romea 4 I-35020 Legnaro (Padova)

# Contents

## Preface

## Part A: The Physics Case for ADRIA

### 1. Heavy Ion Physics at 1-2 GeV/u

#### 1.1 Introduction

#### 1.2 Grazing Collisions

##### 1.2.1 General Considerations

##### 1.2.2 Coulomb Excitation

##### 1.2.3 Study of Extreme Configurations

#### 1.3 Energy Evolution of Central Collisions

##### 1.3.1 Characterizing the Transition from Low to Intermediate Energies

##### 1.3.2 Multifragmentation

##### 1.3.3 High Density Nuclear Matter and Particle Production

#### 1.4 The Intermediate Energy Regime

##### 1.4.1 Preliminary Considerations

##### 1.4.2 Evolution from Deep Inelastic to Multifragmentation

##### 1.4.3 Stability Limits in Energy and Angular Momentum

##### 1.4.4 Bulk Properties of Nuclear Matter and EOS

#### 1.5 Sub-threshold Particle Production

### 2. Physics with Unstable Ion Beams

#### 2.1 Introduction

#### 2.2 Nuclear Structure

##### 2.2.1 General Considerations

##### 2.2.2 Neutron-rich Region. Neutron "Halos"

##### 2.2.3 Study of Giant Resonances in the "Halo" Nuclei

##### 2.2.4 Exotic Decays

##### 2.2.5 Nuclear Spectroscopy Far from Stability

2.2.6 The Structure of Proton-rich Nuclei: the  $N=Z$  Nuclei

2.2.7 Exotic Shapes

2.2.8 New Regions of Deformation Close to the Proton Drip-line

2.2.9 The Nuclear Shell Structure Far from Stability

## 2.3 Nuclear Reactions

2.3.1 General Considerations

2.3.2 Fusion around and below the Coulomb Barrier

2.3.3 Transfer and Deep Inelastic Reactions

2.3.4 Elastic Scattering and the Nuclear Potential

2.3.5 Spin Distributions

## References

## Part B: Medical and Applied Physics with ADRIA

### 1. Therapy with Heavy Charged Particles

#### 1.1 Introduction

#### 1.2 Status of Conventional Radiotherapy

#### 1.3 Heavy Charged Particles Therapy

#### 1.4 Technical Set-up

#### 1.5 Layout of a Treatment Cave

#### 1.6 Perspective of Radiotherapy for the ADRIA Project

#### 1.7 Summary

### 2. Heavy Ion High Energy Beams in Applied Physics

# Part C: The ADRIA Technical Proposal

## 1. General Overview

- 1.1 The ADRIA Complex
- 1.2 Heavy Ion Source
- 1.3 Injection and Acceleration in the Booster
- 1.4 Fragment Production and Accumulation

## 2. Injector

- 2.1 Heavy Ion Injector
- 2.2 The Transfer Line (ITL) between ALPI and the Booster

## 3. Booster Ring

- 3.1 Lattice and General Layout
- 3.2 Injection
- 3.3 Extraction
- 3.4 The Magnet System
- 3.5 Power Supply
- 3.6 The rf System
- 3.7 The Vacuum System
- 3.8 Diagnostics and Instrumentation

## 4. Fragment Production & Transfer Line

- 4.1 Secondary Beam Production
- 4.2 Targetry
- 4.3 Design of the Transfer Line

## 5. Decelerator Ring

- 5.1 Lattice and Operation Cycle
- 5.2 Injection
- 5.3 Extraction
- 5.4 The Magnet System
- 5.5 Power Supply
- 5.6 The rf System
- 5.7 The Vacuum System
- 5.8 Diagnostics and Instrumentation
- 5.9 Cooling Techniques

## 6. Control System

### 6.1 Control Requirements

### 6.2 System Implementation

## 7. Civil Engineering

### 7.1 Tunnel Enclosure

### 7.2 Experimental Area

### 7.3 Utilities

## 8. Radiation Protection

### 8.1 Active Shielding

### 8.2 Induced Radioactivity

### 8.3 Radiation Damage

### 8.4 Other Risks

## 9. Cost Estimate and Schedule

### 9.1 Cost Estimate of the ADRIA Project

### 9.2 Time Schedule for Construction

### 9.3 Accelerator R&D Program

## Appendix: Acceleration of Protons

# Preface

This is a proposal for construction of the ADRIA complex on the site of the Laboratori Nazionali di Legnaro.

With the completion of the construction and the start of the operation of the ALPI post-accelerator, beams of heavy ions will be available with a broad range of energies, intensities and charge state from deuterium to uranium. As a natural upgrading of the facility, it is proposed here to build two circular accelerators with the circumference of 267 m and a magnetic rigidity of 22.25 Tm. The first accelerator can deliver beams of heavy ions with specific kinetic energies up to a few GeV/u, e.g. 1 GeV/u for Gold ions and 2.5 GeV/u for lighter ones. The repetition rate of the magnetic cycle has been fixed to 10Hz and the achievable beam intensities are about  $10^{12}$  ions per second.

In addition to the normal mode of operation, where the primary beam is sent toward a fixed target for studies of nuclear and subnuclear physics, the proposal foresees the production of well collimated beams of unstable exotic fragments, by impinging the primary beam on a target located in the transfer line connecting the two accelerators. Prior acceleration of the primary beam to energies of few GeV/u is required for the production of the exotic elements with significantly large rates. The secondary beam intensities are estimated in the range of  $10^8 \div 10^9$  ions/s.

The second ring is used for the accumulation and deceleration of the unstable isotopes. To increase the phase space density of the circulating ion beam, electron and stochastic cooling are applied after injection. When sufficient particles have been accumulated, the whole beam can be decelerated down to energies of about 5 MeV/u corresponding to the Coulomb barrier, extracted and used for experiments dealing with nuclear structure studies.

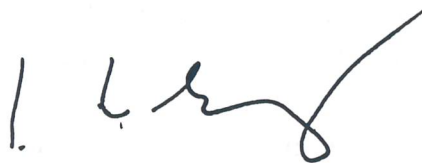
It is also possible to produce beams of electrons, muons and  $\pi$  mesons for experiments and detector developments. The availability of heavy ions with specific energies in the range of hundreds of MeV/u makes also possible many other applications such as study of cancer therapy with range-controlled probes, material science and solid state physics. Furthermore, the ADRIA complex can be also a useful tool for preliminary studies of the physics and the engineering of the inertial confinement thermo-nuclear fusion driven by heavy-ion beams.

The cost of the project is estimated around 67 billions of Italian Lire. The construction can be spanned over a five-year period integrated with a three-year period for accelerator

research and development.

The project can be developed in three phases: (1) construction of the first accelerator and targetry for the study of secondary beams; (2) construction of the second accelerator and completion of the transfer line for accumulation and deceleration of exotic fragments; and (3) addition of electron cooling.

We owe here a great thank to the Italian nuclear physics community that has contributed to the preparation of the physics case for ADRIA; a great thank also is due to the large community of engineers and physicists who have contributed with enthusiasm to the definition of the project in its guiding lines and we hope that an even larger international community will participate to the future developments. A considerable amount of technical research and findings has been documented in the conceptual design report "Feasibility Study of a Hadron Facility", edited by the LNL (February 1992). The present proposal of the ADRIA project is based on the demonstration of feasibility in the previous and more recent studies.



Prof. Pietro Dalpiaz  
Director of the Laboratori Nazionali di Legnaro

Legnaro, March 1992

## Part A

# The Physics Case for ADRIA

# 1

## Heavy Ion Physics at 1-2 GeV/u

### 1.1 Introduction

One of the ultimate goals of nuclear physics is to set up a unified description of nuclear and hadronic matter and quark-gluon plasma through an all-including equation of state (EOS).

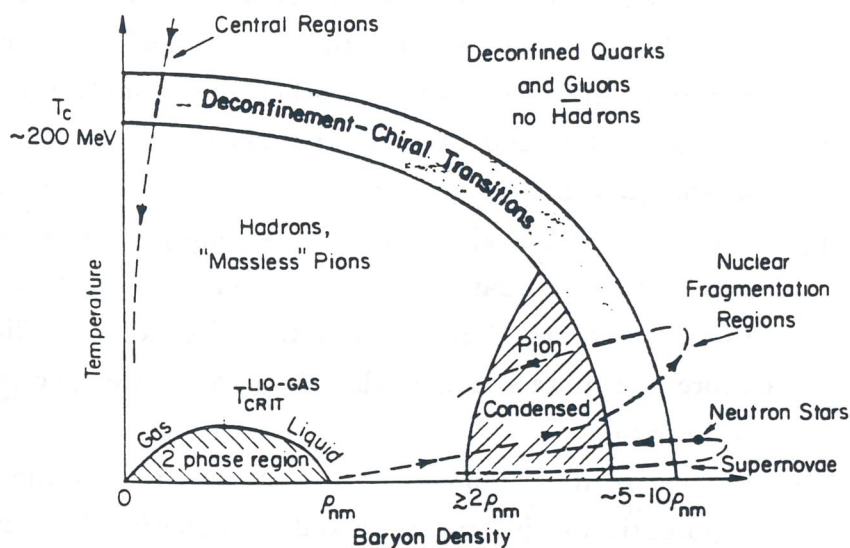


**Fig. 1.1** - Phase diagram of nuclear matter in the baryon density, temperature plane, showing regions of hadronic and deconfined matter [BAY86].

Heavy-ion collision physics has significantly advanced our knowledge of some general features of nuclei in extreme conditions. In fact, by varying the beam energy, one can realize

a spectrum of physical systems ranging from relatively cold, highly degenerate quantum fluids, through nuclear matter near to critical temperature to hot compressed hadronic matter. Although a general *equation of state* is still a far reaching problem, we gained a sufficient empirical knowledge of different regions of *phase diagram*. It is not the aim of the present proposal to inquire into such general problems. In Sect.1.3 we shall touch these questions only with the purpose of properly framing a few selected topics (discussed in Sect.1.4 and 1.5) which can be investigated experimentally at the Legnaro Laboratories using stable beams from the first ring of Adria and exploiting the instrumentation available at present and in the foreseeable future. A short preliminary discussion will be devoted to grazing collisions, whose study will require relatively simple experimental setups.

In the following we shall refer to low, intermediate and high energies to  $E \simeq 10$  MeV/u (around the Coulomb barrier),  $E \simeq 50$  MeV/u (the regime of nuclear Fermi energies) and  $E > 100$  MeV/u respectively.

## 1.2 Grazing Collisions

### 1.2.1 General Considerations

A general feature expected for grazing collisions at intermediate and high energies is that, because of the strengthening of the effects of electromagnetic interactions, the scattering processes are strongly coupled between each other. This imply that already at the stage of phenomenological description and interpretation one should resort to the conceptual apparatus of coupled channels and multistep processes. Few particle direct transfers, which are still interesting at intermediate energies, should be strongly hindered at high energies by recoil effects, which prevent accomodation of nucleons on single particle bound orbitals. Charge exchange processes, due to the large possibilities of choosing colliding nuclei and energies, can be made more and more selective; this allows accurate spectroscopic analyses of states not reachable otherwise.

In a theoretical perspective it is important to verify the role of the nucleus-nucleus optical and polarization potentials at intermediate and high energy. A satisfactory description of the optical potential and of elastic scattering is related to the possibility of getting, through the optical theorem, an accurate determination of the total cross section, including production processes.

## 1.2.2 Coulomb Excitation

Both from a practical and a theoretical point of view, high energy beams of heavy ions offer an ideal framework to study in a great detail the method of equivalent photon number (Fermi-Weizsacker-Williams method). The electromagnetic field generated, e.g. by the projectile, is equivalent to a beam of virtual photons, whose distribution probability versus the photon energy can be described by a square-box like function with  $E_{\gamma}^{Max} \simeq \gamma \hbar c / b$ , ( $b$  is the impact parameter and  $\gamma = [1 - v^2/c^2]^{-1/2}$ ), with a normalization constant proportional to  $Z_P$ . In a collision with typical impact parameter  $b \simeq 10\text{fm}$  one can get photons with maximum energy  $E_{\gamma}^{Max} \simeq 20\gamma$  MeV. From these simple relations one has an immediate feeling of the processes reachable for a given projectile energy; they range from simple Coulomb excitation of giant resonances at intermediate energies of the projectile to  $\Delta$ -excitation, pion production and lepton-pair production at relativistic energies. Since the cross sections are proportional to  $Z_P^2$ , heavy projectiles are the ideal tools for this inquiring.

In low energy heavy-ion physics, Coulomb excitation and multiple Coulomb excitation play a central role in studying low-energy collective states, and in building up a definitive systematics of these states. According to the previous considerations, by intermediate and high energy heavy-ion collisions it is possible to populate high-lying levels, such as giant resonances, and to study multiple excitation of these modes. The multiple excitation of giant resonances can lead to disruption of nuclei in fragments far from the stability line. In particular the multiple excitation of isovector modes is foreseen to lead to a (nearly) complete separation between neutrons and protons, with the possibility of reaching the *polynutron matter*.

Electromagnetic dissociation leading to fission (photofission) is an ideal tool for probing the method of equivalent photon number, because for relatively low energies one can compare the results with the ones obtained with real photons. It should be added that at high energies ( $E \simeq 1$  GeV/u) Coulomb dissociation becomes a dominant process for one- and two-particle emission from the projectile; this is related to giant resonance excitation and decay, and can be an extremely clean way to study giant resonance structure.

Direct laboratory measurements of photocapture cross sections of light ions at energies of astrophysical interest (a few keV) are extremely difficult because of hindering effects of the Coulomb barrier, so that the cross sections currently used are obtained by extrapolation from data acquired at several hundreds of keV's. The scission of an intermediate energy projectile in the strong Coulomb field of a heavy target can be viewed as the inverse of the radiative capture process and can be related to it by detailed balance theorems. Although the scission fragments have *laboratory velocity* comparable with the projectile velocity, they can be detected at angles at which their *relative velocity* is actually very low.

### 1.2.3 Study of Extreme Configurations

There exist theoretical previsions (Ikeda diagrams) according to which, in grazing heavy-ion collisions at high energy, nuclei such as  $^{16}\text{O}$  can be excited in states of four aligned  $\alpha$ -particles, due to the combined effects of Coulomb repulsion and nuclear attraction [BAY87]. There is a lack of experiments performed for the explicit search for these objects, which have been regarded as "anomalous" in standard experiments. Characterizing features of these configurations, emerged from theoretical studies, are that they should have very low transition probabilities to nearly spherical structures and be stable with respect to the spontaneous fission in two shorter linear chains. These properties, if experimentally confirmed, would allow one to consider these structures as true nuclear molecular states.

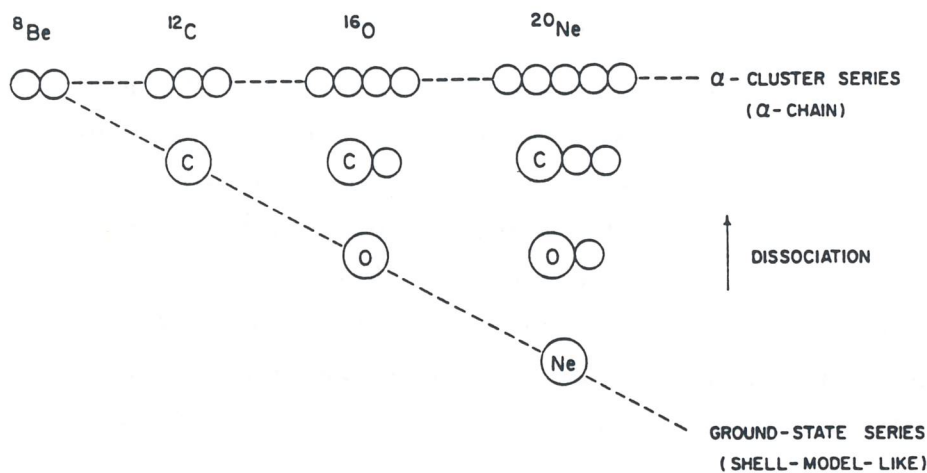


Fig. 1.2 - Ikeda diagram of structure change in self-conjugate  $4n$  nuclei. The unlabelled smaller circles represent  $\alpha$  clusters. After [BAY87].

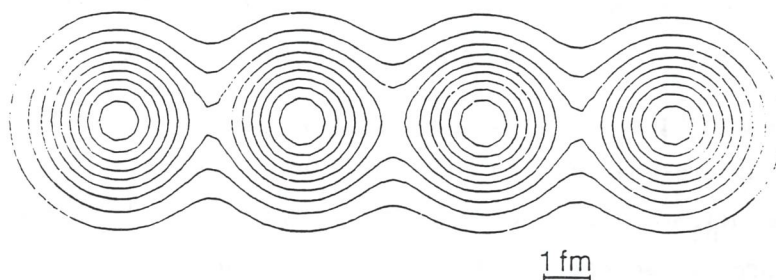


Fig. 1.3 - Density contours for the linear-chain configuration in  $^{16}\text{O}$ . The contours are plotted in steps of 10% of the peak density. After [BAY97].

## 1.3 Energy Evolution of Central Collisions

### 1.3.1 Characterizing the Transition from Low to Intermediate Energies

In the last two decades, research in heavy-ion physics has been extensively performed in two well-separated energy domains, the low-energy regime (corresponding to bombarding energies up to about  $E \simeq 10$  MeV/u) and the high-energy regime (above  $E \simeq 100$  MeV/u). Only in the last few years the availability of new accelerators has given access to the region of intermediate energies. At bombarding energies of few MeV/u above the interaction barrier the reaction mechanism proceeds via the formation of a mono-nuclear or di-nuclear intermediate system. Neglecting deexcitation processes like light particle emission or sequential fission, which do not belong properly to the reaction mechanism, the exit channel is characterized by the presence of one (in case of fusion-like phenomena) or at most two (in case of deep-inelastic processes) heavy reaction products and by the dissipation of a large fraction of the initially available kinetic energy. On the contrary, at bombarding energies of a few hundreds of MeV/u the most apparent feature of heavy-ion collisions is the production of a large number of complex fragments and single nucleons with velocities very near to those of the projectile and target nuclei (so-called mechanisms of fragmentation and spallation, respectively).

These features can be understood by resorting to general physical concepts. At low energies, the de Broglie wavelength  $\lambda$  associated with a nucleon is large compared to the average intranucleonic distance. One-body dissipation and mean-field are concepts well suited to describe the reaction, as nucleon-nucleon collisions are strongly suppressed by the Pauli exclusion principle. At high energies, the opposite approximations are applicable. Due to the decrease of the de Broglie wavelength and to the negligible effect of the so-called Pauli-blocking, the mean free path of a nucleon becomes small with respect to the nuclear dimensions and comparable to the intranucleonic distance.

The temperature of the emitting nuclei is characterized by the number of "evaporated" nucleons and complex particles and their energies. In this framework recent experiments have shown that nuclei can consistently attain temperatures up to 6 MeV. Further increase in beam energy are not reflected in higher temperatures of the nuclear system formed in the heavy-ion collision. Above these temperatures, which correspond to a thermal energy slightly less than the binding energy per nucleon, the attractive nuclear interaction can no longer counteract the repulsive Coulomb forces and the thermal pressure. This subject is discussed in more detail in Sect. 1.4.

### 1.3.2 Multifragmentation

We mentioned in the previous section the fragmentation and spallation processes occurring for peripheral collisions at high energy. If we consider central collisions, with increasing energies hot nuclei have been observed to break up into several intermediate mass fragments. At present, the mechanism of this multifragment decay has not yet been fully clarified. Suggested interpretations range from sequential fission-like processes, statistical emission from hot subsystems to novel reaction modes such as break-up due to dynamical instabilities of expanding nuclear matter. Systematics studies have shown that the key parameter governing the onset of this nuclear disintegration mode is the excitation energy stored in the composite system.

There is emerging evidence for an excitation energy window for multi-fragment emission. As predicted in microscopic N-body calculations and recently observed in experiments, the multiplicity of intermediate mass fragments goes through a maximum at excitation energies per nucleon close to the binding energy per nucleon ( $E \simeq 8$  MeV/u), indicating that at still higher energies hot systems preferentially disintegrate into a gas rather than into larger fragments (drops of nuclear matter).

In terms of equation of state, at these energies one attains the region of coexistence of the liquid and gas phase, which is one of the prominent features of hot nuclear matter. The nuclear matter isotherms, which are of standard van der Waals form, indicate just the occurrence of this effect. As the temperature is raised, the distinction between the phases diminishes and disappears completely at the critical temperature, which is expected to be around  $T_{crit} \simeq 10-20$  MeV.

### 1.3.3 High Density Nuclear Matter and Particle Production

Once the transition-energy region has been passed, the nature of the underlying nuclear dynamics (fragmentation and multifragmentation) should not change fundamentally until nuclear transparency effects come into play. At the energies of 0.7-1 GeV/u it can be put the onset for one of the most peculiar phenomena of nuclear collisions, i.e. the production of nuclear matter of high density.

When two nuclei collide a density increase is possible to occur, provided only that the nuclei stop each other rather than interpenetrate. Except at ultrarelativistic energies (not contemplated in this proposal) one should be well within the nuclear stopping regime for the bulk regions of heavy nuclei. For sufficiently large systems, thermodynamic relations can be used and the density buildup follows largely from energy and momentum conservation laws (Rankine-Hugoniot relations of shock-wave theory). The precise value of the compression is strictly dependent on the model chosen to describe the EOS and on the value of the

incompressibility parameter. A suitable tool for investigating these features is the analysis of particle production.

Subthreshold positive kaon production have been suggested as a probe for such regime. The advantage of using kaons is that, once produced, they interact only relatively weakly with the surrounding matter and are not reabsorbed at all, both features in complete contrast to pions. Microscopic calculations within the Vlasov-Ueling-Uhlenbeck model indicate that, for central collisions between heavy nuclei, the number of kaons produced can differ by a factor of three, depending on the particular equation of state assumed. Moreover, all the kaons are created at the stage of maximum compression and are therefore sensitive to the equation of state, particularly for large systems and at subthreshold bombarding energies. This subject is discussed in larger detail in Sect. 1.5.

## 1.4 The Intermediate Energy Regime

### 1.4.1 Preliminary Considerations

First experiments at intermediate energies were performed in a somewhat non-systematic manner, following more the availability of new beams and energies, rather than a well defined connecting thread. Partly due to the objective experimental difficulties encountered in this research field, the first generation experiments obtained only a limited view of the reaction mechanism. As a consequence, they did not put severe enough constraints for the model descriptions and in the end favoured an overinterpretation (and sometimes a misinterpretation) of the data. At first the attention was focussed on the similarities with the high-energy regime. In particular, there was an attempt to explain most experimental features in the frame of a participant-spectator-like picture, integrated by specific modifications when necessary. This approach, while realizing a smooth connection with the high-energy regime, produced an evident and unsatisfactory discontinuity with respect to the low-energy reaction mechanisms. Only recently, with the advent of more thoughtfully planned and more complete experiments, the existence of dissipative processes and their importance also at intermediate energies has been fully recognized.

As already pointed out and in spite of the growing complexity of the experimental requirements and of the theoretical interpretation of the results, intermediate-energy heavy-ion collisions seem to represent a rather unique opportunity to study a certain number of features characteristic of nuclear matter.

It is reasonable to expect that the most significant results will arise from a systematic and detailed investigation of how phenomena typical of the low-energy regime do evolve

with increasing bombarding energy, say from 20 to 50 MeV/u. Truly enough, low-energy phenomena are understood only in their gross features, while a deeper comprehension finds it hard to emerge, partly because the experiments are not detailed enough, partly because the models do still contain too many approximations or ad-hoc assumptions. The knowledge of the energy dependence of these phenomena will put strong constraints on possible interpretations.

### 1.4.2 Evolution from Deep Inelastic to Multifragmentation

For example, it would be interesting to follow the evolution, with increasing bombarding energy, of the so-called "deep-inelastic" phenomena, which represented the most distinctive (and unexpected!) feature of low-energy heavy-ion collisions. The question of their possible disappearance in favour of other hypothetical mechanisms has not been satisfactorily answered up to now.

In particular, a presently very much debated subject concerns the nature of the mechanism leading from the binary reactions typical of the low energies to larger and larger numbers of final complex fragments. The as yet unanswered question is whether this increasing multiplicity takes origin from a sequence of binary steps (thus reflecting more the decay modes of very highly excited nuclei), or rather from a prompt fragmentation process (the so-called "multifragmentation") more strictly linked to dynamical aspects of the collision. Detailed studies of three- and four-body events in heavy symmetric systems favour the first interpretation, at least up to bombarding energies of about 24 MeV/u. It would be interesting to extend the investigation to higher energies.

At intermediate energies, due to the decreased interaction time (with respect to the low-energy case), some internal degrees of freedom may remain far from equilibrium for the whole duration of the interaction. Alternatively, additional degrees of freedom may get excited. Thus, the observation (although difficult) of a non-equilibrium condition in the intermediate system at separation may help illuminating the microscopic aspects of the interaction and represent a crucial test for theories.

It is a widely accepted belief that the interaction between the colliding nuclei proceeds via a microscopic mechanism of nucleon exchange (single nucleons or even clusters). Additional contributions may come from mechanisms of more collective nature, at the beginning of the collision (excitation of vibrations, resonances and the like) as well as in the final phase (for example when the neck between the fragments snaps off). At low energies, the non-equilibrium condition created by these microscopic mechanisms gets generally obscured by the tendency of the nuclear system to evolve towards equilibrium, with relaxation times characteristic of each degree of freedom.

### 1.4.3 Stability Limits in Energy and Angular Momentum

Another research field which can be pursued at intermediate energies is the one concerning the stability limits of nuclei, namely the maximum amount of excitation energy which a nucleus can sustain, as well as the limits in angular momentum and linear momentum transfer which can be obtained in the collision. Also these aspects need to be faced in a systematic way, as a function of mass and mass-asymmetry of the entrance channel (up to now most studies were performed with not very massive projectiles), but especially as a function of bombarding energy.

It has also to be stressed that, with increasing excitation of the nuclear system, its characteristic decay time decreases and becomes comparable with the interaction time itself. In this case one expects that a significant fraction of the observed light particles cannot be attributed to the statistical emission from an excited but equilibrated source, but rather reflects a non-equilibrated condition of the emitting object. Up to now, the available information about pre-equilibrium light particle emission is fragmentary and usually restricted to collisions with rather light projectiles (up to about 40 amu). From a theoretical point of view, widely different mechanisms have been proposed, but unfortunately the available experimental data are not selective enough to discriminate among them. Moreover, even a reasonable prediction of the behaviour of pre-equilibrium phenomena as a function of important reaction parameters (like mass and mass asymmetry of colliding nuclei, inelasticity or impact parameter of the collision and relative velocity) is still lacking and would be very valuable for the interpretation of many experimental results.

### 1.4.4 Bulk Properties of Nuclear Matter and EOS

Finally, it seems that bulk properties of nuclear matter are not exclusive domain of the high energies, but can be studied also at intermediate energies. Indeed it has been claimed that the energy dependence of the collective behaviour known as "flow" (with its "inversion" observed in recent experiments at intermediate energies) may give precious contributions to a better understanding of the equation of state for nuclear matter.

A systematic settlement of the many open questions in this research field would strongly benefit from the availability, in a wide energy range, of rather massive projectiles, so as to minimize undesired nuclear structure effects often present with medium-light ions.

Finally, it has to be stressed that, in order to be able to perform a systematic settlement of the field with high significance, there is a strong need for a large body of clean and as-exclusive-as-possible experiments, performed and analyzed in comparable ways (or at least under very precisely defined conditions).

## 1.5 Sub-threshold Particle Production

Heavy-ion collisions at relativistic energies offer a unique possibility to study non-equilibrium dynamics of finite-size fermion systems, as well as properties of dense and hot nuclear systems. In particular there is a big interest in getting information on observables related to the nuclear equation of state (EOS); this is correlated to the compressibility of nuclear matter and to the behaviour of the density as it exists in the interior of very massive stars, supernovae and neutrons stars.

During the collision phase nuclear matter is stopped and piled-up in the reaction region; many nucleon-nucleon collisions lead to degradation of momenta of the incoming projectile constituents with observation a) of nucleonic flow in transverse directions and b) the production of particles other than nucleons.

Studies by many authors (see e.g. [CAS90]) have shown that nucleonic flow is not a clean signal for the nuclear EOS since it is determined by the interplay of three physical effects: the compressibility of nuclear matter, the in-medium scattering cross sections of nucleons and the momentum dependence of the nucleon-nucleon (NN) interactions.

Better probes for the hot and dense part of the nuclear volume which is involved in the collision are particles like pions and other mesons produced in the reaction. On one hand pions can be created in the first NN collisions and may not be directly related to the equilibrated regime, so that one must distinguish between direct and thermal pions. A big improvement has been achieved by going to energies below the free NN threshold for pion production, because in such an energy regime particles can be produced in first NN collisions with low probability and nucleons have to undergo several collisions before they can accidentally acquire an energy sufficiently high above the threshold.

On the other hand, particles such as  $\gamma$ -rays, dileptons and kaons, because of strangeness conservation, only feel weak final state interactions and leave the collision region without reabsorption or rescattering, thus giving cleaner information on the primary reaction phase.

Of course also for these particles other production mechanisms are possible, e.g. in the case of kaons second-order processes involving pions or deltas produced in the first step; theories must take into account all important contributions.

On the experimental side, only a few experiments have been done, looking at different particles and spanning an energy range from 1-2 GeV/u to as low as some tenths of MeV/u (Fig.1.4) [NuP91]. Most of the studies have been concentrated on pions and hard photons, while kaons and dileptons have begun to be investigated only very recently. The cross sections strongly depend on the energy, especially near the threshold, and the presence of events also at far subthreshold energies indicate that some new phenomena like cooperative effects can contribute to the observed yield [JUL91]. As it is unlikely that a very high nuclear density far away from its normal value is achieved, low energies subthreshold experiments

on strangeness production may point to the interesting possibility of the presence of strange quark components in nucleons even at normal nuclear matter densities. This is a very promising aspect for quantum-chromo-dynamical studies at non-perturbative level.

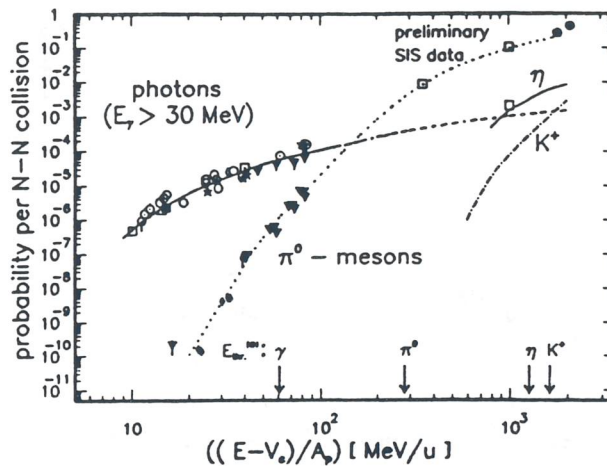


**Fig. 1.4** - Experimental cross sections for the production of various particles as a function of the bombarding energy in a collision of a symmetric mass system ( $20 + 20$ ). Note that the cross section scale covers twelve orders-of-magnitude.

Both theoretical and experimental studies require sophisticated techniques. The theoretical description of particle production involves the many-body dynamics and the elementary production processes. The former is based for example on the Vlasov-Uehling-Uhlenbeck equation for the one-body phase-space distribution  $f(r, p, t)$  and involves a non-perturbative treatment of the NN interaction. The production of particles is treated on the basis of incoherent in-medium baryon-baryon collisions. Although a certain amount of experimental data have been explained at above threshold energies, at lower energies several improvements are needed.

From the experimental side the low yields available impose the use of advanced detectors and triggers which are partly borrowed from elementary particle physics and partly match common nuclear techniques. A recent study of  $^{197}\text{Au} + ^{197}\text{Au}$  at 1 GeV/u to get cross sections for kaon production [AHN91], uses a properly designed spectrometer, which combines optical magnetic elements similar to the ones utilized in low energy heavy-ion reactions (e.g. recoil mass spectrometers and spectrographs) and a multiple detection system with multiwire proportional counters, scintillator arrays and time-of-flight detectors. With a proper hardware/software selection procedure one gets clean focal plane spectra as shown in Fig. 1.5. The accuracy can be improved to measure cross sections at the level of some hundreds of picobarn.

Often, the selection of good events requires the reconstruction of particle trajectories and the acquisition of several parameters like energy losses, time coincidences, veto condi-

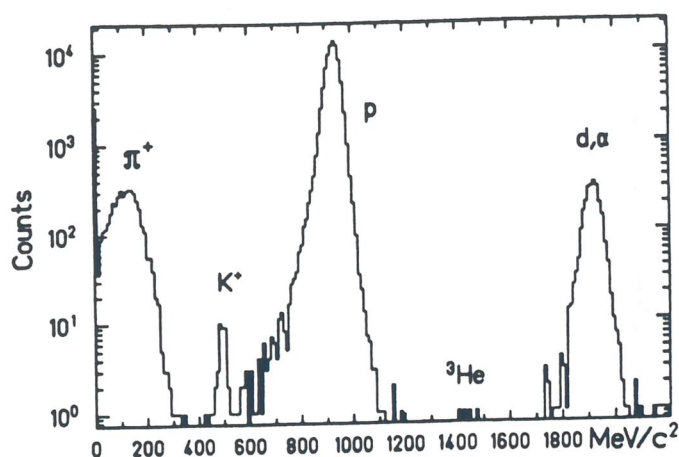


**Fig. 1.5** - Mass spectrum taken for  $^{197}\text{Au} + ^{197}\text{Au}$  at 1.0 GeV/u within a momentum band of  $650 \text{ MeV}/c < p_{lab} < 1150 \text{ MeV}/c$ ; the relative yields have to be corrected for trigger conditions.

tions. It is of big help the detection of charge particles in the mid-rapidity region to determine the participant's multiplicity. Also, other particle detectors at very forward angles allow to identify spectator particles, thus allowing a better understanding of the complex processes involved.

## 2

# Physics with Unstable Ion Beams

## 2.1 Introduction

Decades of experimental and theoretical studies have led the knowledge of nuclear many-body systems and of nuclear interactions to a rather satisfactory status. This knowledge, however, is so far confined mainly to the properties of nuclear states not too far from the ground-state equilibrium configuration, i.e. to situations characterized by small values of the excitation energy (temperature) and angular momentum, and in addition limited to stable (or nearly-stable) nuclei, i.e. to values of the isospin ( $Z-N$ ) close to the equilibrium valley in the mass table.

Nuclear systems are not expected to display the same properties as we move from this rather confined region of mass, charge, angular momentum and temperature. Atomic nuclei are in fact rather peculiar finite-size quantal aggregates, whose static and dynamical behaviours are basically dominated by the interplay between single and collective degrees of freedom. It is the residual interaction which, acting between the nucleons moving in the self-consistent average field, essentially determines the properties of the system. But the finiteness of the system implies that this residual interaction depends strongly on the particular orbits occupied by the last few nucleons outside the closed-shell core. In a similar way the features of the collective modes are intimately related to the positions of the proton and neutron Fermi levels and to the availability of a limited number of specific particle-hole states. It is therefore not surprising that major changes and phase transitions are expected to take place as we inject temperature or angular momentum into the system or when we alter the ratio between numbers of protons and neutrons, all features that lead to modifications of the average field and of the level occupancy.

Important steps in the wide domain of high-spin states and of hot systems have been recently obtained exploiting newly developed ion facilities in connection with sophisticated detection techniques. In this respect the possibility of using *radioactive nuclear beams* offers an unique opportunity of investigating also the path moving in the third direction, namely the  $N/Z$  degree of freedom. These exotic nuclei, in fact, aside from the possibility of being studied *in se*, open new perspectives when accelerated and used in order to induce secondary reactions.

From a point of view of nuclear structure these secondary reactions allow the production and the study of new nuclei still farther from the stability line. It will then be possible to investigate nuclear structure properties of both single-particle and collective nature along extensive chain of isotones and isotopes, for example following an entire major shell from closure to closure. Due to the different configurations involved, this allows to enlarge the

knowledge and the understanding of the residual interaction to presently unknown areas of the configuration space. Similarly the richness of the different single-particle orbits involved will open the possibility of a more detailed study of the occurrence of phase-transition phenomena, beginning with the one associated with shape degrees of freedom. We will be able to study the transition from spherical to deformed shape (and eventually back to the original spherical one) separately for the proton and neutron degrees of freedom following isotone and isotope chains respectively, as well as possible transitions involving not only the conventional quadrupole but also octupole or higher reflecting-asymmetric surface degrees of freedom.

One of the appealing features in this excursus outside the stability region is the possibility of reaching nuclei with such ratios  $N/Z$  so to display really radically different behaviours. The already studied nucleus  $^{11}\text{Li}$  can serve as a promising paradigmatic example. The peculiar mass distribution, with the presence of a halo associated with the last two valence neutrons, opens interesting aspects on the shell model with weakly bound systems as well as on the nature of new soft dipole modes corresponding to the motion of the halo nucleons with respect to the core.

New perspectives may also be opened by the use of unstable ion beams in the longstanding problem of new superheavy nuclei, and eventually new stability islands. Use of extreme neutron rich projectiles on the already neutron rich actinides in  $(\text{HI}, \text{xn})$  reactions should in fact allow the production, identification and study of the decay properties of new transactinides isotopes. This is a crucial problem, not only in itself, but as a probe of nuclear structure models, as well as of the mechanisms for compound-nucleus formation and evaporation/fission decay.

The new nuclear structure features will also open new areas in the heavy-ion reaction processes. New combinations of colliding systems become in fact available, allowing for more systematic studies of the reaction mechanisms as a function of the proton or neutron numbers. In addition it will be possible to study the effects on the reaction process of having colliding systems characterized by extreme conditions, such as superdeformation and stable octupole deformation, which are in nearly-stable nuclei only present at high angular momentum or temperature. The large availability in  $Z$  and  $N$  will be an important aspect in the study of those reactions, such as charge-exchange reactions, directly involving the isospin degree of freedom; we only mention in this respect the exciting possibility of charge-exchange (and multi-charge exchange) reaction connecting heavy mirror nuclei.

Specific features are expected in reactions involving very neutron-rich systems as a consequence of the neutron halos extending at large distances from the core. All grazing reactions, such as one-particle or multiparticle transfers, will be strongly enhanced, as well as fusion processes at energies below the Coulomb barrier. High  $Q$ -values, deriving from the weakly bound nature of the halo neutrons, will also show up in further enhancement of cross sections. Also the polarization heavy-ion potential arising from the coupling to reaction channels is expected in this case to differ from the systematic behaviour characterizing the "normal" systems.

## 2.2 Nuclear Structure

### 2.2.1 General Considerations

New advances in nuclear structure studies based on radioactive beams will require beam-

energies close to the Coulomb barrier (5–10 MeV/A). An accelerator complex like ADRIA will provide a large range of such beams with good intensities ( $\geq 10^9$  p/sec). This will greatly extend the range of compound nuclei which could be produced in a heavy-ion reaction. It will be possible for the first time to study the high-spin structure of both neutron-rich and stable rare-earth nuclei. On the proton-rich side, the proton drip-line will be reached or exceeded for all nuclei with  $Z \geq 50$ .

The frontiers of nuclear structure studies that may be addressed with the proposed facility are rather wide and open to further developments. We can mention: new extremes of nuclear deformations, neutron halos, giant resonance phenomena in unstable nuclei, Coulomb excitation of unstable nuclei, structure on and beyond the proton drip-line, particle radioactivity and cluster emission, single particle degree of freedom in unstable nuclei, new singly and doubly-magic regions, high-spin spectroscopy of neutron-rich and stable nuclei, new collective modes, isospin symmetries, reactions on excited nuclei, nuclear masses, radii and moments. Some of these items will be illustrated in some details in the following sections.

### 2.2.2 Neutron-rich Region. Neutron “Halos”

Peculiar density distributions are expected to be the characteristic feature of nuclei with extreme neutron excesses. Excess neutrons will in fact occupy the outer region of the nucleus, so extending to distances where the tail of the proton density is negligible. This neutron predominance will therefore lead to alteration of the mean field, with the subsequent appearance of novel features such as new magic numbers, completely different deformations for the proton and neutron components and consequent new variety of excitation modes.

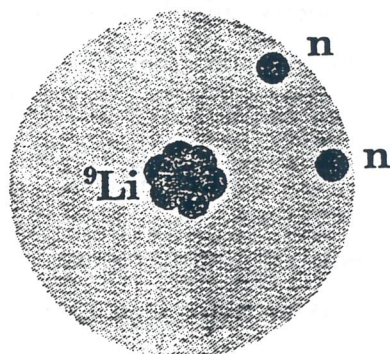


Fig. 2.1 - Pictorial representation of  $^{11}\text{Li}$  nucleus.

The neutron excess can even reach situations where the outer neutrons completely separate from the core, giving rise to sort of neutron “halos” [HAN91]. Fig. 2.1 gives a pictorial representation of  $^{11}\text{Li}$  in terms of the  $^9\text{Li}$  core plus the two separated valence neutrons. The formation of such characteristic distributions offers unique conditions for the study of relatively pure neutron matter, with the possibility of facing fundamental questions such as equation of state, saturation properties and compressibility in neutron matter. Unusual pairing properties should also show up in such low-density halo of weakly bound neutrons. Similarly novel aspects will be present in large mass decay processes (so called exotic decay), as well as in the long-standing problem of surface cluster phenomena.

### 2.2.3 Study of Giant Resonances in the "Halo" Nuclei

Giant resonances can be viewed as the modes associated with the nuclear zero sounds. Their properties (centroid energy, width, strength) have been studied in great detail, both theoretically and experimentally, in the stable nuclei [SPE91]. It appears imperative to extend these studies to the radioactive exotic nuclei like the "halo" nuclei (e.g. the already studied  $^{11}\text{Be}$ ,  $^{11}\text{Li}$ ,  $^{11}\text{B}$ ) having weakly bound neutrons which extend far beyond the standard size of the stable nuclei.

From the theoretical point of view many microscopic calculations have been performed in the last few years for such systems within different approaches (shell model, random phase approximation, sum rules, cluster models) for the giant resonances of different multiplicities [BER91], with special attention for the dipole mode. These studies predict a new kind of dipole excitation at very low excitation energy,  $E_x \sim 1$  MeV, having a large transition strength with exhaust a few percent of the energy weighted sum rule (pigmy resonance). It is a soft dipole mode as the halo neutrons oscillate slowly with respect to the core.

Experimentally, the energy dependence of the electromagnetic dissociation cross sections [SHI91] and a recent measurement of the double charge exchange reaction  $^{11}\text{B}(\pi^-, \pi^+)^{11}\text{Li}$  [KOB91] provide a strong evidence for this new kind of dipole excitation in halo nuclei.

It is noted that this low-energy collective dipole mode would affect the neutron-capture cross section [PYW85] and could result in significant modification of our understanding of the nucleosynthetic r-process. The coupling to this mode will also increase the sub-barrier fusion cross section (cf. Sect. 2.3), but the effect may be reduced by the dissociation of the halo neutron.

Similar properties have been predicted for the modes of the other multiplicities,  $0^+$ ,  $2^+$ ,  $3^-$ , and could be tested in the inelastic scattering of radioactive beams on light targets. Of course it will be also necessary to study the usual Giant Resonances to obtain information on the coupling of the halo with the core.

The properties of the isoscalar Giant Monopole Resonance are connected to the compressibility of the nuclear matter. The use of radioactive beams in inelastic scattering experiments populating the GMR will allow a systematic study of this property as a function of the isospin.

The short-lived radioactive exotic nuclei can not be used as targets and therefore electron and/or polarized proton scattering experiments can not be performed to study the density distribution. However, one may use the strong sensitivity of the Giant Dipole Resonance nuclear excitation cross section to the difference between the neutron and proton radii to get information on this quantity [KRA91] and make comparison with the theoretical values.

## 2.2.4 Exotic Decays

The occurrence of spontaneous decay processes with emission of a heavy fragment with mass intermediate between the  $\alpha$ -particle and the fission fragments has been recently observed [PRI89]. Reported cases, which include  $^{14}\text{C}$ ,  $^{20}\text{O}$ ,  $^{24-26}\text{Ne}$ ,  $^{28,30}\text{Mg}$  and  $^{32}\text{Si}$  emission, favour processes leading to daughter nuclei close to doubly-closed systems. Tunnelling in the multidimensional space of shape deformation combined with a correct description of the nuclear structure in terms of many-body correlations seems to be the key-elements for a proper interpretation of the mechanism responsible for such exotic decays. Still the subject remains one of the most challenging problems from both experimental and theoretical points of view.

Even on the simple ground of the dependence on the  $Q$ -value it is clear that the possible occurrence of the process, the emission rates and the preferred decay channels are expected to vary considerably along the mass table. In this framework predictions have been recently made [POE91] also in regions far from the stability. In particular a new interesting region of cluster radioactivity with measurable branching ratios relative to the  $\alpha$ -decay is expected on the neutron-deficient side, i.e.  $^{12}\text{C}$ ,  $^{16}\text{O}$  and  $^{28}\text{Si}$  emissions from  $^{114-116}\text{Ba}$ ,  $^{118-125}\text{Ce}$  and  $^{127,128}\text{Sm}$ . Another island of cluster radioactivity is estimated for  $Z=58-76$ , neutron rich,  $\alpha$ -stable parents.

## 2.2.5 Nuclear Spectroscopy Far from Stability

An important inspiration for spectroscopic studies of far unstable nuclei has been the expectation of finding new regions with "simple" properties, new magic regions and new deformed regions. In fact in recent years a great progress has been made in this field and new forms of collectivity, new regions characterized by shape phase transitions, new doubly magic nuclei have been discovered. In many cases these new findings have altered our thinking about the basis of collectivity and deformation ( e.g. discovery of deformation in the  $A=100$  region far from stability) and of the magicity of some neutron/proton numbers (e.g. the  $^{80}\text{Zr}$  nucleus expected to be spherical and found to be deformed). Only radioactive nuclear beams offer today the possibility of extending this work in new directions that will greatly enhance our understanding of nuclear structure. As mentioned already before, it will be possible to characterize phenomena across entire shells ( magic to magic) and from deformed mid-shell regions through a closed shell to the next deformed region.

As an example of a possible typical scenario we consider in Fig. 2.2 the case of the even-even Nd isotopes. The predicted spectra [MAI82] are based on a schematic collective model (IBM-1). The low-lying energy levels show characteristics of  $\gamma$ -soft rotors in the light isotopes ( $^{136,138}\text{Nd}$ ), single particle components near the neutron shell closure at  $N=82$

( $^{142}\text{Nd}$ ), highly anharmonic vibrational patterns in the intermediate region ( $^{144-148}\text{Nd}$ ) and behaviours of asymmetric rotors above  $N=90$  ( $^{152,154}\text{Nd}$ ), due to the disappearance, with increasing neutron number, of the effect of the  $Z=64$  proton subshell closure. Extrapolating from this example, ever richer situations are expected when moving even farther from the stability.

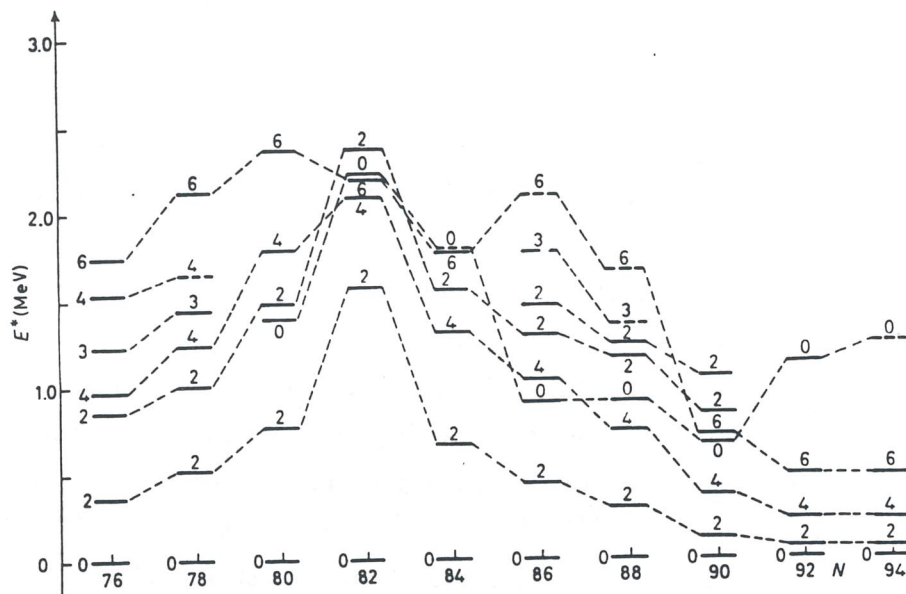


**Fig. 2.2** - Positive parity low-lying levels for Nd isotopes vs. neutron number  $N$ . Available experimental levels (solid segments) are supplemented by theoretical levels obtained with an IBM-1 hamiltonian (dashed segments).

### 2.2.6 The Structure of Proton-rich Nuclei: the $N = Z$ Nuclei

In the study of nuclei far from stability on the proton-rich side the  $N=Z$  self-conjugate nuclei play a major role. A reinforcement of the proton and neutron shell effects is predicted to occur in phase for these nuclei, giving the possibility of observing new exotic shapes such as hyperdeformation, nonaxial octupole deformation, oblate superdeformation. An open question is the persistence of magic numbers very far from stability; our understanding of nuclear shell structure is based on the knowledge of magic nuclei in the valley of stability but already the first results on the  $N=Z$  nucleus  $^{80}\text{Zr}$  give indication of a "softness" of this doubly magic nucleus [LIS85]. Especially in the region around  $^{80}\text{Zr}$  the current theoretical nuclear models are predicting structural changes occurring very rapidly with changing  $N$  and  $Z$ . Along the  $N=Z$  line lies the nucleus  $^{100}\text{Sn}$  which has been sought for almost two decades and which is probably stable with respect to particle decay. It is evident the importance of the investigation of this doubly magic nucleus, probably the best example of this kind of nuclei although presenting the strongest Coulomb effects.

In the last years studies of even-mass,  $N=Z$  nuclei have been extended to  $^{80}\text{Zr}$  and to  $^{84}\text{Mo}$  [GEL91], using fusion-evaporation reactions near the Coulomb barrier. The two-neutron evaporation yields that populate these nuclei are at the limit of our present experimental capabilities because charged-particle emission is the dominant evaporation mode in the proton-rich compound systems and fusion cross sections are very small near the Coulomb barrier. Near barrier fusion reactions have also the disadvantage that the compound nucleus is populated with a small amount of angular momentum. Therefore, much of the interesting high-spin physics in the  $N=Z$  nuclei will not be possible with standard beams even if the detection sensitivity is enhanced by several orders of magnitude using the more advanced  $\gamma$ -arrays (GA.SP [BAZ91], EUROBALL [GER91]) and the upgraded Recoil Mass Spectrometer (RMS) at LNL [SPO85]. We mention here that the presence at Legnaro of the RMS in conjunction with GA.SP (and possibly EUROBALL), give a unique opportunity to fully use radioactive beams in the study of proton rich nuclei along the  $N=Z$  line. The above mentioned  $^{80}\text{Zr}$  and  $^{84}\text{Mo}$  were produced with cross-sections in the range of 10-60 microbarns and only the combination of an RMS and a large  $\gamma$ -array has given the possibility to identify the first excited states in those nuclei.

By using radioactive beams many self-conjugate nuclei can be reached in heavy-ion reactions involving charged-particle emission, and the expected cross section can be around 10 millibarns. The use of Euroball, RMS and of a  $4\pi$  charged particle detectors gives therefore the possibility to do spectroscopy of these elusive nuclei up to (and may be beyond)  $^{100}\text{Sn}$ .

With the present facilities (RMS and a small  $\gamma$ -array) some work has already been done at Legnaro in this field. As an example Fig. 2.3 shows a  $\gamma$ -ray spectrum taken in coincidence with mass  $A=106$  detected at the focal-plane of the RMS in the reaction  $^{58}\text{Ni} + ^{54}\text{Fe}$  [DEA91]. The lines of  $^{106}\text{Sn}$  populated after  $3p2n$  evaporation are clearly seen. It is obvious that radioactive beams are at present the only way to reach  $^{100}\text{Sn}$  since the available (and future)  $\gamma$ -arrays are well suited for this kind of study in the presence of a reasonable production cross section.

### 2.2.7 Exotic Shapes

Nuclei exhibit a variety of shapes from spherical to superdeformed. The nuclear shape depends strongly on the availability of specific combinations of nuclear configurations near the Fermi level. For example, the neutron  $2d_{5/2}-1h_{11/2}$ ,  $\Delta l=3$ , pair contributes strongly to the octupole (reflection asymmetric) degree of freedom in the  $A=150$  region. With the advent of unstable beams other combinations of exotic configurations will become accessible giving rise possibly to new types of nuclear collectivity and new nuclear shapes. Some of the possible exotic nuclear shapes are illustrated in Fig. 2.4. The study of nuclear shapes

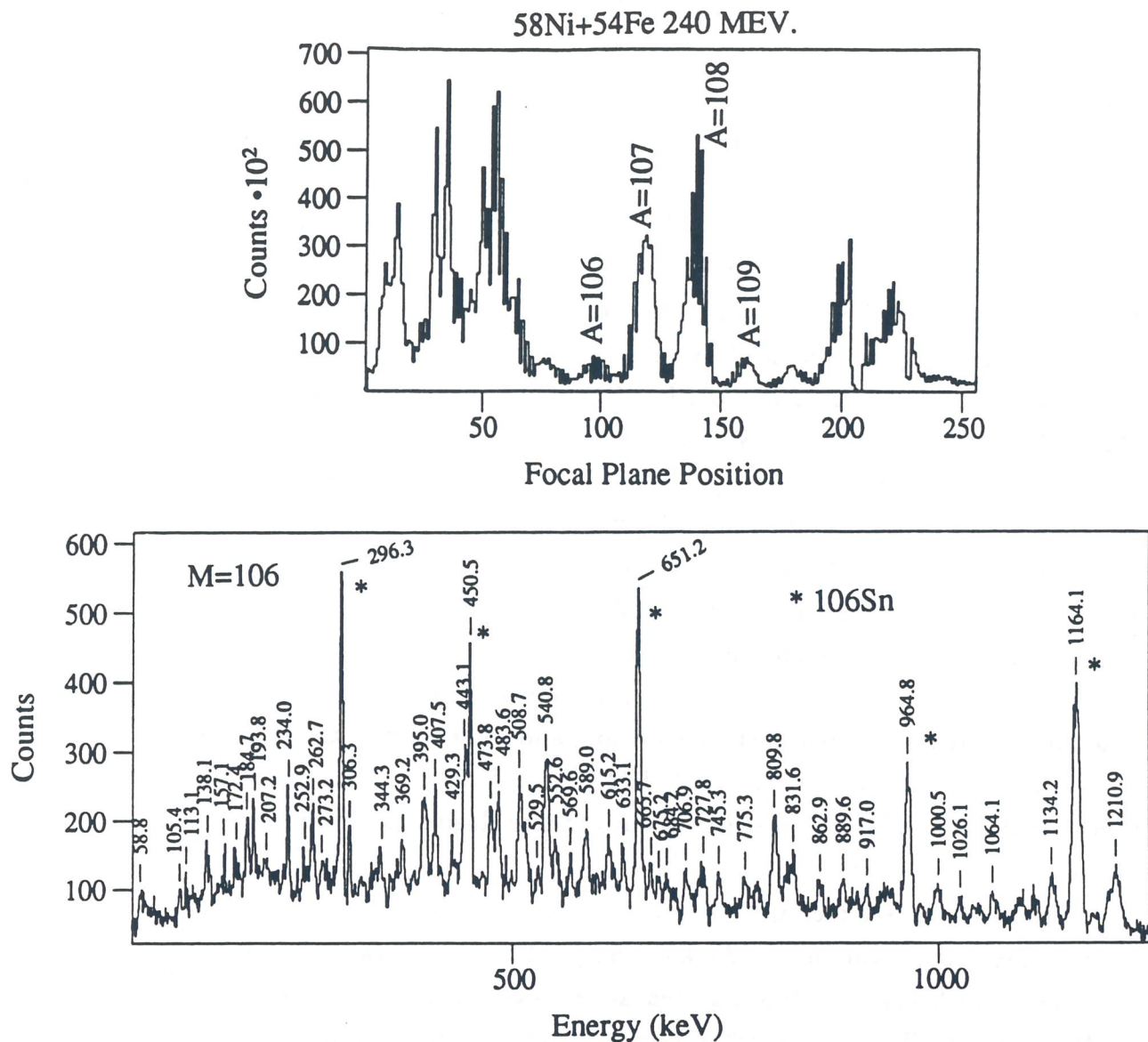


**Fig. 2.3** - The  $\gamma$ -ray spectrum in coincidence with mass  $A=106$  in the reaction  $^{58}\text{Ni} + ^{54}\text{Fe}$ . The mass spectrum at the focal plane detector is also shown.

requires both the extension to different nuclear regions, only accessible with radioactive beams, and the addition of angular momentum to the nucleus.

These two aspects can be discussed in more detail taking as examples the cases of “superdeformation” and “hyperdeformation”. Superdeformed shapes are seldom found at low spin, except in fission isomers in the actinide nuclei. Rotation provides the added stability that allows the extension of such studies to lighter systems. And, indeed, superdeformed shapes have been discovered in many other regions of the nuclide-chart [JAN91]. However, with the availability of only stable beams and targets, the understanding of nuclear structure at high spin has been limited to neutron deficient nuclei. The advent of radioactive beams will provide access, as already mentioned, to the high spin structure of both neutron rich

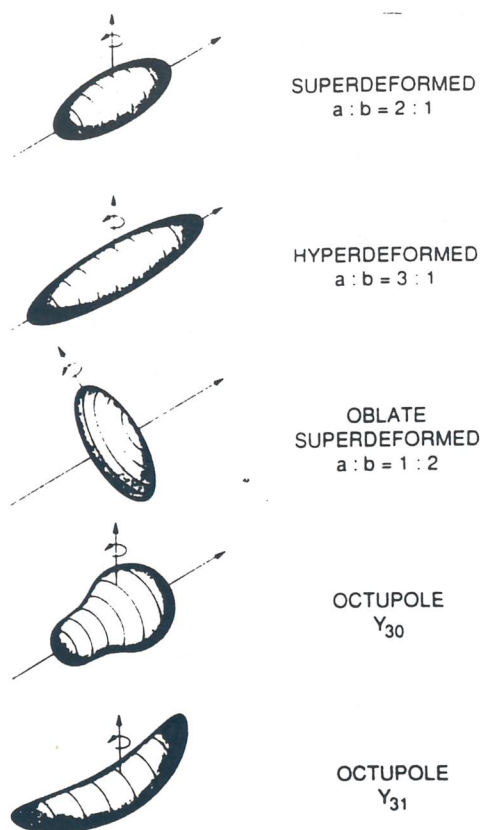


Fig. 2.4 - Pictorial illustration of possible "exotic" nuclear shapes. From [ISO91].

and stable nuclei.

The next major goal in this field is to test the prediction, made in the same theoretical framework as that for superdeformation, of nuclear "hyperdeformation" in which the nucleus adopts a 3:1 axis ratio [DUD88]. Such states are predicted to exist at the limit of rotational frequency which the nucleus can sustain before fissioning. On the neutron rich side of stability the barrier against fission of the compound nucleus formed in a heavy ion induced reaction is increased, allowing the observation of such shapes in rotating nuclei with large neutron excess. Calculations verify that for the isotopes of a typical rare earth nucleus such as Er, the limiting angular momentum imposed by fission is increased for each additional neutron. The predictions of Dudek *et al* [DUD88] suggest the heavy Er and Yb nuclei as the best candidates in which to observe hyperdeformation. From calculations it is foreseen that the hyperdeformed states become yrast at  $I > 70\hbar$  where fission competition becomes significant. It is therefore necessary to choose symmetric mass-target systems to minimize the excitation energy for a given input angular momentum. A possible reaction could be  $^{82}\text{Se}(^{90}\text{Kr}, 4n)^{168}\text{Yb}$ . The microscopic fission barrier in  $^{168}\text{Yb}$  at  $I = 70\hbar$  is comparable to that in  $^{152}\text{Dy}$  at  $I = 60\hbar$ , where the superdeformed states are populated.

The existence of minima in the total energy surface at large deformations and high spin results from gaps in the deformed shell structure of both neutrons and protons. Superde-

formation and hyperdeformation involve the occupation of key orbits crossing two or more major shells. The particular combinations of  $N$  and  $Z$  for which this occurs can frequently be reached only with radioactive beams.

### 2.2.8 New Regions of Deformation Close to the Proton Drip-line

Studies of nuclear collectivity at low spin have been limited to the valley of stability, to few neutron-rich fission products and to some nuclei on the proton-rich side. The evolution of collectivity from closed shell nuclei to the highly deformed regions has been studied in detail only in very light and heavy (rare-earth and actinides) nuclei. Since the properties of light and heavy systems differ in many respects, a lot can be learned from the study of the intermediate mass  $A=130$  deformed nuclei. This kind of study has been started already at the Legnaro Tandem and significant results have been obtained on the onset of deformation below  $N=82$  in Samarium nuclei [SOR88, CAR91]. The investigation of the most deformed nuclei in this region, however, remains beyond our present reach because they are situated near or beyond the proton drip line. In these nuclei, the proton Fermi level lies low in the  $1h_{11/2}$  subshell, and the neutron Fermi surface lies high in the same subshell. In configurations with protons or neutrons excited to the  $1h_{11/2}$  orbitals, a variety of shape changes and shape coexistence phenomena may appear, since the protons favour prolate shapes and the neutrons favor oblate or triaxial shapes. Thus far, only the transitional portion of the  $A=130$  deformed region is accessible to experimental studies using stable beams and targets. This study has been performed in recent years in many laboratories including Legnaro. Figure 2.5 shows the evolution of the deformation parameter  $\beta$  from  $N=80$  to  $N=72$  in the light Samarium isotopes. For the center of the deformed region, the Fermi surfaces for both neutrons and protons are closer to the middle of the  $1h_{11/2}$  subshell. With the exotic beams accelerated by ADRIA it will be possible to produce sufficiently proton rich nuclei for the protons and the neutrons to cooperate in establishing energetically favored stable prolate shapes.

Another interesting research topic in this region is superdeformation. Large superdeformed gaps are predicted for  $N=62$  and  $Z=64$ . Simultaneous reinforcement of the proton and neutron shell effect should result in stable superdeformed shapes in the nearly self-conjugate  $^{124,126}\text{Nd}$  and  $^{126,128}\text{Sm}$  nuclei.

### 2.2.9 The Nuclear Shell Structure Far from Stability

The nuclear shell model, with its single-particle basis and residual interactions, is fundamental to nuclear structure. It is the starting point for any other, more macroscopic, geometric, algebraic, and phenomenological models. Together with HF and HFB approaches, it provides the microscopic basis for the mean field. But the shell model is not an immutable

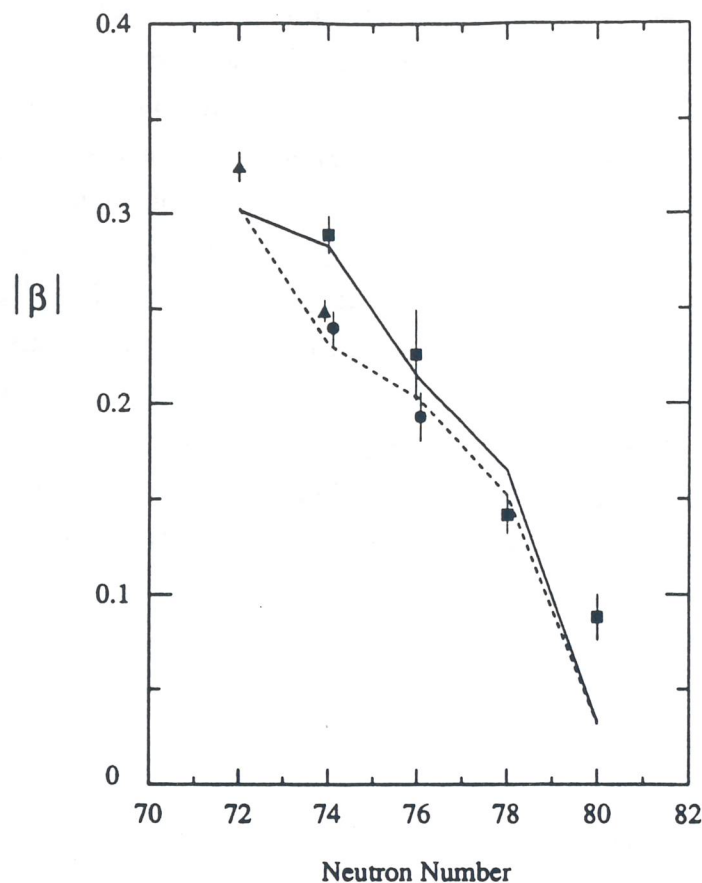


**Fig. 2.5** - Experimentally deduced quadrupole deformation parameter  $\beta$  as a function of neutron number in Samarium isotopes, compared with two different theoretical predictions [CAR91].

edifice. Because the central potential is due to the interactions of the nucleons that orbit in its mean field, there is an evolution of shell structure with  $N$  and  $Z$ . Single particle level energies change across the periodic table. This is largely due to the effects of residual interactions among the valence nucleons. In particular, it is a result mainly of the p-n interaction ( $T=0$ ), whose critical role is now becoming more fully appreciated. The monopole part of the p-n interaction modulates the shell-model single particle energies that define the available basis space within which the quadrupole p-n interaction acts. An understanding of exactly how the monopole p-n interaction affects single-particle energies depends on an acceptable model for that residual interaction. To develop such a model requires a knowledge of empirical p-n matrix elements for complete sets of interacting proton and neutron orbits. This task implies measurements of masses and binding energies, and single-particle energies for key nuclei that are unavailable with stable beams and targets. These nuclei include singly magic, or singly magic plus two, nuclei for sequences of isotopes or isotones in which the other nucleon is filling each of the successive orbits in its major shell. Mapping

shell structure through single-particle states far from stability and as a function of isospin, therefore, can serve as a test of our understanding of these residual interactions, and as a direct indicator of the structure of individual nuclei. Principal among experimental approaches are single-nucleon transfer reactions with radioactive nuclear beams, which are the most direct source of information on the microscopic structure of the nucleus. Of course, the most important studies will be those of the single particle levels adjacent to doubly magic nuclei that will be accessible with ADRIA, especially those near  $^{78}\text{Ni}$ ,  $^{100}\text{Sn}$  and  $^{132}\text{Sn}$ . In addition to observation of single-particle states near closed shells, single-nucleon transfer reactions are valuable for studying the Nilsson model far from stability; examining Coriolis effects in deformed nuclei; identifying specific key orbitals - at either low or high spin - that are critical for understanding specific structural phenomena such as superdeformation and quantal localization; and providing parameters vital to calculations of superheavy nuclei.

## 2.3 Nuclear Reactions

### 2.3.1 General Considerations

As exotic beams have an excess of protons or neutrons compared to stable nuclei, they are characterized by more loosely bound nucleons and this represents a very attractive feature in studies of nuclear reaction dynamics. As examples we mention  $^{17}\text{F}$  with a proton binding energy of only 0.6 MeV,  $^{14}\text{O}$  and  $^{30}\text{S}$  with two-proton binding energies of 6.57 and 7.15 MeV respectively. On the neutron rich side the most classical example is  $^{11}\text{Li}$  where the neutron radial density extends twice more than the proton one so that one deals with "neutron halos" in nuclei.

The use of radioactive beams to initiate nuclear reactions enlarges enormously the number of projectile-target combinations that one can exploit with respect to the limitations imposed by the valley of stability. These new possibilities allow the study of various nuclear phenomena and to address specific questions, such as the diffusivity of the optical potential, its energy dependence, the doorway channels for fusion, Q-value effects, almost in a continuous way. This should enable us to pin down the relevant degrees of freedom.

Of course there are other advantages related to the use of radioactive beams. They stem from the presence of weakly bound nucleons that allow a very broad range of Q-values, thus making accessible a large varieties of reactions (we point out that very often enhanced cross sections will compensate for lower beam intensities). The weakly bound nucleons, specifically neutrons, are characterized by quite large radii that could be responsible for an enhancement of the cross sections, e.g. in the fusion process or in transfer reactions where

new paths may be opened for multinucleon transfer. In fact, unusual reaction patterns may be observed: neck formation, dynamical deformation, particularly asymmetric shapes, new doorway states in the intermediate steps of the reaction and the likes. Moreover, in the reactions that occur at large distances there is a reduction of the Coulomb component that usually complicates the data analysis.

The study of the reactions at large internuclear distances may bring new insight into nuclear phenomena like the diffusivity of the nuclear densities and the behaviour of the optical potential. The existence of one-particle transfer reactions with large positive  $Q$ -values may allow the study of the energy dependence of the optical potential in conditions that were not available with stable beams. Since, by changing the beam and/or the target, one can modify almost continuously the properties of the nuclear surface one can really identify the channels that are responsible for these behaviours.

Moreover, the neutron skin thickness is predicted to be particularly large for a nuclear asymmetry between protons and neutrons of about 0.4, implying new collective modes that involve out of phase motion of neutrons vs. protons. This would be the case of the low-lying component of the giant dipole resonance ( $E1$ ) with the core oscillating relative to the neutron mantle. That soft dipole mode (pigmy state) is predicted to influence strongly heavy-ion fusion at energies below the Coulomb barrier.

Single-particle state properties may be studied via one-particle transfer reactions, while collective states may easily be studied via Coulomb excitation. The interplay between the  $T=0$  and  $T=1$  channel of the pairing correlations, very important for the existence of the neutron halo, may be studied via two-particle transfer and also charge-exchange reactions.

In this section we will illustrate a few examples of reactions with exotic beams at energies around the Coulomb barrier where the ADRIA project is mainly centered and where various groups performing experiments at LNL have accumulated a considerable experience. We do not want to cover all the field of nuclear reactions but just spot some of the highlights. As a guideline we believe that very interesting collisions could take place when projectile and target are particularly rich or poor of neutrons respectively (e.g.  $^{132}\text{Sn} + ^{118}\text{Sn}$  or  $^{68}\text{Ni} + ^{58}\text{Ni}$ , or when they are both rich (or poor) in neutrons and finally when we deal with one or two doubly magic nuclei.

### 2.3.2 Fusion Around and Below the Coulomb Barrier

In recent years several experiments of sub-barrier fusion have been performed and measured cross sections have shown systematically large enhancements with respect to the simple expectations of one-dimensional tunneling. Moreover, significant isotopic effects have been evidenced: namely the cross sections are considerably different (even more than one order of magnitude) for very similar target/projectile combinations. The general interpretation is

that around the barrier nuclear structure effects are non negligible and contribute considerably to the cross section enhancement: during the collision nuclei start to vibrate and/or rotate (according to the various degrees of freedom which can be excited) and also to exchange nucleons. All these processes lower somewhat the barrier and the net result is always an increased tunneling penetrability and consequently a larger fusion cross section.

A detailed theoretical description can be quite involved [SAT87] but also more simplified approaches (e.g. [DAS83]) often give satisfactory results for medium-heavy systems: by coupling various inelastic excitation and transfer channels the fusion cross sections can be fairly well reproduced at least in the bulk of the experimental results. For heavier systems more phenomenological approaches have been devised such as neck formation and the free flow of neutrons [STE88, AGU88, IWA88]. The availability of radioactive beams extremely rich or poor of neutrons would allow one to test theories in very extreme and relevant cases. Since the process of fusion is initiated by nuclear forces when nuclei are sufficiently close, neutron halos can dramatically enhance the interaction between the colliding nuclei and the consequent fusion. This means that even with low intensity beams, as is sometimes the case with exotic isotopes, a reasonable yield can be obtained in the experimental apparatus. But also less exotic radioactive beams can make very interesting reactions accessible. As an example we mention different combinations of Ni+Ni and S+Ni isotopes. Experimental fusion cross sections below the barrier are much larger for the  $^{58}\text{Ni} + ^{64}\text{Ni}$  and  $^{32}\text{S} + ^{64}\text{Ni}$  systems than for  $^{58}\text{Ni} + ^{58}\text{Ni}$  [BEC82] and  $^{32}\text{S} + ^{58}\text{Ni}$  [STE86] respectively, as can be seen in Fig. 2.6. A comparative study of the combinations  $^{56}\text{Ni} + ^{64}\text{Ni}$ ,  $^{58}\text{Ni} + ^{66}\text{Ni}$ ,  $^{32}\text{S} + ^{66}\text{Ni}$ ,  $^{30}\text{S} + ^{64}\text{Ni}$  (this last one having a very large  $Q$ -value of +11.6 MeV for 2n transfer) would be extremely interesting since it may provide a crucial check of the present understanding of subbarrier fusion.

Since the advent of heavy-ion accelerators it has been possible, with a variety of conventional projectiles and targets, to produce isotopes of all known elements and even to reach far beyond [ARM85]. For heavier systems, however, the resulting neutron numbers fall short from those corresponding to the stability valley or its extrapolation. This is one of the reasons why the use of unstable neutron-rich projectiles is likely to favour the formation of heavy, stable, compound systems (superheavy nuclei). Another important consideration is that the neutron halo surrounding the exotic projectiles makes them feel the effect of the attractive nuclear forces at longer distances than in the case of their lighter isotopes. Neutron-rich projectiles are thus expected to face lower fusion barriers than their stable counterparts.

As already mentioned above, very neutron-rich nuclei display, at low excitation energies, an additional collective dipole resonance (E1) in which the excess neutrons oscillate against the nuclear core. The mechanism by which a soft dipole mode may effectively contribute to enhance the fusion probability at low bombarding energies is illustrated schematically

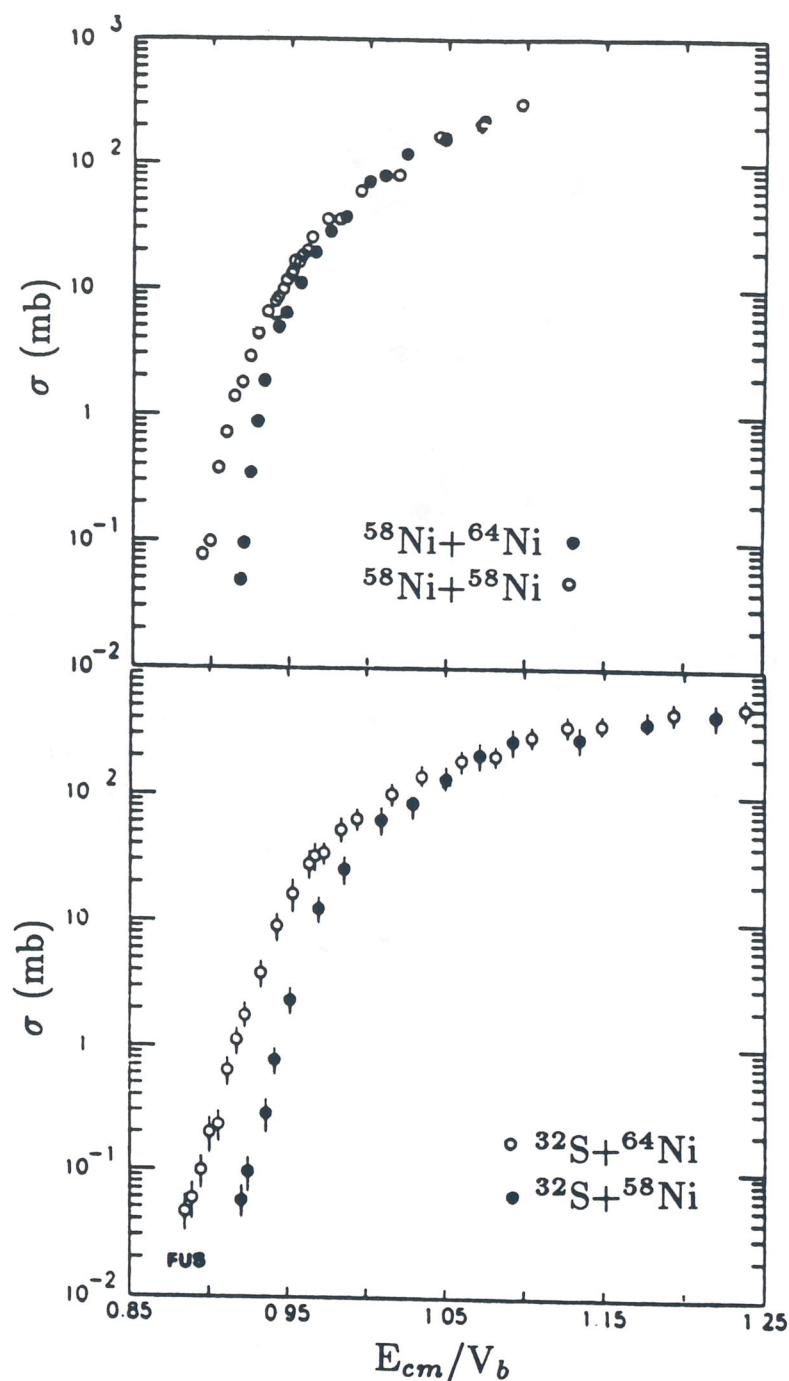


**Fig. 2.6** - Evaporation residue (fusion) cross sections for  $^{58}\text{Ni} + ^{58,64}\text{Ni}$  [BEC82] (upper panel) and for  $^{32}\text{S} + ^{58,64}\text{Ni}$  [STE86], plotted vs. the energy relative to the Coulomb barrier [VAZ81].

in Fig. 2.7. As the projectile approaches the target its charged core feels the effect of the Coulomb repulsion and, as a consequence, the width of the neutron halo is increased in the direction facing the target. This brings the surfaces of the two nuclei closer together and the nuclear forces can then drive the system into fusion with a substantially lower electrostatic repulsion.

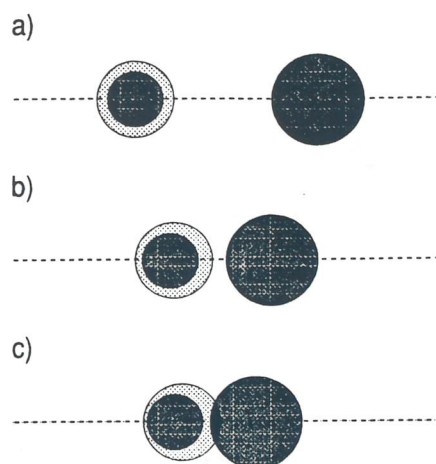


**Fig. 2.7** - Qualitative illustration to show the effect of a neutron halo bound by weak restoring forces on the dynamics of fusion. In a) the projectile (left) and the target (right) are far apart and the excess neutron cloud of the former is centered on its core. In b) the effect of the couplings has already displaced the spatial distribution of neutrons towards the target. Finally, in c) it is seen that the overlap of nuclear densities starts to occur with a considerable separation of the charge distributions, thus strongly lowering the effective fusion barrier.

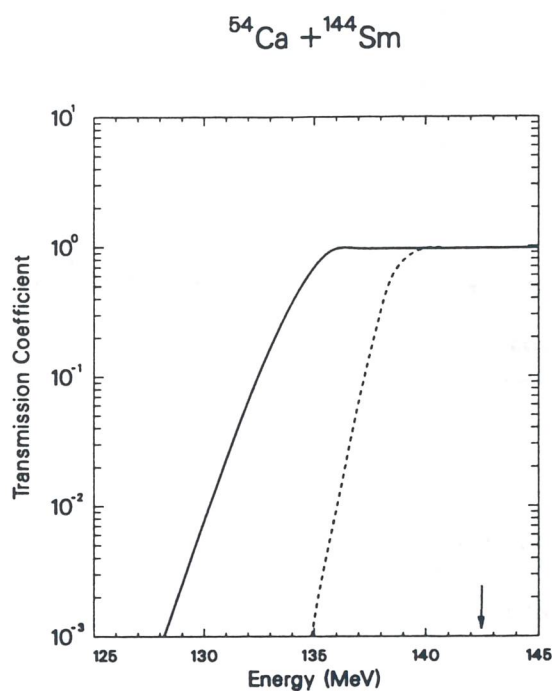


**Fig. 2.8** - Transmission coefficients for partial wave  $\ell = 0$  as a function of center-of-mass energy for the reaction  $^{54}\text{Ca} + ^{144}\text{Sm}$ . The full-drawn and dashed curves correspond to values of the deformation parameter  $\beta = 0.15$  and  $\beta = 0.10$ , respectively. The arrow indicates the position of the nominal Coulomb barrier.

In Fig. 2.8 we show the fusion probability for  $^{54}\text{Ca} + ^{144}\text{Sm}$ , calculated according to [DAS92], as a function of the incident energy and for two characteristic values of the deformation parameter  $\beta$ . It is found that the coupling to the soft-dipole mode brings the transmission coefficient to appreciable levels at 10 or 20 MeV below the nominal Coulomb barrier. It is important to stress that this dynamical effect comes in addition to the static one generated by the large size of the neutron halo. We should further note that projectiles and targets used for these kind of reactions may also have considerable quadrupole deformations; this factor by itself is expected to produce significant enhancements of the sub-barrier fusion cross sections [DAS90].

The potential of these processes for the synthesis of superheavy nuclei is not easily predicted. An interesting possibility could be for instance  $^{54}\text{Ca} + ^{244}\text{Pu}$ , a combination that leads to the elusive  $Z=114$  nucleus. Also in this case (cf. [DAS92])) the enhancement obtained is equivalent to an effective reduction of the barrier by tens of MeV. However, the speculative nature of these results should be emphasized. In fact, in situations involving very heavy systems the strong Coulomb forces acting during the collision can disrupt the evolution of the system and cause it to follow reaction paths into channels different from the one of compound nucleus formation [ILJ82, SWI82]. Estimates of superheavy element formation that do not take into account these effects cannot be considered reliable.

### 2.3.3 Transfer and Deep Inelastic Reactions

Transfer reactions are among the dominant channels at near- and sub-barrier energies; the availability of exotic nuclei with loosely bound nucleons allows the onset of such reactions at larger internuclear distances than have been observed so far. In fact, most of the appeal of exotic beams in nuclear reactions stems from the possibility for nuclei to interact, at large distances, by neutron exchange that may lead e.g. to large enhancements of subbarrier fusion or to the early onset of necks. This would be very useful in investigating the connection of transfer with fusion, namely its role as a doorway step that has yet to be satisfactorily explained.

Furthermore, as the interacting ions become heavier and heavier an increasing fraction of the cross section is found experimentally to consist of deep inelastic events [WOL87]. A key question then applies to the interplay of all these reaction channels, a very difficult task in a microscopic theoretical approach. From an experimental point of view one needs precise and complete measurements identifying all quasi elastic transfer cross sections, possibly distinguishing the various final states populated, as well as the deep inelastic components. It would be worthwhile to study a few cases comprehensively: one should be able to make a detailed comparison between e.g. a collision of spherical, magic nuclei and nuclei with loosely bound neutrons from an exotic beam. Possible candidates could be  $^{56}\text{Ni} + ^{90}\text{Zr}$

(both spherical and the former unstable) and  $^{66}\text{Ni} + ^{96}\text{Zr}$ . To do this one needs large  $4\pi$  experimental set-ups where also  $\gamma$ -rays should be detected.

An accurate study of the enhancement factors of the cross sections for two-particle transfer reactions is very important for the study of the pairing correlations in nuclei. These studies are very important to establish an interesting analogy to a similar problem that occurs in solid state physics, i.e. the Josephson effect. One may expect to observe a nuclear Josephson effect with strongly enhanced two- and multi-nucleon transfer cross sections between superfluid nuclei. Enhancement factors for two-nucleon transfer have been studied by several groups [GAR88] in order to pave the way to the study of this effect. Now, the loosely bound nucleon pairs, as existing in exotic nuclei, are ideally suited to study such pairing correlations and in particular the onset of superfluid currents.

### 2.3.4 Elastic Scattering and the Nuclear Potential

A study of the nuclear optical potential would be particularly interesting with light halo nuclei such as  $^{11}\text{Li}$ , but also heavier, exotic projectiles may help to solve relevant open problems such as the size of the "fusion" (absorption) radius of the optical potential. Elastic scattering as well as fusion data indicate that the radius of the imaginary, absorptive potential extends much more than previously thought, beyond the barrier radius [UDA89], but the evidence is still ambiguous. Also interesting is the investigation of the so called threshold anomaly [FUL85], where the imaginary part of the potential drops to zero around the barrier (gradual closure of the absorption channels) and correspondingly the real part undergoes a sudden increase as expected from very general dispersion relations. This increase in the real potential (i.e. in the internuclear attraction) is reflected in the enhanced sub-barrier fusion. The use of exotic beams is essential in this respect because of the possibility to have much larger interaction radii.

We know that at energies close to the Coulomb barrier the dominant reactions are inelastic and Coulomb excitation, Coulomb break-up, few nucleon transfer and fusion and we know that all these channels play an important role for the optical potential, specifically for the understanding of its energy dependence.

Following refs. [BRO81, DAS86] the correction to the folding real potential due to one-particle transfer reactions may be written in the form:

$$\begin{aligned}\Delta U(r) &= \Delta V(r) + iW(r) \\ &= (...) \sum_{ij} |F_{ij}(r)|^2 [p(\lambda_{ij}, Q_{ij}) - ig(\lambda_{ij}, Q_{ij})]\end{aligned}$$

where  $F_{ij}(r)$  are the one-particle transfer formfactors and the sum has to be performed over all the single-particle transitions between projectile and target.

The functions  $p(\lambda, Q)$  and  $g(\lambda, Q)$ , that weigh the contribution of the transitions, are function of the  $Q$ -value and of the angular momentum transfer  $\lambda$ . Neglecting the dependence on the angular momentum these functions are shown in Fig. 2.9 as a function of the  $\omega = -(Q_{ij} - Q_{eff})$ . From the figure one sees that the contribution to the imaginary potential peaks at  $\omega = 0$  and drops off rapidly, while the contribution to the real potential is antisymmetric about  $\omega = 0$  and decreases slowly for large  $\omega$ . These results provide an insight into the nature of the effective potential since the dependence on the relevant parameters (i.e. number of states,  $Q$ -values and angular momentum transfer) appears explicitly in the expression. For the inelastic channels one can write a similar expression (for more details see refs. [ILJ82, SWI82, BRO81, DAS86]).

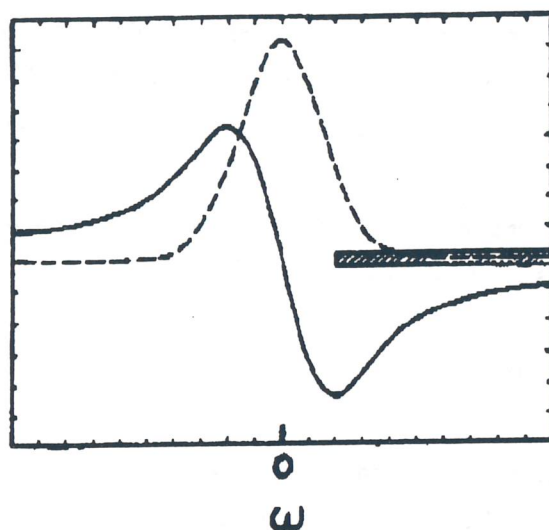


**Fig. 2.9** - Behaviour of the functions  $p(\lambda, \omega)$  (full line) and  $g(\lambda, \omega)$  (dashed line) as a function of  $\omega = -(Q - Q_{eff})$  for a distribution of channels (hatched bar) that is representative in the case of nuclei in the stability valley. Both scales are in arbitrary units.

From the distribution of the relevant channels in  $Q$ -value ( $\omega$ ) one can make some interesting points. Inelastic excitations and negative effective  $Q$ -value ( $\omega > 0$ ) transfer reaction channels give rise to negative correction to  $\Delta V$ , thereby increasing the nuclear attraction. For an equal distribution of channels over positive and negative  $\omega$ -values there will be contribution to the absorption and not to the polarization. For nuclei in the stability valley these are the only two regions that can be explored. With exotic beams one has available many reactions with transfer channels characterized by positive  $Q$ -values. In these cases the correction to  $\Delta V$  is positive, thereby giving rise to a reduction in the nuclear attraction. Of course this behaviour will be contrasted from the existence of the low-lying soft dipole mode. Another important channel that can contribute to the optical potential and that is not included in the above formulae is the break-up.

For nuclei in the stability valley the contributions of the reaction channels to the polarization potential are relevant only in a narrow range of energy close to the Coulomb barrier. This may not be the case for exotic nuclei. As recently calculated by Satchler [SAT91] the elastic scattering of  $^{11}\text{Li}$  on  $^{12}\text{C}$  at 30 MeV/u has a somewhat surprising behaviour. He found that, contrary to naive expectations, the neutron halo in  $^{11}\text{Li}$  does not increase enough the absorption so to transform the pattern of the elastic scattering angular distribution from refractive to diffractive. The predicted angular distribution is a factor of 2 larger than the Rutherford cross section in the forward direction and presents a very prominent minimum close to the grazing angle. This minimum is very sensitive to the value of the real potential in relation to the imaginary potential. One can conclude pointing out that the presence of the neutron halo may give very important information on the nature of the optical potential.

Elastic scattering experiments are relatively simple since they can be done even with low intensity beams by using large position-sensitive detectors. The main difficulty, with heavy systems, is the energy resolution, but we remind that very clean "true" elastic scattering has been measured recently in heavy ion collisions by means of kinematic coincidence techniques and with large acceptance momentum spectrographs with high-order compensation of kinematic shifts. This is shown in Fig. 2.10.

### 2.3.5 Spin Distributions

Fundamental questions, requiring unfortunately non-easy experiments, are connected with the spin distribution of compound nuclei in a fusion reaction. The angular momentum of the compound nucleus bears clues of the evolution during the reaction process. Moreover the partial-waves contributions to the reaction are directly related to the nuclear potential. A way to study this problem experimentally is to observe the  $\gamma$ -ray cascades originating from the evaporation residues. The availability of very large arrays of  $\gamma$ -detectors with high enough granularity and a solid angle coverage of nearly  $4\pi$  makes this type of measurement accessible. A very relevant theoretical problem is that the angular momentum involved in the fusion of medium-heavy nuclei around the barrier is considerably larger than predicted by those same theories that can satisfactorily account for the bulk of fusion and elastic scattering cross sections. This is a very open and debated question in the field of nuclear interactions around the Coulomb barrier. Experiments on spin distributions and even, more simply, on average angular momenta in collisions with exotic beams are crucial in this respect because they can involve extreme projectile-target combinations where one expects largely different results. An interesting example may be a comparison of the reactions  $^{66}\text{Ni} + ^{96}\text{Zr}, ^{100}\text{Mo}$  with existing data on  $^{64}\text{Ni} + ^{96}\text{Zr}, ^{100}\text{Mo}$  [KUH89, HAL89] shown in Fig. 2.11.

With an exotic beam of reasonable intensity of a "neutron halo" projectile another fundamental problem could be investigated: the minimum angular momentum of a compound

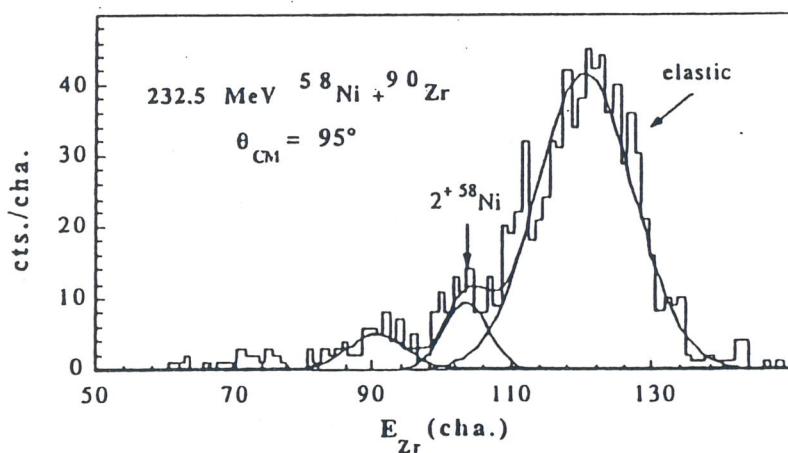
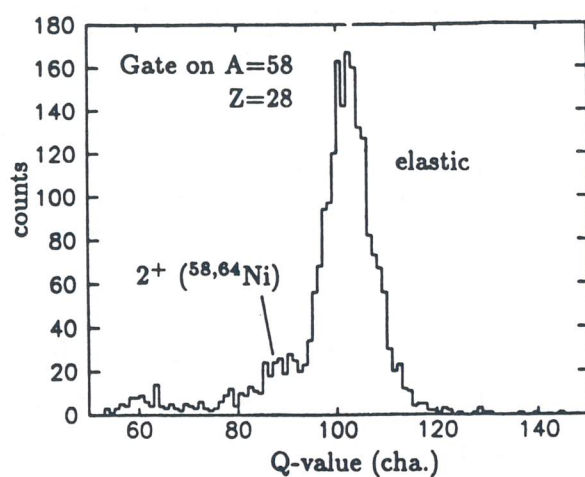
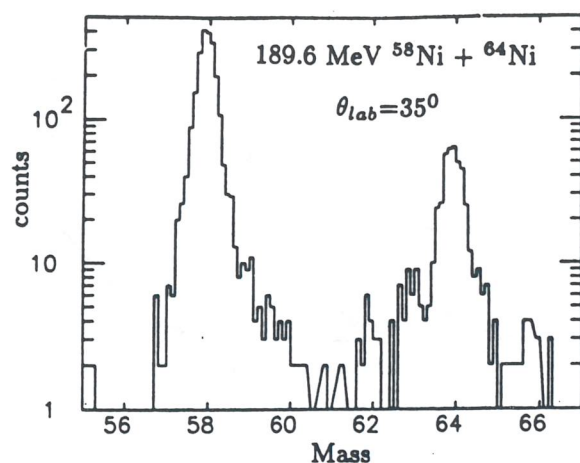


**Fig. 2.10** - Mass and Q-value spectra of elastic and quasi-elastic fragments from the  $^{58}\text{Ni} + ^{64}\text{Ni}$  reaction [STE90] (upper panel), and energy spectrum of Zr-like ions from  $^{58}\text{Ni}$  (beam) +  $^{90}\text{Zr}$  [COR91] (lower panel) at the indicated energies.

nucleus produced at very low energy. In fact theories predict that there is a minimum value which remains constant going down with the bombarding energy in the sub-barrier region.

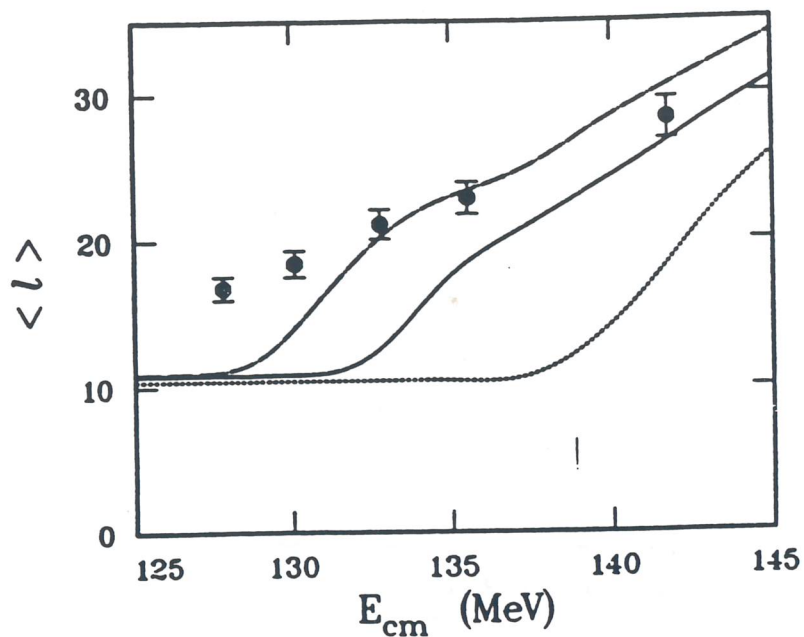


**Fig. 2.11** - Average angular momenta of the compound nucleus in the fusion of  $^{64}\text{Ni} + ^{100}\text{Mo}$  [HAL89]. Solid and dotted lines are the results of calculations with and without couplings to the quasi-elastic channels. The coupling strengths were arbitrarily increased by 50% for the dash-dotted line.

There is scanty experimental evidence so far that this actually occurs, but in a suitable combination of exotic beams and targets with a reasonable enhancement of the sub-barrier fusion this limit could be thoroughly tested.

## References

Specific references are quote below. In addition, we like to list here a number of reports and proposal on which we have heavily relied for the preparation of some points of these chapters:

- Isospin Laboratory, *Research Opportunities with Radioactive Nuclear Beams*, R.F. Casten *et al.*, report LALP91-51.
- A Proposal for Physics with Esotic Beams at the HHIRF, ed. by J.D. Garrett and D.K. Olsen, Physics Division, ORNL, Feb. 1991.
- Proc. II Int. Conf. on *Radioactive Nuclear Beams*, Louvain-la-Neuve, Belgium, 1991, ed. by Th. Delbar (Adam Hilger, Bristol, 1992).
- *Nuclear Physics in Europe: Opportunities and Perspectives*, NuPECC report, Nov. 1991.
- The Bevalac Upgrade, LBL Report PUB-5166, Mar. 1986.
- C.A. Bertulani and G. Baur, *Electromagnetic Processes in Relativistic Heavy Ion Collisions*, Phys. Rep. **163**, 299 (1988).

- [AGU88] C.E. Aguiar *et al.*, Phys. Lett. **201B**, 22 (1988).
- [AHN91] W. Ahner *et al.*, Z.Phys. **A341**, 123 (1991).
- [ARM85] P. Armbruster, Ann. Rev. Nucl. Part. Sci. **35**, 135 (1985).
- [BAY86] G. Baym, Proc. Int. Nucl. Phys. Conf., Harrogate, Vol. 2, 309 (1987).
- [BAY87] B.F. Bayman and Y.C. Tang, Phys. Reps. **147**, 155 (1987).
- [BAZ91] D. Bazzacco, Proc. Int. Conf. on *New Nuclear Physics with advanced Techniques*, Crete (1991).
- [BEC82] M. Beckerman *et al.*, Phys. Rev. **C26**, 837 (1982).
- [BER91] See e.g. G.F. Bertsch *et al.*, Ann. Phys. **209**, 327 (1991).
- [BRO81] R.A. Broglia, G. Pollarolo and A. Winther, Nucl. Phys. **A361**, 307 (1981); Nucl. Phys. **A406**, 369 (1983).
- [CAR91] M.A. Cardona *et al.*, Phys. Rev. **C44**, 891 (1991).
- [CAS90] W. Cassing *et al.*, Phys. Reps. **188**, 363 (1990).
- [COR91] L. Corradi *et al.*, JAERI Tandem Annual Report 1990, p.116
- [DAS83] C.H. Dasso *et al.*, Nucl. Phys. **A405**, 381 (1983).
- [DAS86] C.H. Dasso, S. Landowne, G. Pollarolo and A. Winther, Nucl. Phys. **A459**, 134 (1986).
- [DAS90] C.H. Dasso, J. Fernandez-Niello and S. Landowne, Phys. Rev. **C41**, 1014 (1990).
- [DAS92] C.H. Dasso and R. Donangelo, Phys. Lett. **276B**, 1 (1992).
- [DEA91] G. de Angelis *et al.*, Annual Report, Legnaro (1991).
- [DUD88] J. Dudek, T. Werner and L.L. Riedinger, Phys. Lett. **211B**, 252 (1988).
- [FUL85] B.R. Fulton *et al.*, Phys. Lett. **162B**, 55 (1985).

- [GAR88] J.D. Garrett *et al.*, Contemporary Topics on Nuclear Reactions, eds.
- [GEL91] W. Gelletly *et al.*, Phys. Lett. **253B**, 287 (1991). R.F.Casten *et al.*, (World Scientific, Singapore, 1988), p. 699
- [GER91] J. Gerl and R.M. Lieder, *Upgrading to EUROBALL* (1991).
- [HAL89] M.L. Halbert *et al.*, Phys. Rev. **C40**, 2558 (1989).
- [HAN91] P.G. Hansen, Nuclear Physics News, NuPECC, **1**, 21 (1991).
- [ILJ82] A.S. Iljinov, Yu.Ts. Oganessian and E.A. Cherepanov, Yad. Fiz. **36**, 118 (1982).
- [ISO91] Isospin Laboratory, *Research Opportunities with Radioactive Nuclear Beams*, R.F. Casten *et al.*, report LALP91-51.
- [IWA88] A. Iwamoto and N. Takigawa, Proc. JAERI Int. Symp. on Heavy-Ion Reaction Dynamics in Tandem Energy Region, Hitachi (Japan), August 1-3, 1988, eds. Sugiyama, Iwamoto and Ikezoe (Universal Academy Press, Tokyo, 1988) p. 29
- [JAN91] R.V. Janssens and T.L. Khoo, Ann. Rev. Nucl. Part. Sci. **41**, 321 (1991).
- [JUL91] J. Julien *et al.*, Phys. Lett. **B264**, 269 (1991).
- [KOB91] T. Kobayashi *et al.*, preprint 1991.
- [KRA91] A. Krasnahorkay *et al.*, Phys. Rev. Lett. **66**, 1287 (1991).
- [LIS85] C.J. Lister *et al.*, Phys. Rev. Lett. **55**, 810 (1985).
- [MAI82] G. Maino and A. Ventura, Lett. Nuovo Cim. **34**, 79 (1982); Nuovo Cim. **73A**, 1 (1983).
- [NuP91] NuPECC Report, p.29 (1991).
- [POE91] D.N. Poenaru and W. Greiner, *Radioactive Nuclear Beams*, Louvain-la Neuve, p.203 (1991).
- [PRI89] P.B. Price, Ann. Rev. Nucl. Part. Sci. **39**, 19 (1989).
- [PYW85] E. Pywell *et al.*, Phys. Rev. **C32**, 384 (1985).
- [SAT87] G.R. Satchler *et al.*, Ann. Phys. **178**, 110 (1987).
- [SAT91] G.R. Satchler *et al.*, Nucl. Phys. **A522**, 621 (1991).
- [SHI91] T. Shimoura, Proc. of Int. Workshop on Structure and Reactions of Unstable Nuclei, ed. Y. Suzuki, 1991, World Scientific.
- [SOR88] F. Soramel *et al.*, Phys. rev. **C38**, 537 (1988).
- [SPE91] *Giant Resonances*, ed. J. Speth, 1991, World Scientific.
- [SPO85] P. Spolaore *et al.*, N.I.M. **A238**, 381 (1985).
- [STE86] A.M. Stefanini *et al.*, Nucl. Phys. **A456**, 509 (1986).
- [STE88] P.H. Stelson *et al.*, Phys. Lett. **205B**, 190 (1988).
- [STE90] A.M. Stefanini *et al.*, Phys. Lett **240B**, 306 (1990).
- [SWI82] W.J. Swiatecki, Nucl. Phys. **A376**, 275 (1982).
- [UDA89] T. Udagawa *et al.*, Phys. Rev. **C39**, 1840 (1989).
- [VAZ81] L.C. Vaz *et al.*, Phys. Repts. **69**, 373 (1981).
- [WOL87] F.L.H. Wolfs, Phys. Rev. **C36**, 1379 (1987).

## Part B

1.1

### Medical and Applied Physics with ADRIA

now

app

the

ticular

are

part

treat

leth

to a

as

to

diag

as

of

int

rad

# 1

## Therapy with Heavy Charged Particles at ADRIA

### 1.1 Introduction

Since the original idea of R. Wilson at Harvard (1946), many efforts have been done till now to utilize proton and heavy charged particles for therapeutical application (radiotherapy) as alternatives to the electromagnetic radiation as well as complementary approach to the surgical, chemotherapeutical and immunotherapeutical treatment of tumour. In particular, the results obtained by the pioneer laboratories of Berkeley and Harvard in U.S.A. are promising and show the potential benefits which can be achieved through the charged particle therapy. In the last few decades a total number of about 9000 patients have been treated throughout the world.

The final goal of any radiotherapy project is to expose the tumour as a target to a lethal dose of ionizing radiation, sparing thereby the surrounding healthy (normal) tissues to a maximum extent. As a consequence, highly effective methods of localization of tumour as well as the local control of systemic treatments are required. Nowadays, it is possible to delineate the contours of a tumour with an extreme precision using the new improved diagnostic techniques, including computerized tomography (CT) with x-rays, magnetic resonance imaging (MRI) tomography and positron emission tomography (PET).

However, the precision of conventional therapy is limited mainly by the physical nature of the ionizing radiation i.e. the electromagnetic radiation. Heavy ions exhibit a different interaction mechanism with matter compared to the conventionally used electromagnetic radiation:

- They have a small range and lateral scattering which enables to fill complex target volumes within a precision of a few millimetres.
- They have an inverse dose profile with a low dose at the entrance channel and a high dose at the end of their range in the tumour.
- The elevated dose at the end of the range is connected to an increased biological effectiveness enhancing the killing of tumours cells for several reasons.
- Finally beams of ions like carbon, oxygen or neon produce a trace of radioactive isotopes which can be monitored from outside and can be used to control the position of the therapy beam (in beam PET).

## 1.2 Status of Conventional Radiotherapy

In conventional radiotherapy x-rays, Co  $\gamma$ -rays and bremsstrahlung from electron linacs are mainly used as radiation sources. The physics of the absorption of these types of electromagnetic radiation yield essentially an exponential decrease of the deposited dose with increasing penetration depth. For the low energetic x-rays a pure exponential depth dose relationship is found having a very limited penetration. With increasing average energy, the penetration depth increases and also the maximum of the energy deposition can be shifted from the outer layer, the radiosensitive skin to a few centimetres below the surface. Both, the shallower depth dose relation and the shift of the maximum of dose to greater depth for the electron bremsstrahlung increase the maximum tumour dose and the precision of the treatment to such a great extent, that most of the hospitals are now equipped with electron Linacs.

Presently, radiotherapy alone contributes to 12% to the total of 45% of five years survival of all cancer patients. Another 6% yields from the combined application of radiation and surgery, while surgery alone contributes to 25% and chemotherapy less than 5%. It is evident from these statistics that for the major fraction of all patients of 55% a successful treatment does not exist and an improvement of all types of tumour treatment is mandatory. However for conventional radiotherapy a further increase of the tumour dose is restricted by the physical properties which determine the dose given to the tumour bed and the healthy tissue around the tumour.

## 1.3 Heavy Charged Particle Therapy

### 1.3.1 Physical Advantages

Beams of heavy charged particles exhibit a completely different interaction mechanism when penetrating through tissue compared to electromagnetic radiation. Heavy charged particles interact mainly with the electrons of the penetrated material. At the high energies the interaction is weak but increases towards the end of penetration yielding a maximum of energy deposition very close to the end of their range in the so called Bragg peak (Figure 1.3.1). Moreover, due to the very different masses of projectile and target electrons, the projectiles are nearly not deflected by the collision process and a maximum precision in hitting a small target of a few millimetres can be achieved even for large penetration distances.

The physical properties of a beam of heavy ions are very favourable for a radiotherapeutical application: the precision of the treatment becomes comparable to the precision of the modern diagnosis using various types of tomography. Secondly, due to the inverse dose profile the target dose can be increased while simultaneously the healthy tissue around the tumour can be spared to a large extent.

The advantages of particle therapy over conventional therapy using x or  $\gamma$ -rays are given for all ions starting with protons up to heavier ions like carbon, oxygen or neon. An optimum of the physical dose distribution is reached for carbon ions because in this case the lateral and range straggling is drastically reduced compared to the lighter ions and nuclear fragmentation does not deteriorate the dose profiles as it is the case for neon and the heavier ions.

### 1.3.2 Biological Advantages

In addition to the physical properties of the particle beams, the changes of the biological effectiveness with the elevated ionization density have to be considered for the proper choice of heavy particle beams for therapy. For the very light ions the energy deposition events by the primary ion and the subsequent electrons are separated larger than the dimension of the molecular target inside the biological cell i.e. the DNA as carrier of genetic information. For these particles, the relative biological effectiveness (RBE) is the same as for the sparsely ionizing radiation ( $RBE=1$ ) and the biological effect is given by the total energy deposition. For the heavier ions, in the range of elevated energy deposition or elevated Linear Energy Transfer (LET), many ionization events occur closely together and produce correlated damage at the DNA. In this ionization range the deposited energy is biologically far more effective than at lower ionization densities. ( $RBE \geq 1$ ).

For the ions, in the range between carbon and oxygen, the elevated relative biological effectiveness corresponding to enhanced cell killing is restricted to the end of the particle range i.e. in the tumour volume. In the entrance channel before the tumour, the ionization density and biological effectiveness are low. Therefore these beams act like sparsely ionizing radiation in the healthy tissue but like densely ionizing radiation in the tumour. The differences in the biological action between entrance region of the beam and the tumour volume concern different biological reactions like the repair capacity, sensitivity to fractionated exposure, exposure under oxic and anoxic condition and the cell cycle dependent sensitivity as shown in Figure 1.3.2.

### 1.3.3 In Beam PET Monitoring of the Beam Localisation

Finally, beside the extreme precision of the dose delivery and the elevated biological effectiveness there is a third reason favourable for the use of particle beams in therapy. Heavy charged particles when penetrating through a tissue of a depth of several centimetres undergo nuclear reactions. Some of these reactions having a probability of less than 1% result in positron emitting isotopes. These isotopes have mainly the same direction and nearly the same range as the primary beam. Their stopping point can be monitored by a coincident detection of the two annihilation  $\gamma$ -quantas emitted by the positron. Using appropriate  $\gamma$ -cameras it is possible to monitor in vivo the penetration and the localisation of the primary particle beam.

### 1.3.4 Energies and Intensities of the Particle Beam

In order to irradiate a deep seated tumour the penetration of the particle beam has to be sufficient to reach any position inside the human body. This is possible for a particle range of 15 cm in tissue. However, heavy ion therapy will be applicable frequently for those cases where the tumour is located close to a radiosensitive organ like the spinal cord. In these cases the shortest entrance channel is not always the most appropriate way to irradiate a tumour volume and a larger penetration would be useful. In practice, ranges of 20 to 25 cm are sufficient for any treatment which corresponds to energies of 200 MeV/u for He-ions,

400 MeV/u for C-ions, 450 MeV/u for O-ions and 500 MeV/u for Ne-ions. These ranges for clinically interesting energies could be easily achieved with ADRIA (see for instance, Table 1.3.1).

Other important questions are the required beam intensities. In order to apply a dose of 2 Gy to a target volume of 1 litre in less than one minute a primary intensity of  $10^9$  particles per second is always sufficient. However, the particle fluency necessary to achieve a certain dose depends on the size and the depth of the target volume. In Table 1.3.2, the different modalities are compared.

Beam intensities between  $10^8$  to  $10^9$  particles per second represent an optimum value. Lower intensities will prolongate the exposure time, higher intensities are difficult to spread over the target volume using a magnetic scan system.

**Table 1.3.1: Penetration Ranges of Clinical Interest**

Ion	Energy (MeV/u)	Range to Bragg Peak (cm)
$^{12}\text{C}$	400	26
$^{20}\text{Ne}$	670	32
$^{28}\text{Si}$	670	23.2
$^{40}\text{Ar}$	500	12.3

**Table 1.3.2: Beam intensities for 6 Gy l/min in  $1000\text{ cm}^3$  volumes**

	Desired Beam Intensity (ions/s)		
	400	200	50
Area ( $\text{cm}^2$ )			
Depth (cm)	2.5	5	20
Helium	$3.4 \times 10^9$	$2.4 \times 10^9$	$1.1 \times 10^9$
Carbon	$6.7 \times 10^8$	$4.5 \times 10^8$	$2.2 \times 10^8$
Neon	$3.0 \times 10^8$	$2.3 \times 10^8$	$1.0 \times 10^8$
Argon	$1.1 \times 10^8$	$7.8 \times 10^7$	$3.8 \times 10^7$

## 1.4 Technical Set-up

### 1.4.1 Magnetic Scanning Technique

Maximum success of heavy ion therapy can be expected when the irradiation will be the most conform to the shape of the tumour and the dose outside the tumour minimum. In particular it has to be avoided that the highly efficient part of the particle beam, i.e. the Bragg peak ions with the elevated RBE values, hits the healthy tissue around the tumour. For the dose delivery systems presently in use at the LBL Berkeley and designed for the heavy ion treatment in Chiba, passive beam shaping techniques are preferred because of their simplicity. However, using passive beam shaping it is not possible to achieve a complete tumour conform treatment and the tumour dose is widely determined by the tolerance of the tumour bed and the healthy tissue around. For a tumour conform treatment magnetic scanning technique like rasterscan have been proposed and are presently developed.

To irradiate an irregular shaped tumour with a rasterscan, the target volume will be dissected into slices of equal particle range (Figure 1.4.1). The slice will be irradiated sequentially starting with the most distant part. Each slice will be covered with a precalculated number of particles moving a sharp pencil beam in a zig-zag or other pattern over the slice. The writing speed has to be controlled by the beam intensity in order to achieve the required dose for each spot of the slice. Because of the different biological effectiveness of stopping and penetrating particles, each slice has to be covered with an inhomogeneous dose distribution to achieve a biological iso effect.

Only the magnetic scan technique can produce a true tumour conform treatment but this technique poses severe restrictions on the accelerator performance. Presently, first tests of magnetic scanning are performed at LBL Berkeley, GSI Darmstadt and PSI Villigen.

Magnetic scanning requires a time constant and slow extraction of the beam from the accelerator. Reasonable values for the rise time of the current in the deflection magnets ask for a stable extraction over a period of 400 to 500 msec in which one slice will be treated. During that time the beam intensity should be as constant as possible and only intensity changes, slow compared to the control of the writing speed, can be tolerated. Furthermore the beam has to be started and terminated on request from the magnetic scanning system. In addition, an active energy variation decreasing the particle energies stepwise in steps of a few percent on request from the scan system is necessary to shift the particle range from slice to slice of the target volume.

### 1.4.2 Beam Monitoring

The monitoring of the particle beam during the exposure of the patient is of utmost importance for the treatment procedure. First, the writing velocity of the magnetic scanning system has to be controlled by the intensity of the incoming beam. Second, independent control of the position of the beam immediately before the patient is necessary for the safety of the patient.

Monitoring of a particle beam at intensities of  $10^8$  -  $10^9$  particles per second is extremely difficult because the transition frequency of electronic components is mostly in the range of one to a few megahertz. Therefore it is principally not possible at this particle intensity to

monitor the individual particles. Instead, for the incoming beam the emission of secondary electrons from thin foils can be utilized as an integrating monitor used to control the power supplies of the scanning magnets. For the position sensitive monitoring in front of the patient large wire chambers have to be developed which are operated in ionization mode but not in single particle mode.

The on-line monitoring in front of the patient is necessary for a fast cut off of the beam in case of malfunctions of the scanning system or the accelerator. The in vivo PET technique is not fast enough because it needs a mathematical reconstruction of the image.

## 1.5 Layout of a Treatment Cave

If experimental treatment of a few hundred patients a year is planned, a single treatment area is sufficient. This cave should be preferably equipped with a horizontal and an oblique beam line which allows to simulate, at least partially, a multiform treatment as given by moveable gantry systems. The treatment cave should have easy access from outside and it has to be equipped also with a patient couch, since the highest reproducibility is achieved when the patient is treated in a horizontal position resting in an individually formed plastic mold.

The dimension of this cave could be similar to the Berkeley or Darmstadt cave of approximately  $6 \times 10 \text{ m}^2$  with 1.5 m concrete shielding around the cave. However it is advisable to incorporate a beam dump in forward direction at the end of the cave where the beam can be stopped for beam tuning or when the cave will be used for the testing of other equipments. This beam dump will be made of a block of iron of 1 m by 1 m extension perpendicular to the beam and 1.5 m in beam direction. The beam should be stopped in the first third of the iron block. The iron block should be followed by another 2 m of concrete in order to stop the neutrons produced in forward direction. Such shielding allows to work outside the cave during the time when the beam is in the cave.

In addition to the layout of the treatment area, rooms for the preparation of the therapy, waiting rooms for the patient and rooms for the physicians, have to be installed. In total approximately  $300 \text{ m}^2$  of additional rooms are necessary in order to accommodate for patients, physician, physicist, medical control room, computer rooms, photolab and so on.

## 1.6 Perspective of Radiotherapy for the ADRIA Project

In spite of the very favourable properties of heavy ions for therapy the high cost for the acceleration of heavy particles prevent from a common use of these particles in therapy. An experimental treating therapy program for approximately 100 patients a year is performed at LBL Berkeley. In National Institute of Radiological Sciences (NIRS) at Chiba, Japan, a dedicated facility for the treatment of tumour patient with heavy ions is presently under construction and will be starting with full phase treatment in the next year. At GSI a preclinical program for the development of an advanced heavy ion therapy using magnetic scan techniques is presently under progress.

It is common to all these programs that only a limited number of patient will be treated with heavy ions. Therefore an additional treatment facility at LNL, Legnaro, would increase

significantly the number of patients to be treated with this ultimate radiation modality.

A set-up for tumour treatment would be a very favourable addition to the planned physics program because only a very limited amount of beam time of a few minutes is necessary for the treatment of one patient but the time for the precise set up of the patient and the control of the coordinates take half an hour to one hour. Therefore, a tumour program at the Laboratori Nazionali di Legnaro would not be in a large conflict to the physics program but it would enable the Italian therapy community to explore the borderlines of the outmost physical possibilities of cancer treatment in radiotherapy. Such a project is in accordance within the greater european effort of "Europe Against Cancer" program and a national effort in this field will proved to be useful for cancer management inside the European Communities. Acknowledging the fact that Radiotherapy can be considered as "applied radiobiology" and the experience acquired through radiobiological research with charged particles by the respective group at the Laboratori Nazionali di Legnaro, in closer collaboration with other international groups, the proposal for use of heavy ion for therapeutical treatments at the ADRIA facility seems to be natural and justified.

## 1.7 Summary

In summary, beams of heavy charged particles in the range of atomic numbers such as carbon, oxygen and neon represent the useful tool for the radiotherapy of solid tumours. They travel virtually in straight lines, having negligible sideways spreading and characteristic deposition of large fraction of energy at the path-end. Their action is comparable to knife of the surgeon: heavy ion beams have a precision of a few millimetres and a high efficiency in the tumour volume. In addition it is also possible to control the position of this knife precisely and in vivo using the PET techniques.

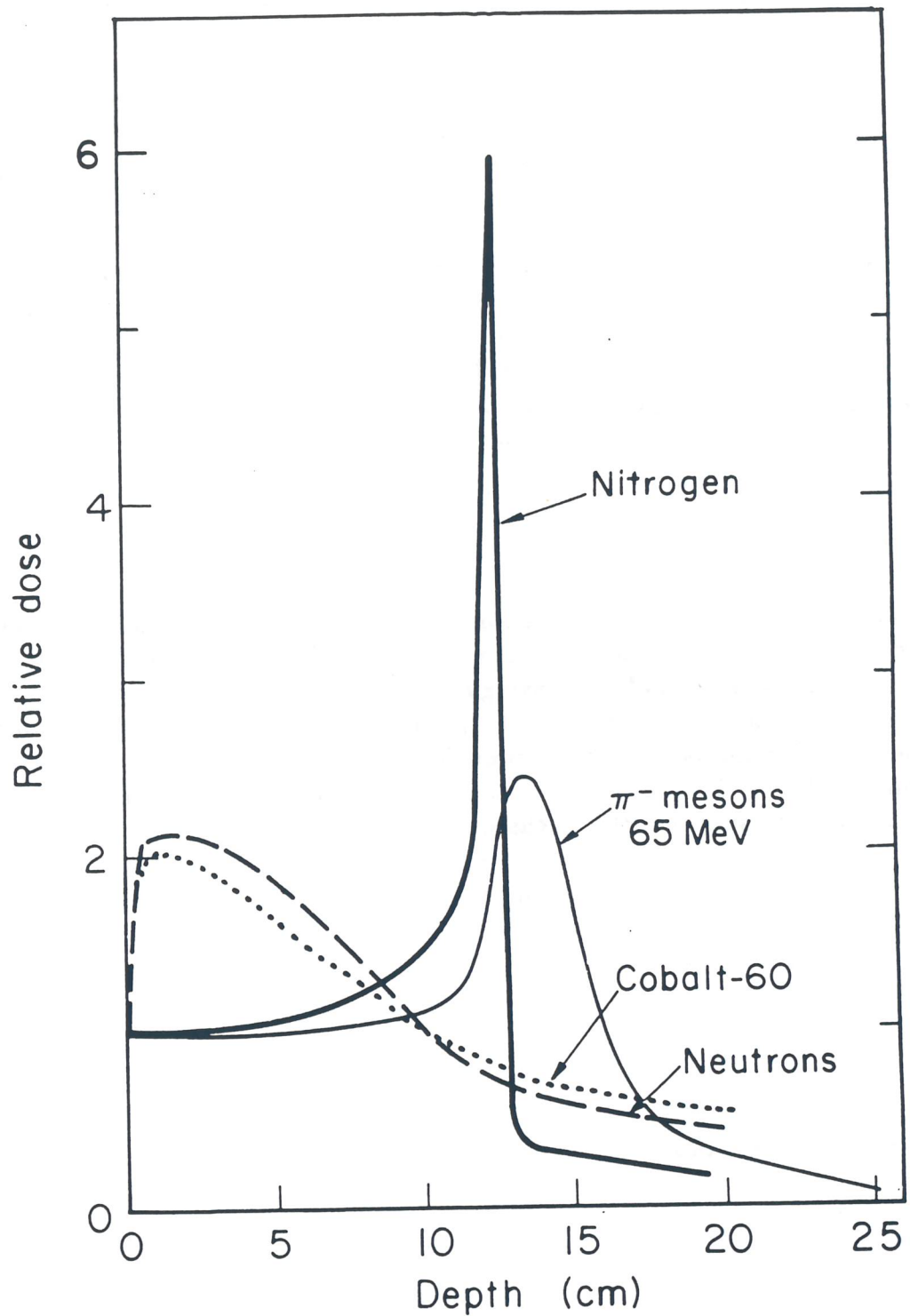


**Figure 1.3.1:** Comparison of the depth dose distribution of Co  $\gamma$ - rays, neutrons, negative pions and nitrogen beam. For x-rays and neutrons the integral dose in the entrance channel is higher than a dose for a deep seated tumour. Particles like ions and pions exhibit an inverse dose profile which allows to increase the tumour dose and to spare the healthy tissue.

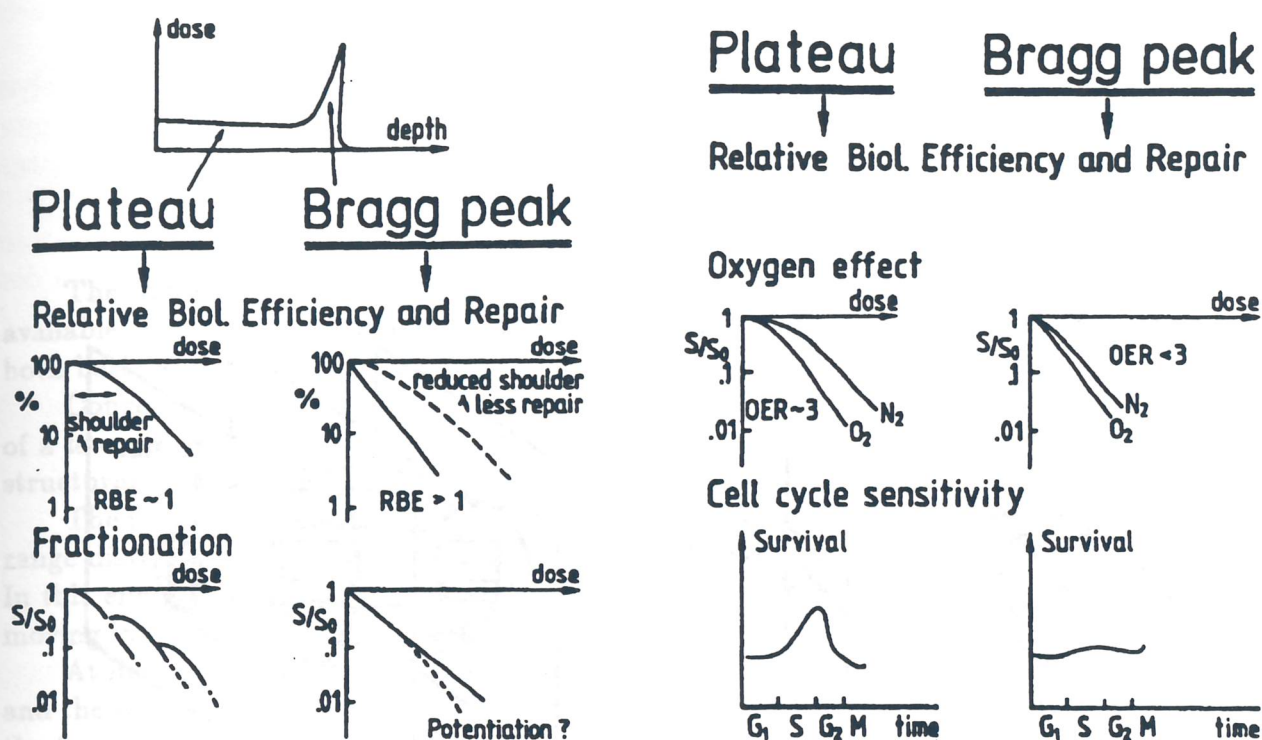


**Figure 1.3.2:** Comparison of the different biological action of heavy ion beam in the entrance region and the tumour region (for explanation of this figure, see the following texts).

**Repair and Fractionation.** In the region of low linear energy transfer (LET), cell survival is characterized by a large repair capacity corresponding to an extensive shoulder in the survival curve. The high LET regime exhibits reduced repair and an exponential or nearly exponential survival curve.

**Fractionation.** In the high LET regime, a drastically diminished fractionation effect has been observed. A potentiating of the radiation damage of a few percent has been found for fractionated treatment, but the potentiating effect will not play a major role for therapy. However, the diminished repair in the tumour volume and the full repair in the entrance channel will be of clinical relevance.

**Oxygen Effect.** At low LET values, the radiation sensitivity of hypoxic cells can be reduced by a factor of three compared to oxic cells. For high LET radiation, these differences are decreases and for LET values around  $100 \text{ keV}/\mu\text{m}$ , both types of cells, oxic and hypoxic, exhibit the same radiation sensitivity.

**Cell Cycle Sensitivity.** In vitro cell cultures show differences in radiosensitivity of more than one order to magnitude when exposed to sparsely ionizing radiation in different phases of the cell cycle. This is true, especially for cells in late S phase which are radioresistant when compared to G<sub>1</sub> phase cells. In the high LET range, these differences are diminished and cells in different phase have the same radiosensitivity independent of the cell cycle. This reduces important differences in the radioresponse of slowly proliferating cells of the healthy tissue and the fast proliferating tumour cells.

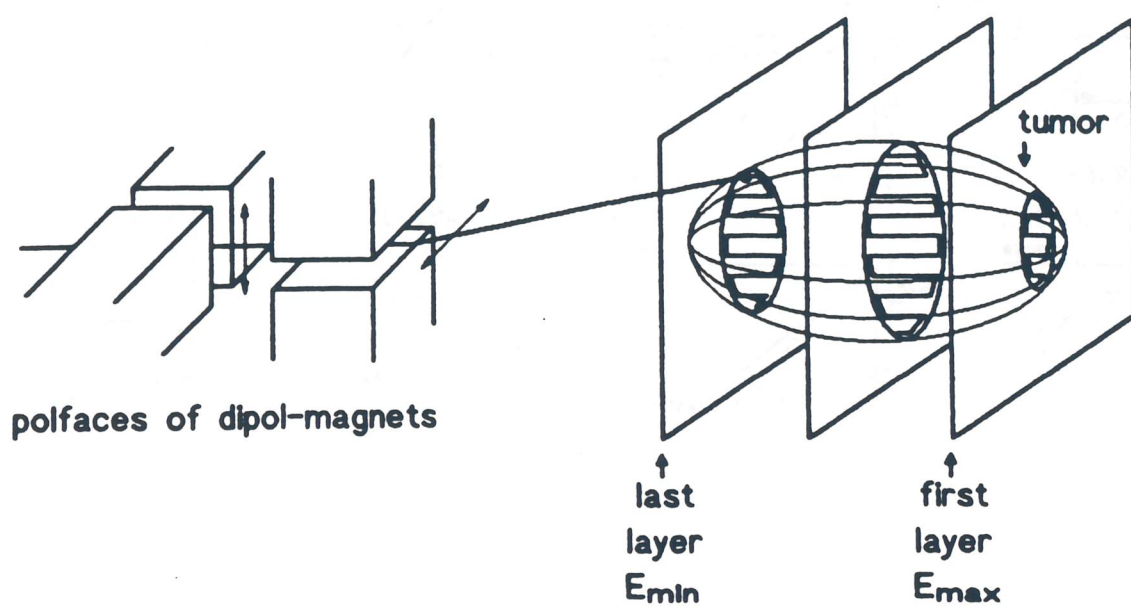


**Figure 1.4.1:** In the raster scan technique a pencil beam is deflected by two fast scanning magnets over different sections of the tumour. In order to achieve a homogeneous biological effect in each point of the tumour the writing velocity is controlled by the beam intensity.

## 2

# Applied Physics at ADRIA

The variety of accelerated ions (up to Uranium) combined with the wide range of available energies and intensities of the beams ( $10^{12}$  ions/s) permits the development of both basic and applied physics.

Concerning that the accelerated ions can penetrate in the solid targets for thickness of a few millimetres, the main practical applications involve all those research fields where structural and compositional modifications of the surface are important.

The first step for application of high energy implants requires a detailed knowledge of the range distribution. At energies of tens or hundreds of MeV few measurement are reported. In this energy range the main process responsible of slowing down is the interaction of the moving ion with the electrons of the crystal.

At high energies the damage distribution coincides practically with the ion range profile and the fact that near-surface regions are relatively undisturbed is of practical advantage in the formation of deep wells several microns beneath the surface.

The main physical effects along the path of the ions during the process of slowing down in the matter are related to the creation of points and extended defects, which directly induce variations of macroscopical properties (electrical, optical, mechanical etc.).

The interest in high energy ion implantation is also determined by the useful features that this method has for microelectronics technology, in particular:

- a. the possibility of introducing doping impurities to high depths which makes it possible to reduce or to eliminate a prolonged heat treatment;
- b. the possibility of creating buried layers using the peculiarities of impurity depth profiles formed by high energy ion implantation;
- c. An increase in the degree of integration and so the possibility of creating three-dimensional integrated circuits.

Since the basic advantages of high energy ion implantation are the substantial depth of penetration and the localization of the impurities at this depth, it is meaningful to use light ions. For this reason, when doping Silicon by high energy ion implantation, it is expedient to use the lightest alloying impurities, i.e. Boron and Phosphorous, which create in Silicon layers of p-type and n-type, respectively.

For example, in III-V devices, MeV implantation can be used to form buried insulation layers or buried channel charge-coupled devices (CCDs), while in Silicon similar implants are used for complementary metal-oxide semiconductors (CMOS) well formation. The formation of buried collectors in bipolar transistors, buried interconnects, or deep getting layers are also further applications of MeV range implantation. In addition, there have been several recent reports of the use 120 MeV Oxygen ion irradiation for varying the critical currents and transition temperatures of various oxide superconductors.

Particular interest is also given to the possible application in polymer science.

Processes of depolymerization are induced by high energy ion irradiation with a consequent release of elements (H or O) or of groups of elements, leaving a new altered structure rich of carbon, with modified optical properties (transmission, reflectivity, absorption, refractive index,...). Furthermore the depolymerization processes induce morphological surface variations which greatly improve the adhesion of possible coatings.

Very interesting studies can be performed on the compositional modification of polymer structures due to the possibility of using the broken bonds in order to fix new elements to the polymer. It is evident the possible development of the research in the biotechnological field.

An other application of high energy ion beams consists in the possibility to create micro-holes of few nanometres of diameter in organic materials, mainly at high irradiation doses. This can be used for filtering purposes in the biomedical field.

## Part C

# The ADRIA Technical Proposal

# 1

## General Overview

A proposal of an accelerator complex for the Laboratori Nazionali di Legnaro (LNL) is described in this conceptual design report. The main components of the complex are a Heavy Ion Injection system and two rings, a Booster and a Decelerator, both with a maximum rigidity of 22.25 Tm, connected by a Transfer Line where exotic isotopes are produced and selected. The proposal has two main goals:

- a. Acceleration of stable ion species up to kinetic energies of the order of few GeV/u, at a repetition rate of 10 Hz with intensities of about  $10^{12}$  ions per second, for fixed target experiments in nuclear physics.
- b. Production of fully stripped radioactive beams, using particle fragmentation method, for nuclear spectroscopy experiments. Fragments are accumulated in the Decelerator, with intensities  $10^8 \div 10^9$  ions/s, cooled and delivered at the production energies or decelerated down to energies of few MeV/u, in proximity of the Coulomb barrier.

### 1.1 The ADRIA Complex

The schematics of the ADRIA complex is given in Figure 1.1.1 and its location on the LNL site is shown in Figure 1.1.2. The individual components are the following:

- a Heavy Ion Injector (XTU tandem and the ALPI post-accelerator);
- a Fast Cycling Synchrotron (Booster);
- a Slow Cycling Synchrotron (Decelerator);
- a Transfer Line (connecting the two rings);
- an Experimental Area;

The two accelerators have the same size and similar lattices. They can hold beams of particles with magnetic rigidity of 22.25 Tm, and are arranged in a vertical layout with the Decelerator exactly on top of the Booster and 2.5 metres above it. Both rings are housed in the same enclosure with the Booster beam axis 1.5 m below the ALPI line. The lattices of the two rings have been designed to allow enough drift space for rf cavities, components for injection and extraction, and other devices. A fourfold superperiodicity has been found convenient, with each superperiod made of a  $90^\circ$  arc and a 22 m long straight section. The arcs are made of FODO cells 11 metres long. The betatron tunes are 5.8 (H) and 3.8 (V), away from any low-order systematic resonance. The transition  $\gamma$  of 4.6 is high enough to be avoided by all acceleration cycles.

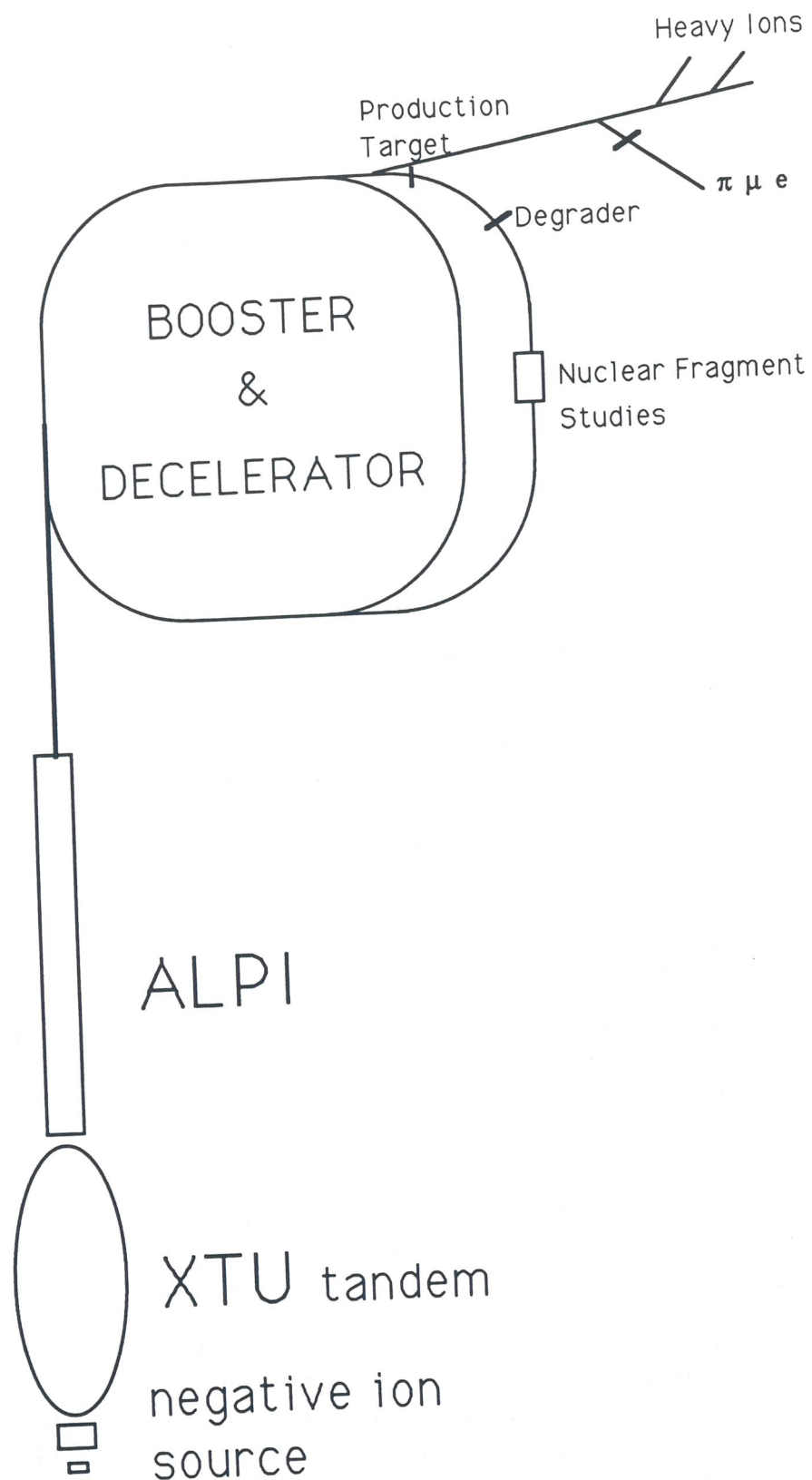


Figure 1.1.1: Schematics of the ADRIA Complex

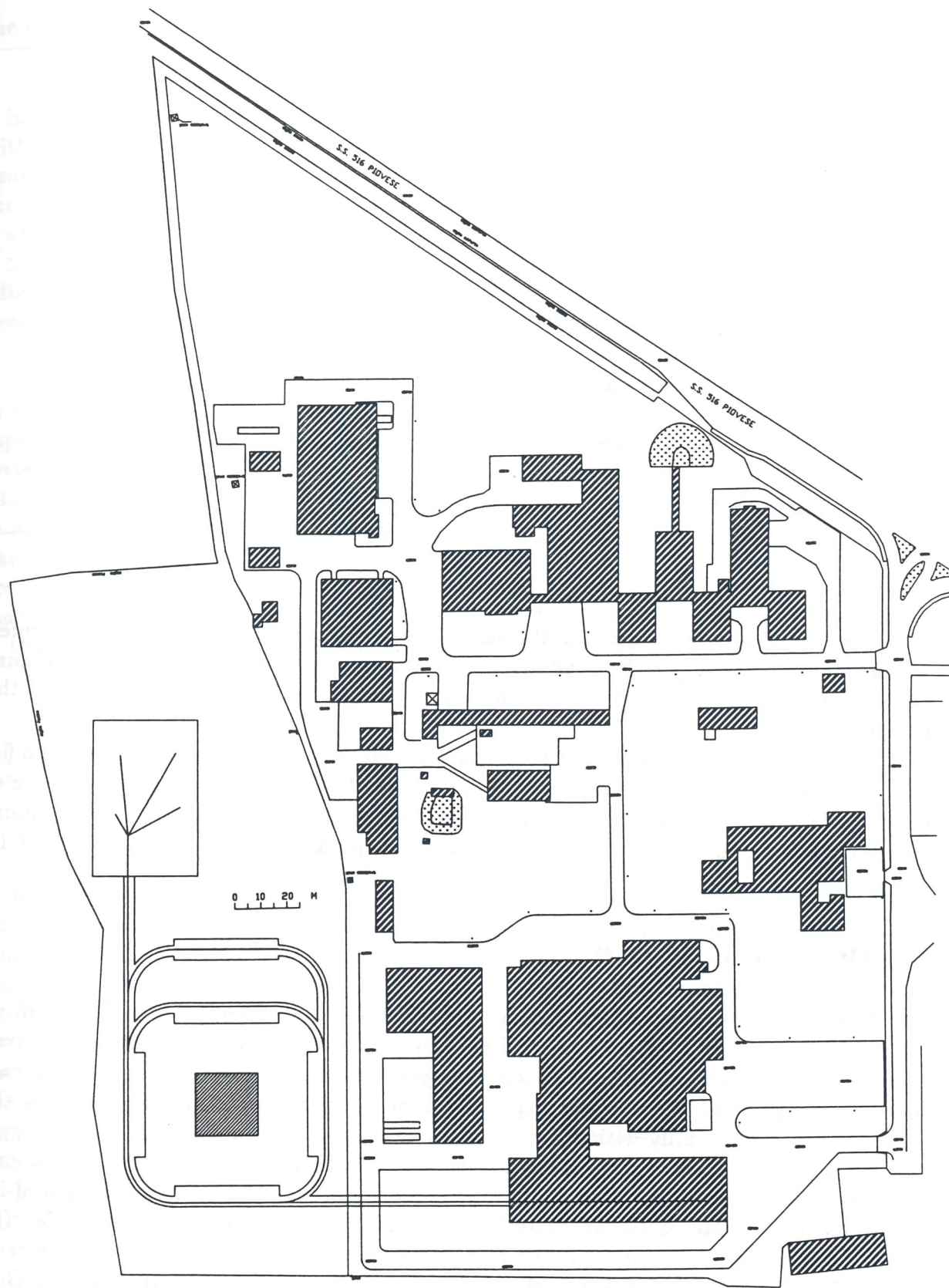


Figure 1.1.2: The ADRIA Complex on the LNL Site

**Table 1.1.1: General Lattice Parameters of the Two Rings.**

Maximum Magnetic Rigidity	22.25	Tm
Circumference	266.6667	m
Bending Radius	17.62	m
Maximum Dipole Field	1.26	T
Dipole vertical gap	10	cm
Maximum Quadrupole gradient	9.0	T/m
Quadrupole bore radius	7	cm
Superperiodicity	4	
Transition Energy ( $\gamma_t$ )	4.6	
Betatron tunes:		
Horizontal plane $\nu_h$	5.8	
Vertical plane $\nu_v$	3.8	
Natural Chromaticity:		
Horizontal plane $\xi_h$	-5.5	
Vertical plane $\xi_v$	-4.9	

The Decelerator has basically the same lattice of the Booster, the same circumference and geometry, except for the long straight sections; a different quadrupole configuration allows a magnet-free drift space 11.5 m long, to accommodate electron cooling of the ion fragments.

Dipole magnets have a gap of 10 cm, are 3.5 metres long and have a maximum field of 1.26 T. The excitation of the dipole field has a rate of 38 T/s. The physical aperture of the quadrupoles is circular with 7 cm radius. The number of power supply busses is minimized for easy tracking and tuning. A summary of lattice parameters is given in Table 1.1.1.

## 1.2 Heavy Ion Source

The Laboratori Nazionali di Legnaro own and operate a Tandem Van de Graaff with a terminal voltage of 16 MV, used to accelerate continuous beams of heavy ions. Essentially all ion species up to lead can be accelerated at large intensities; acceleration of uranium requires source development. We propose a pulsed mode of operation of the Tandem, as already demonstrated successfully with a similar machine at Brookhaven National Laboratory. This mode of operation makes the Tandem the ideal injector for a heavy ion facility which employs a fast cycling synchrotron. A negative ion source is pulsed with a pulse duration of 360  $\mu$ s at the repetition rate of 10 Hz. The following analysis is based on the example of Gold. In the scheme proposed here, the ions are accelerated towards the high voltage terminal (+16 MV), where they hit a target and are partially stripped. In the case of Gold an intermediate charge state of +13 is obtained, and the ions are further accelerated from the positive terminal toward ground where they exit the Tandem. One virtue of the Tandem is that it is able to deliver intense beams without sacrificing the small betatron emittance and momentum spread typical of electrostatic machines. The specific kinetic energy of  $\text{Au}^{+13}$  at

the exit of the Tandem is about 1 MeV/u.

At the Laboratori Nazionali di Legnaro the construction of a linear accelerator (ALPI) is in a completion phase; the project is made of superconducting cavities at 80 and 160 MHz with the equivalent of 40 MV accelerating voltage. The project will allow acceleration of heavy ions to an energy of 5-30 MeV/u depending on the species and charge state. For the proposal described here, ions of Gold with charge state +13 are accelerated through a section corresponding to a total voltage of 36 MV; at the end of this section, where  $\beta > 0.08$ , they hit a second stripping target where a new charge state (+51) is produced. After acceleration through the final 4 MV section of the linear post-accelerator the final beam energy is 4.6 MeV/u, corresponding to  $\beta \sim 0.1$ .

The time structure of the ALPI beam is generated by a 5 MHz pre-buncher located at the Tandem entrance, with a compression system (buncher) made of 80 and 160 MHz superconducting cavities located at the entrance of the post-accelerator. With this bunching system only one bucket in 32 will carry beam at the exit of ALPI. In the near future an alternate injection system to ALPI will be available; this consists of a ECR source coupled to an RFQ device. This new injector can be used to complement the performance of the Tandem with a different range of charge states, energies and intensities. Which of the two pre-injectors can be more used for filling of the ADRIA complex will depend on the mass of the ions and of the experience at hand at the time. In the following we shall limit our study to the case of the Tandem-ALPI combination as the injector to ADRIA.

### 1.3 Injection and Acceleration in the Booster

The circumference of the Booster has been chosen to correspond to the injection of 45 bunches of Gold ions per turn; the number of turns that can be injected is about 40. The rf harmonic at injection is also 45, corresponding to an injection frequency of 5 MHz, equal to the pre-buncher frequency. With this choice, all the rf buckets are occupied by beam bunches, except for the gap required for beam extraction. Each injected bunch is very short, about 1/50 of the length of the rf bucket. Thus a "painting" procedure can be applied to the multi-turn injection of the heavy ions to fill the rf buckets uniformly. At the end of the process about  $5 \times 10^{10}$  ions of Gold have been injected. The resulting tune depression due to space charge is estimated to be 0.5, assuming that the beam fills essentially all the available aperture; this yields a normalized betatron emittance of  $12 \pi$  mm-mrad. The beam is then accelerated to 1 GeV/u at a rate of 10 Hz, yielding  $5 \times 10^{11}$  ions of Gold per second. Even higher intensities and energies can be obtained with lighter ions. The maximum dipole field required for this mode is less than 1.3 T, and the maximum rate of change is 38 T/s.

A peak voltage of 220 kV is required during the acceleration cycle; the beam velocity varies between  $\beta = 0.1$  and  $\beta = 0.9$  requiring a large frequency swing from 5 to 45 MHz. This is accomplished with two rf cavity systems: the first operates from 5 to 32 MHz, the second from 30 to 45 MHz. A summary of beam parameters at the end of the acceleration cycle in the Booster is given in Table 1.3.1

**Table 1.3.1: General Parameters of Heavy Ion Acceleration.**

	S	Cu	I	Au	U	
Atomic Number Z	16	29	53	79	92	
Mass Number A	32	63	127	197	238	
Charge State Q	16	27	40	51	54	
Injection Kinetic Energy	16.4	10.4	6.1	4.6	3.9	MeV/u
Extraction Kinetic Energy	2.53	2.08	1.4	1.03	0.85	GeV/u
Harmonic number	24	30	39	45	49	
Beam Intensity	2.0	1.3	0.7	0.5	0.5	$10^{12}$ ions/s
Normalized Emittance	23	18	14	12	11	$\pi$ mm-mrad
Bunch Area	0.017	0.011	0.007	0.005	0.005	eV/u - s

Several modes of operation with heavy ions are possible: the beam can be extracted at the end of the acceleration cycle and sent toward external target stations; it can be also transferred to the Decelerator which can be used as a Stretcher, for energies up to few GeV/u, with slow-spill extraction for 100% duty cycle.

The possibility of producing ion fragments, for the study of fusion processes etc., is examined next.

## 1.4 Fragment Production and Accumulation

A transfer line takes the beam from the Booster to the Decelerator. Along the transport the beam first encounters a target where fragments are produced, at about the same kinetic energy, with medium-to-large mass numbers, and completely stripped. Selection of the required fragment species is then obtained with a second target, called the *degrader*, placed in a region of large dispersion, and a system of collimators. The combination of the targeting and the focusing along the transport will allow the capture of a total momentum spread of 0.7% and a betatron emittance of  $20 \pi$  mm-mrad in both planes. The expected yield can be as high as  $1 \times 10^{-3}$  fragments per incident ion. The secondary beam is then injected into the Decelerator. Here the bunches of fragments are captured by a 45 MHz rf system, rotated in the longitudinal phase space to present a smaller momentum spread (0.1%) and displaced by an additional rf system to an off-momentum trajectory at a distance of 1.2%, where they are allowed to debunch. The required voltage for the bunch operation is 1.4 MV, which can be obtained with two cavities.

Electron cooling is applied to the beam on the stacking orbit. A new pulse is injected every 100 ms, which has to be matched by the electron cooling rate. While both transverse and momentum cooling take place, the more important requirement is the reduction of the beam momentum spread by an order of magnitude. This process repeats until 12 pulses have been stacked (Figure 1.4.1); electron cooling then continues for a further 0.5 seconds, in conjunction with stochastic cooling. Finally the beam can be decelerated from the energy of

the fragments at production, down to about 5 MeV/u, which is near the Coulomb potential barrier energy. The deceleration lasts 0.3 s, and is followed by an interval of 0.1 s during which the field is reset to its initial value. At the end of the 2 second long cycle, the beam is extracted and directed to the experimental area. The beam momentum spread at this stage is 0.1%. A second step of electron cooling lasting about 100 ms can be applied just before extraction, for a further reduction of the beam momentum spread, for instance to 0.01%. The Decelerator can also be operated with an internal gas-jet target producing a high luminosity for precision experiments. Table 1.4.1 lists the main parameters of fragment production and accumulation.

**Table 1.4.1: General Parameters of Fragment Production.**

Target Length	1	g/cm <sup>2</sup>
$\beta^*$ @ target	1	m
Angular Acceptance (full)	7.5	mrاد
Momentum Acceptance (full)	0.7	%
No. of Booster pulses/cycle	12	
Minimum Cycle Period	2	s
Bunch Length (rms)	0.5	ns

	S	Cu	I	Au	U	
Mass Number, A	32	63	127	197	238	
Atomic Number, Z	16	29	53	79	92	
No. of Fragments/s	$4.0 \cdot 10^9$	$1.6 \cdot 10^9$	$5.0 \cdot 10^8$	$1.5 \cdot 10^8$	$1.5 \cdot 10^8$	
Momentum Spread (rms)	0.09	0.11	0.20	0.28	0.38	%
Angular Spread (rms)	3.2	3.7	5.0	5.8	7.3	mrاد
Harmonic Number	24	30	39	45	44	

Initial Emittance	20	$\pi$ mm-mrad
Final Emittance	1	$\pi$ mm-mrad
Final Momentum Spread	0.01	%

The cycle described above is only one example of the possible modes of operation of the Decelerator. The duration of the cycle as well as the extraction energy can be varied accordingly to the user requirements. It is also possible to adjust the rate and the length of the extraction spill which may result in a compromise between intensities and duty cycle. The primary beam pulses of the Booster cycle not involved in the fragment production may be directly used at the Booster energy range for different purposes (nuclear physics, applied research, cancer therapy, ...).

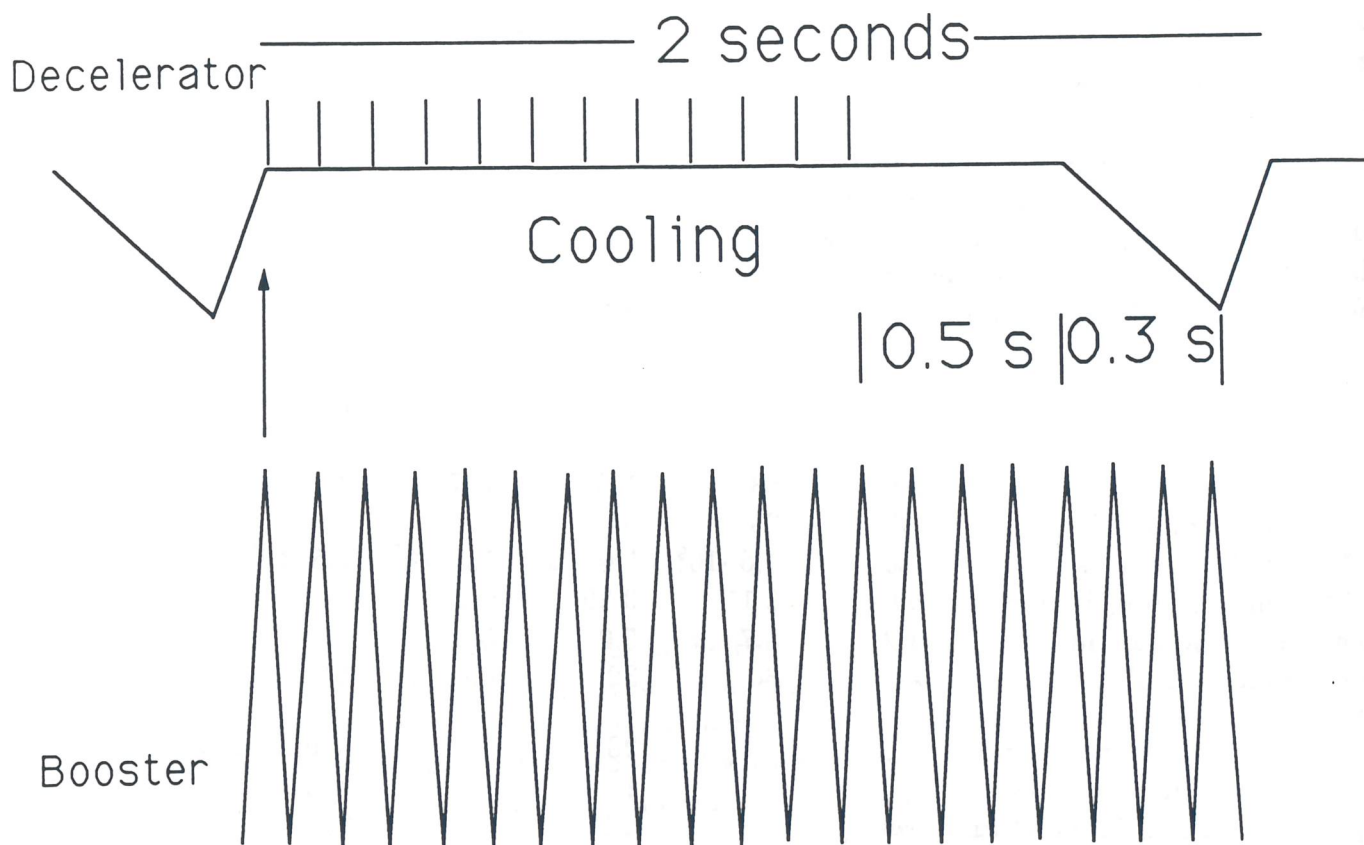


Figure 1.4.1: Magnetic cycle of the ADRIA Complex.

## 2

# Injectors

### 2.1 Heavy Ion Injector

Heavy ions are injected into the ADRIA Booster using the facilities at LNL: the existing XTU Tandem and the ALPI superconducting post-accelerator now under construction [1a]. The ALPI post-accelerator will be able to accelerate very heavy ion beams to an energy equivalent to what would be delivered by a 40 MV electrostatic accelerator. The layout of the injector is shown in Figure 2.1.1.

The XTU Tandem-ALPI combination is able to provide the short high current pulses of heavy ions required to fill the ADRIA Booster accelerator. Moreover the combination provides very good quality beams with small transverse emittances and momentum spread, which allows the injection of several beam turns into the reasonably small magnet aperture of the Booster.

It is also possible with this scheme to obtain beams with a wide range of mass numbers at sufficiently high charge states by using stripping targets at proper locations. The most demanding species to accelerate are of course the heaviest ones. In the following text we take Gold to be the reference case; however, other ions have also been considered (see Table 2.1.1). Notice that ions lighter than Sulfur can be accelerated using the same cycle as the one of Sulfur itself.

#### 2.1.1 The XTU Tandem

The XTU Tandem is an electrostatic accelerator of very reliable and established performance [2]; it is fed by a sputter source capable of delivering ions of any desired species (except the noble gases) with an initial charge state of -1. The negative ion source is currently operated in continuous mode, which is the conventional mode of operation of this device for most atomic and nuclear physics applications; but it can also be pulsed over short periods of time and at relatively high repetition rate. This mode of operation has been demonstrated first at Brookhaven National Laboratory [3]; it is most useful when high peak currents are required for injection into a circular accelerator. For ADRIA, the required repetition rate for the source is 10 Hz, to match the repetition rate of the Booster, with a pulse duration of 360  $\mu$ s to correspond to 40-turn injection, assuming Gold ions (see Section 3.2.1).

In the first section of the Tandem, the beam is accelerated from the source towards the high-voltage terminal, which in the case of the XTU Tandem is at 16 MV. Since the

charge state of the ions during this step is -1, the total kinetic energy at the terminal is just 16 MeV. At the terminal the beam hits the first stripping target where the ions are stripped of some of their electrons and acquire a charge state  $Q_T$ . In the second section of the Tandem, the beam is accelerated from the positive high-voltage terminal to ground potential at the downstream end of the accelerating column. The total kinetic energy gained in this section is  $16 \cdot Q_T$  MeV, and the total kinetic energy from the entire Tandem  $16 \cdot (Q_T + 1)$  MeV.

The bunching operation for injection into the ALPI post-accelerator is performed with two main devices. The first, a double-drift buncher with a basic frequency of 5 MHz, is located between the high voltage platform housing the sputter source and the entrance to the Tandem; the second device (a time compressor) is located in front of the ALPI post-accelerator and actually consists of two superconducting Quarter Wave Resonators with frequencies of 80 and 160 MHz. The choice of 5 MHz for the frequency of the double-drift buncher corresponds to a  $360 \mu s$  pulse made up of a train of 1800 bunches, spaced by 200 ns, for the case of a Gold ion beam.

### 2.1.2 The ECR and RFQ System

An alternate and complementary injector to ALPI is under development at the LNL: it consists of an ECR ion source and a buncher located on a high voltage platform, a transport line and a superconducting RFQ.

The 14.4 GHz ECR ion source Alice went into first operation at the end of 1991, is already capable of producing significant beam currents of highly charged ion species, and its performances are being optimized at present [4,5]. The magnetic field bottle is made out of two normal conducting solenoids, each fed by a 640 A/29 V power supply. A removable small iron core provides a flexible first stage. A NdFeB hexapole grants efficient radial confinement.

Since the discharge is produced only with the microwaves and without any cathodes, no material is consumed in an ECR source but the one providing the ion species to be extracted and accelerated: this makes an ECR one of the most reliable sources, which can be operated continuously for weeks without any interruptions. Well known techniques for the production of highly charged particles also from solid materials (high and low temperature ovens, movable rod grazing the resonant surface in the plasma chamber, etc.) are now under development at the LNL [6].

The high current positive injector is schematically shown in Figure 2.1.1 within the ALPI hall. A high voltage platform [7], designed for more than 350 kV voltage, will house the ECR source, an Einzel lens as a focusing element just after it, the analysis dipole and a 5 MHz buncher in the focus of the latter (about 1.1 m downstreams).

Good stability is required for the High Voltage platform, since an energy spread of about  $10^{-4}$  is required for a small longitudinal emittance at the RFQ. According to the  $Q/A$  value of the extracted ion, the platform voltage will be varied, so as to match  $\beta_{in} \approx 0.01$ . With a typical beam energy after the HV platform, of 10 MeV, the longitudinal emittance is  $\epsilon_L = 20$  keV ns. In this case the 5 MHz buncher will compress the 20 ns bunches to about 1 ns ( $\Delta\phi = 18^\circ$ ) at the entrance of the RFQ. Required normalized transverse emittances as low as  $\gamma\beta\epsilon \approx 0.1 \pi mmrad$  are a well established performance goal for ECR ion sources [8,9].

After being bunched and preaccelerated by the platform potential, the beam is bent

twice by  $90^\circ$  dipoles onto the focal plane of the linac and, by means of proper quadrupole triplets, is focused at the entrance of the RFQ. The latter is meant to be superconducting, both for low power consumption (CW structure,  $f=50$  MHz; 100% duty cycle) and for physical considerations: it can be properly short to fit into a reasonably small cryostat since the buncher section can be avoided (bunching is made on the platform upstreams). The design philosophy should follow the one adopted for the prototype which was developed at Stony Brook [10], finished and proved successful in 1991. It has a 4-rod structure with six tanks. At the exit a  $\beta_{out} = 0.05$  well matches the low- $\beta$  cavity injection parameter of the Linac ALPI, while normalized transverse emittances should be not more than twice the input ones, and the longitudinal one should remain nearly unaltered.

The ion currents extracted from the ECR source, usually in DC mode, will be in the range of 10 to 100  $\mu A$  (1 to 10  $p - \mu A$ ) [11] for the high charge state of the ion species of interest. If used as the first stage of an injector into a synchrotron, as it might be in the ADRIA case, the output current of the higher charge states can be increased by nearly one order of magnitude [12] if the ECR is operated in the so called "afterglow mode" [13], i.e. pulsing the RF system of the source with a repetition rate of 10 Hz. For example,  $Au^{25+}$  which has a suitable Q/A ratio for injection into the RFQ, is expected to give a yield of tens of  $p - \mu A$  in pulsed mode.

The naturally high charge state production bypasses the stripping process associated with acceleration in the Tandem; nevertheless a stripping step is still required in ALPI when  $\beta < 0.08$  to increase the charge state to +51. At the moment the overall performance in intensity and beam dimensions of the ECR-RFQ system does not seem to be competitive to those of the Tandem when, in combination with the ALPI, they are used as injector of ADRIA. Nevertheless, the ECR source technology is expanding and improving at fast rate and in a not too far future may become more competitive.

### 2.1.3 The ALPI Post-accelerator

The ALPI post-accelerator is a series of superconducting Quarter Wave Resonators [14a,14b,14c] made of OFHC (Oxygen-Free High-Conductivity) copper electroplated with lead. The transverse focusing and the bending are done with normally conducting techniques. To accelerate heavy ions over a wide range of velocities, a broad Transit Time Factor curve is required; this is obtained with a two-gap cavity [1a,1b]. Each cavity is independently phased to enable the acceleration of ion species with very different velocities. Furthermore, the large  $\beta$  variation of a single ion species along the machine requires the use of different sections of the post-accelerator for different  $\beta$  ranges. This is achieved by means of three sections: a low- $\beta$  section with 24 cavities ( $\beta_{opt}=0.055$ ) operating at 80 MHz; a medium- $\beta$  section with 48 cavities ( $\beta_{opt}=0.11$ ) at 160 MHz; and a high- $\beta$  section ( $\beta_{opt}=0.15$ ), of 21 cavities also operating at 160 MHz. The mean accelerating field is of the order of 3.0 MV/m with a quality factor of about  $10^8$  and a total dissipated power around 6 W per cavity. The kinetic energy gain per cavity is around 0.45 MeV per charge unit and the equivalent total accelerating voltage is about 40 MV. General parameters are summarized in Table 2.1.1.

For the case of Gold ions, the beam is injected into the ALPI post-accelerator with charge state +13, which is produced at the stripping target in the XTU tandem; acceleration then continues through a section equivalent to a total of 36 MV, the Gold ions acquiring a specific kinetic energy of about 3.5 MeV/u; this corresponds to  $\beta_s = 0.0864$ , high enough for

a second, highly efficient stripping stage. The location of the second stripping target is shown by a dot in Figure 2.1.2. The Gold ions then acquire a new charge state  $Q_F = +51$ . The ions then traverse the remaining 4 MV section where their specific kinetic energy increases to a total of 4.58 MeV/u, which corresponds to  $\beta_F = 0.0988$ . Table 2.1.2 summarizes the expected beam characteristics at the end of acceleration in ALPI for several ion species. Light ions like Sulphur will already be completely stripped by the target housed in ALPI. The beam transverse emittance and momentum spread depends mostly on multiple scattering effects in the stripping targets. A final rms emittance of  $1 \pi$  mm-mrad in both horizontal and vertical planes is assumed here. For design purposes, the stripping target is taken to be at the same position in the ALPI post-accelerator for all ion species; the location chosen corresponds to a net voltage of 36 MV. Of course during design optimization, and also during machine operation, the stripping location can be easily changed from species to species. Carbon foils are used for stripping targets, both in the XTU tandem and the ALPI post-accelerator, with a thickness of a few tens of  $\mu\text{g}/\text{cm}^2$  optimized to yield the charge state which corresponds to the largest efficiency estimated with conventional formulae [15]; some corrections are required [16], but under the present conditions they are small and are therefore ignored here.

Finally, each beam pulse is made of a train of micro-bunches which, during acceleration in the 160 MHz section of ALPI, occupy 1 in 32 rf buckets. The required pulse lengths for other ion species are also given in Table 2.1.2; they are estimated assuming 40-turn injection into the ADRIA Booster. The Tandem (or ECR + RFQ)-ALPI combination operates at a repetition rate of 10 Hz for all ion species, matching the repetition rate of the ADRIA Booster.

## 2.2 The Transfer Line (ITL) between ALPI and the Booster

The extraction point from the ALPI post-accelerator and the injection point of the ADRIA rings are separated by a 50 m long transport line consisting of focusing quadrupoles, a few bending magnets and one debuncher cavity. Because the elevations of the beam in ALPI and in the ADRIA Booster differ of 1.5 metres, an achromatic vertical bending is required. Horizontal bending is not required because the extraction line from ALPI is tangent to the straight section of the Booster.

The transport line is designed to provide matching of the lattice functions at both upstream and downstream ends, avoiding unnecessary dilution of the beam emittances. The design of the line takes advantage of the concept of standard FODO cells with about  $90^\circ$  phase advance per cell, with special matching doublets or triplets at the ends. As far as possible, quadrupoles are all of the same length, cross-section and strength, and are similar to those employed in the ALPI project.

**Table 2.1.1 Acceleration in the ALPI Complex. General Parameters**

XTU Tandem Terminal Voltage	16	MV
ALPI Post-Accelerator		
Average Accelerating Field	3	MV/m
Synchronous Phase	-20	deg
Maximum Magnetic Rigidity	3.3	Tm
Length	~80	m
Number of Cavities		
Low Beta Section $\beta = 0.055$	24	
Medium Beta Section $\beta = 0.09$	48	
High Beta Section $\beta = 0.15$	21	
Length of Modules		
'Short' Modules	4.06	m
'Long' Modules	4.30	m
Number of Cavities per Module		
Low- & Medium- $\beta$ Sections	8	
High- $\beta$ Section	6	
Number of Cryostats per Module	2	
Resonant Frequency		
Low- $\beta$ Section	80	MHz
Medium- & High- $\beta$ Sections	160	MHz

**Table 2.1.2 Beam Parameters of the ALPI Post-accelerator.**

Ion Species	S	Cu	I	Au	U
Atomic Number	16	29	53	79	92
Mass Number	32	63	127	197	238
Charge State $Q_F$	16	27	40	51	54
Injection En. (MeV/u)	5.0	3.05	1.64	1.14	0.94
Extraction En. (MeV/u)	16.40	10.39	6.11	4.58	3.86
$\beta_F$	0.1853	0.1483	0.1140	0.0988	0.0908
Pulse length ( $\mu$ s)	192	240	312	360	392
Energy Spread			$10^{-4}$		
Emittance (rms)			$1 \pi$ mm-mrad		

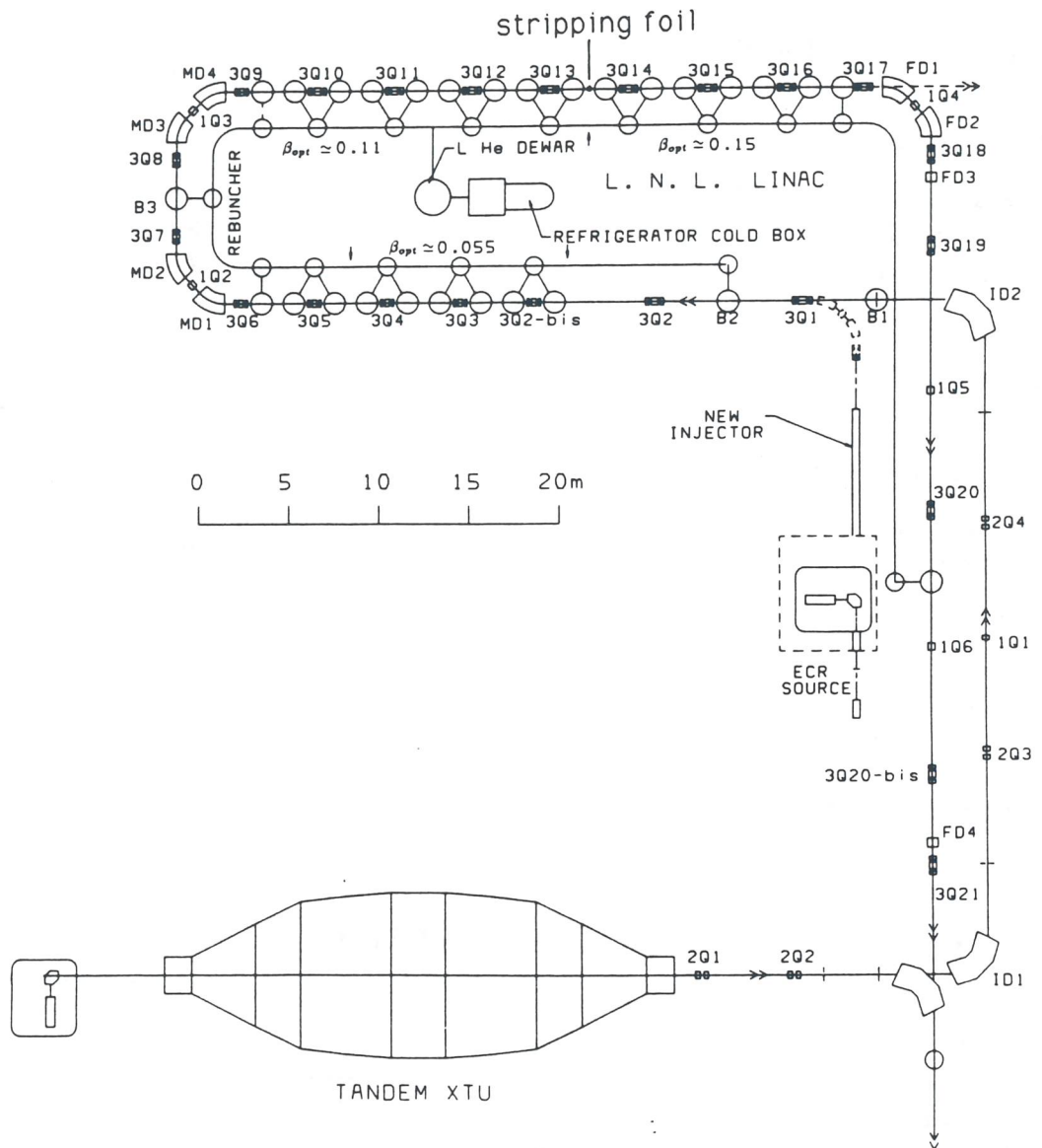


Figure 2.1.2: Layout of the ALPI Post-accelerator.

## References

- [1a] G. Fortuna et al., "The ALPI project at the Laboratori Nazionali di Legnaro", Nucl. Instr. and Meth. A-287 (1990)253-256.
- [1b] A. M. Porcellato et al., Proceedings of the twenty-fourth Symposium of North Eastern Accelerator Personnel, Kansas State University, October 1990, pag. 259-277.
- [2] R. A. Ricci and C. Signorini, Nucl. Instr. and Meth., 184 (1981) 35.
- [3] P. Thieberger et al., Nucl. Instr. and Meth. A-268 (1988) 513-521.
- [4] M. Cavenago and G. Bisoffi, Nucl. Instr. and Meth. A-301 (1991), 9-18 (1988) 513-521.
- [5] M. Cavenago, Proceedings of the 3rd EPAC Conference (to be published).
- [6] T. Nakagawa et al., Proceedings of the 10th International Workshop on Ion Sources, ORNL-Conf. 9011136, 163.
- [7] V. Stolbunov et al., "The Project of a High Voltage Platform", LNL-INFN (Rep) 052/91.
- [8] R. Pardo, Nucl. Instr. and Meth. B40/41 (1989), 1014-1019.
- [9] Y. Jongen and C. Lyneis, "The Physics and Technology of Ion Sources", ed. Ian G. Brown, J. Wiley and Sons, 207.
- [10] I. Ben-Zvi, P. Paul, A. Lombardi, PA.
- [11] R. Geller, Review of Scientific Instruments **61** (1990), 659.
- [12] P. Sortais, Proceedings of the 6th International Conference on Ion Sources, Bensheim, October 1991, to be published in Rev. of Scient. Instrum., April 1992.
- [13] G. Melin et al., J. de Physique C1, 50, 1989.
- [14a] I. Ben-Zvi and J. M. Brennan, Nucl. Instr. and Meth. 36 (1976) 421.
- [14b] P. Boccaccio, LNL Annual Report 1986 LNL-INFN(REP) 002/87.
- [14c] E. Chiaveri, B. V. Elkonin, A. Facco and J. S. Sokolowski, Proceedings of the 2nd European Particle Accelerator Conf., Nice, June 1990, pag. 1103-1105.
- [15] K. Shima, T. Ishihara and T. Mikumo, Nucl. Instr. and Meth. 200(1982) 605.
- [16] M. A. McMahan, R.F. Lebed and B. Feinberg, Proc. of the 1989 IEEE Part. Acc. Conference, Chicago, ILL. Vol.1 (1989) pag. 536.

# 3

## Booster Ring

### 3.1 Lattice and General Layout

The overall size of the ring has been determined by general considerations such as the highest specific kinetic energy of the heaviest ion to be accelerated, compatibility with the heavy ion injector, and the available space on site. The maximum specific energy has been fixed at 1 GeV/u for Gold ions, corresponding to a magnetic rigidity of 22.25 Tm.

The ALPI injector provides 200 ns bunch spacing, and the rf matching requires the Booster circumference to be a multiple of the incoming bunch spacing; this multiple has been chosen to be 45 for Gold ions; this, together with the output velocity ( $\beta=0.098834$ ), gives a total length of 266.6667 m, consistent with the area available on site.

The shape and symmetry of the ring has been determined by the need for many straight sections to accommodate devices for beam handling, namely injection and extraction systems, and acceleration cavities. This need for many straight sections, combined with the high periodicity required to avoid crossing systematic betatron resonances, suggests the choice of a fourfold symmetry (Figure 3.1.1), which also allows a reasonably high dipole magnet packing factor. Given the periodicity of the lattice it is important to fix the choice of the betatron tunes to stay clear of the following major systematic resonances:

$$\begin{aligned}\nu_h &= i, & \nu_v &= j \\ 2\nu_h &= k, & 2\nu_v &= l \\ \nu_h + \nu_v &= m, & \nu_h - \nu_v &= n\end{aligned}$$

(with  $i, j, k, l, m$  and  $n$  natural integers).

While several sets of values can satisfy these requirements, general considerations of technical feasibility and machine operation make the choice of  $\nu_h=5.8$  and  $\nu_v=3.8$  the preferred one [1]. This solution allows a betatron phase advance per cell of about  $90^\circ$  in the horizontal plane and  $60^\circ$  in the vertical plane. This can be considered good from the point of view of chromatic and aberration effects, and operational aspects such as the positioning of diagnostics devices. The resulting cell half-length is over five metres, which can accommodate a dipole magnet about 3.5 m long.

In the high intensity mode, one can expect a considerable tune depression from space charge, which shifts the tune values closer to half-integral resonances; for instance in the horizontal plane from 5.8 down to 5.6. This is believed to be better than the situation with the unperturbed tune just below a half-integral value (such as 5.3 or 3.3) because in that case the shift would bring the tune values closer to integral resonances.

Larger values of tunes than those given above would require either a larger betatron phase advance per cell, endangering beam stability, or a shorter cell length, reducing considerably the packing factor and the attainable magnetic rigidity. On the other hand, lower tune values are not acceptable because they would lead to large beam envelopes which require unreasonably large magnet apertures.

To ensure good stability of the betatron motion, a separated function FODO focussing structure has been chosen for the basic cell. The choice of the FODO cell also gives very good chromatic properties, and in principle a higher momentum acceptance.

Each superperiod, which is mirror-symmetric about its mid point, consists of an arc and two half straight sections; four bending cells make up the arc, while the two half straight sections consist of a basic cell without the bending dipoles.

The total number of cells is therefore fixed at 24, 8 of which are without dipole magnets, and the resulting length of the basic cell is 11.11 m. The maximum magnetic field (1.26 T) and beam rigidity accepted, together with the total number of bending dipoles (32), set the length of the dipole magnets at 3.46 m.

The dipoles are sector magnets with zero entrance and exit angles; because of the large sagitta ( $\sim 8.5$  cm), they have to be curved. Only two types are used: 0.6 m long focussing (QF) and 0.5 m long defocussing (QD), in the horizontal plane. Their lengths are different so that the required strengths, which are different in the two types, can be produced by the same excitation current. The drift spaces between dipoles and quadrupoles are 0.7728 m long.

This configuration allows a 'transparent' arc with a betatron phase advance of almost  $360^\circ$  in the horizontal plane, which also makes the dispersion function vanish at the ends; the dispersion remains zero along the full length of the long straight section.

The overall magnet layout of the Booster is shown in Figure 3.1.1 and a summary of the lattice and FODO cell parameters is given in Tables 3.1.1 and 3.1.2. Lattice and dispersion functions are shown in Figure 3.1.2 for one fourth of the machine. It can be seen that while the periodicity of the  $\beta$  functions exactly matches the cell periodicity, the dispersion function follows the superperiodicity of the structure. Table 3.1.1 also shows that the transition  $\gamma$  is high enough to have the machine working always well above the transition energy.

Both horizontal and vertical envelopes are shown in Figure 3.1.3; they correspond to a full emittance of  $140 \pi \text{ mm-mrad}$  and a momentum spread of  $\pm 0.5\%$  combined quadratically. It is seen that the largest vertical height and horizontal width are about 100 mm.

The positioning of the magnets in the tunnel requires special care. The following alignment rms errors are considered to be within the present state of the art: 0.3 mm for quadrupole lateral displacement and 0.3 mrad for dipole axial rotation. In addition, an integrated dipole field error of  $3 \times 10^{-4}$  rms can be expected. This causes an uncorrected closed orbit distortion with an expected value of about 5 mm rms in the quadrupoles, ensuring that the closed orbit is within the available aperture at the start of operations. The initial use of a small-size beam can then allow detection and correction of the closed orbit distortion. For this purpose, two families of beam position monitors and steering magnets are located next to all QF and QD quadrupoles.

Similarly, quadrupoles have a maximum axial rotation error of 0.3 mrad rms, set by the effects of the betatron coupling, and a maximum integrated gradient error of  $10^{-3}$ , which could cause a half-integral stop-band width of 0.004 rms.

**Table 3.1.1: Lattice Parameters of the Booster.**

Ring Length	266.6667	m
Lattice Periodicity	4	
Maximum Magnetic Rigidity	22.25	Tm
Magnetic Bending Radius	17.6216	m
Total Number of Cells	24	
Number of Cells per Arc	4	
Phase Advance per Cell		
Horizontal	90°	
Vertical	60°	
Transition $\gamma$	4.6	
Betatron Tunes		
$\nu_h$	5.8	
$\nu_v$	3.8	
Natural Chromaticity		
$\xi_h$	-5.45305	
$\xi_v$	-4.89149	
$\beta_H$ , max	16.0 m	
$\beta_V$ , max	21.6 m	
Dispersion, max	4.95 m	

**Table 3.1.2: Parameters of the FODO Cells.**

Cell Length	11.1111	m
Dipoles:		
Dipole Length	3.4600	m
Bending Angle	11.25°	
Bending Radius	17.6216	m
Sagitta	8.48	cm
Vertical Gap	10	cm
Drifts:		
Drift Length	0.7728	m
Quadrupoles:		
QF Length	0.6000	m
Gradient	8.77	T/m
QD Length	0.5000	m
Gradient	8.77	T/m
Bore Radius	7.0	cm



### 3.2 Inj-

The  
ures 3.1.  
in Figure  
each other  
is a n-  
sion, w  
good med  
cross-sect  
given by

Lattice functions of the ADRIA Booster (one fourth) -  $Q_x=5.8$ ,  $Q_y=3.8$   
Cray - UNICOS version 8.3/7

09/07/91 16:24:22

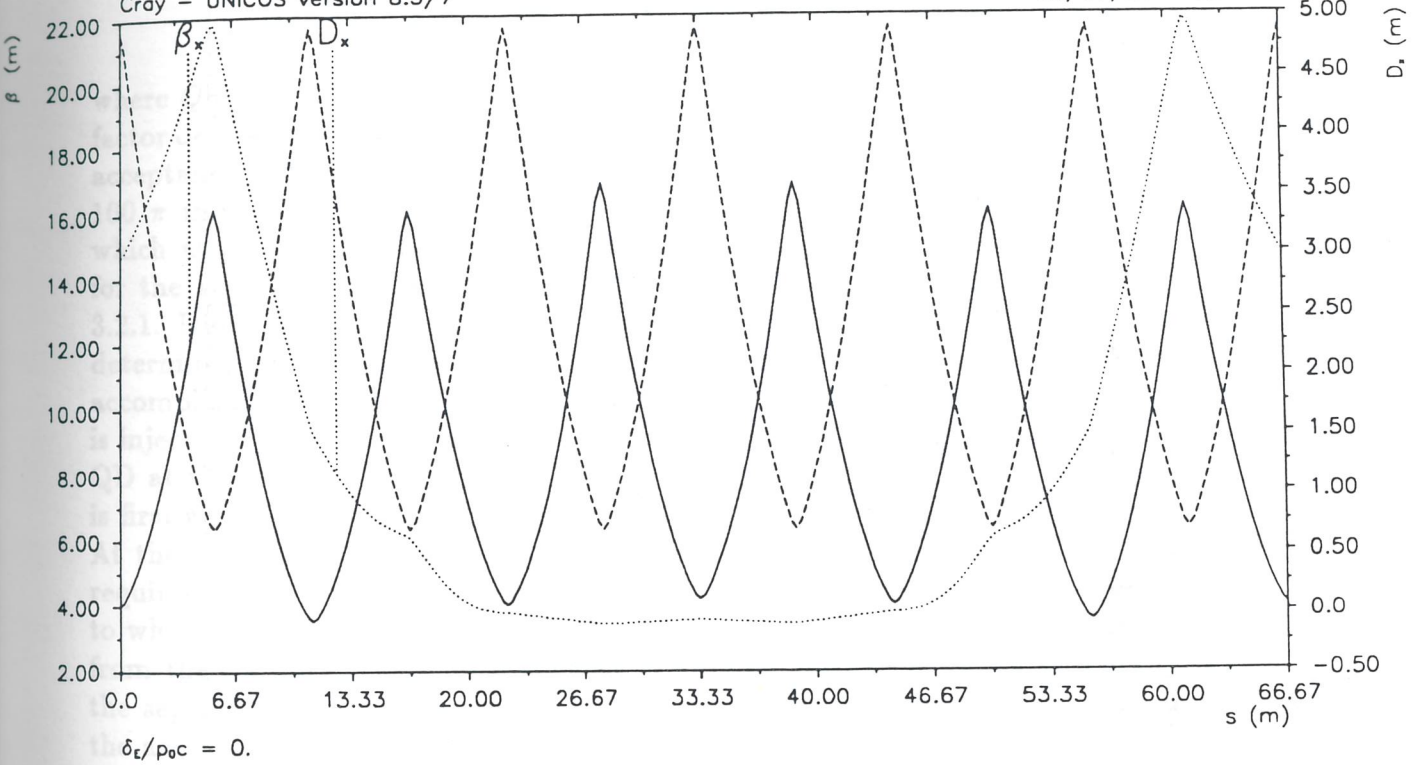


Figure 3.1.2. Lattice functions of the Booster (one fourth).

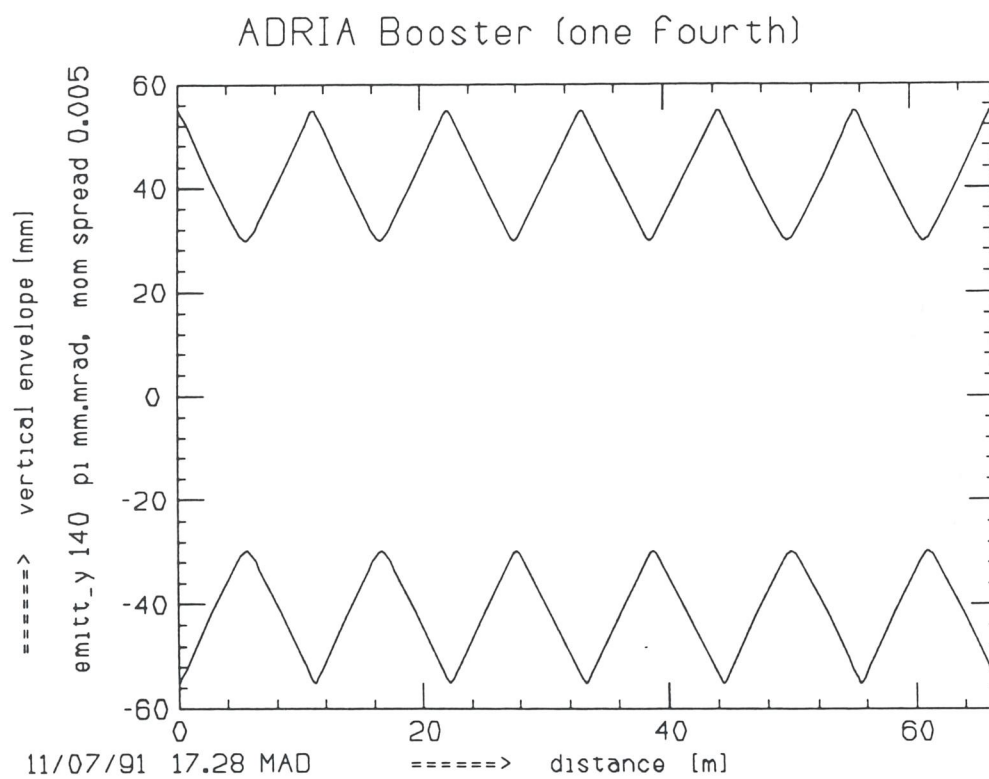
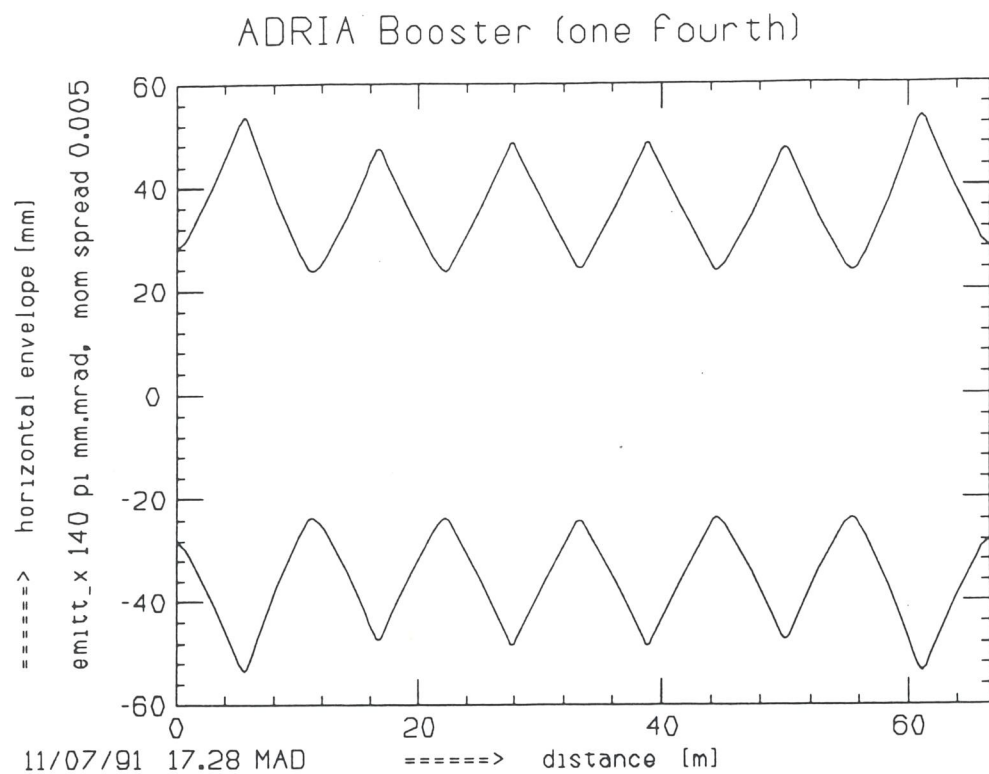


Figure 3.1.3. Beam envelopes for the Booster (one fourth).

## 3.2 Injection

The injection of heavy ions takes place in a long straight section, as shown in Figures 1.1.1 and 1.1.2. The components for injection and extraction are shown in more details in Figure 3.7.1. Multi-turn injection is accomplished by placing consecutive turns next to each other in betatron phase space. After  $n$  turns have been injected the beam emittance is  $\epsilon = n\epsilon_0/\eta_n$ , where  $\epsilon_0$  is the emittance of a single turn and  $\eta_n < 1$  is the injection efficiency, which depends on the number  $n$  of turns already injected. High efficiency requires good matching of the transfer line to the Booster, and also proper shaping of the beam cross-section. For a given total beam emittance there is a limit to the maximum intensity, given by the maximum allowable tune-depression  $\Delta\nu$  due to space-charge forces, taken here to be 0.5. The relation between  $\Delta\nu$ , the total beam emittance  $\epsilon$ , and the total number  $N$  of particles is [2,3,4]

$$\Delta\nu = \frac{Nr_p Q^2}{2\beta^2 \gamma^3 B A \epsilon} \quad (3.2.1)$$

where  $Q$  is the charge state,  $A$  the mass number,  $r_p = 1.535 \times 10^{-18}$  m and  $B$  the bunching factor defined as the ratio of the average beam current to the peak current. Since the physical acceptance of the Booster is  $140 \pi$  mm-mrad, a safe value for the total beam emittance is  $100 \pi$  mm-mrad. Thus, for the case of Gold ( $Q=51$ ,  $A=197$ ) we derive  $N = 5 \times 10^{10}$ , which at the repetition rate of 10 Hz corresponds to  $5 \times 10^{11}$  ions per second. Estimates for the achievable currents with the injection scheme described above are given in Table 3.2.1. Different final currents result from the tune-depression value (here  $\Delta\nu = 0.5$ ) which determine the maximum allowable intensities. The injection of 40 turns in one plane is accomplished by using a scheme similar to that of the AGS Booster at Brookhaven [5]. Beam is injected in the horizontal plane via a Lambertson magnet located next to the quadrupole QD at the centre of the long straight section (see Figure 3.2.1). A horizontal orbit bump is first generated with steering correctors located at both ends of the long straight section. At the injection point, which is at the end of the Lambertson magnet, a narrow beam is required, i.e. a low value for  $\beta_h$ . Taking  $\beta_h = 6$  m, the beam width at injection is 8 mm, to which 3 mm for the septum thickness has to be added. The first turn is injected 11 mm from the bumped closed orbit, which is initially displaced by 29 mm. The inner side of the septum is at a distance of 33 mm from the reference closed orbit; this will not reduce the acceptance of the ring. The orbit bump is turned off at a rate fast enough to avoid for any single pulse hitting the injection septum, but also slow enough to allow the maximum number of turns to be injected. For 40 turn injection, the orbit bump magnets must be turned off in 140  $\mu$ s for very light ions, and in 360  $\mu$ s for Gold ions. The required magnet components for multi-turn injection of heavy ions are listed in Table 3.2.2.

**Table 3.2.1: Heavy Ion Beam Parameters at Injection into the Booster.**

	S	Cu	I	Au	U	
Mass Number	32	63	127	197	238	
Atomic Number	16	29	53	79	92	
Charge State	16	27	40	51	54	
$\beta$	0.1853	0.1483	0.1140	0.0988	0.0908	
Kinetic Energy	16.4	10.4	6.1	4.6	3.9	MeV/u
Orbit Period	4.8	6.0	7.8	9.0	9.8	$\mu$ s
Harmonic No.	24	30	39	45	49	
Beam Intensity	2.0	1.3	0.7	0.5	0.5	$10^{12}$ ions/s
Normal. Emittance	22.6	18.0	13.8	11.9	10.9	$\pi$ mm mrad
Bucket Area	8.6	5.5	3.5	2.6	2.4	meV/u-s
Space-Charge $\Delta\nu$			0.5			

**Table 3.2.2: Magnetic Elements Specifications for Heavy Ion Injection.**

Initial Orbit Bump	29	mm
Bump Fall-off Period	70-180	$\mu$ s
Number of Injected Turns	$\geq 20$	
Lambertson Magnet:		
Length	1	m
Field	0.2	T
Aperture (H $\times$ V)	2 $\times$ 4	cm <sup>2</sup>
Septum Thickness	3	mm

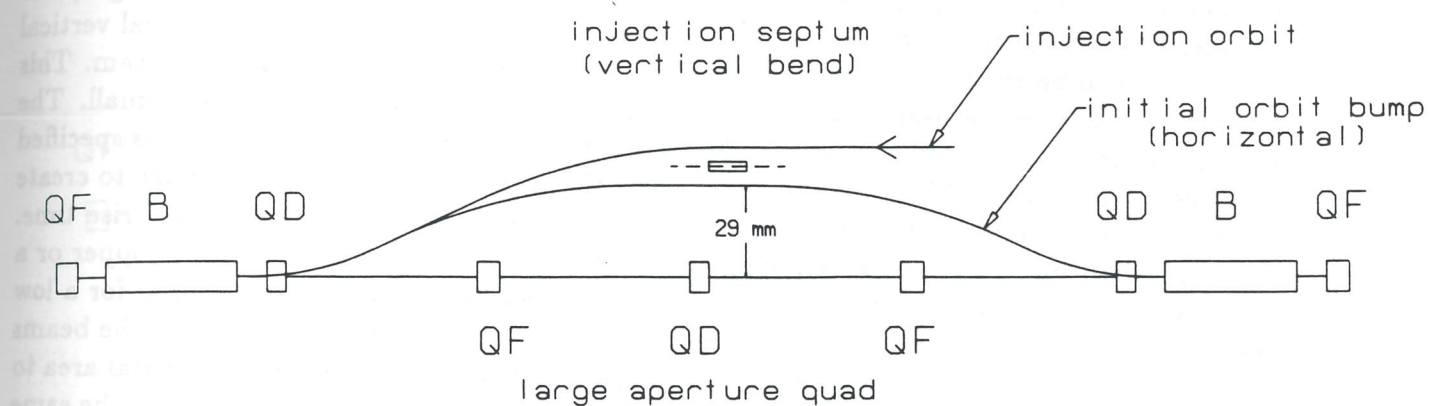


Figure 3.2.1. Schematic Layout of the Injection System for Heavy Ions.

### 3.3 Extraction

The heavy ion beams are extracted from the Booster in single-turn mode. If slow-spill extraction is required, this can be accomplished in the Decelerator, after transferring and debunching. Extraction takes place in the straight section adjacent the injection straight, as shown in Figure 3.7.1. It starts (see Figure 3.3.1) with a fast kicker magnet, located upstream of the straight section, which displaces the beam vertically by 60 mm at the entrance to a Lambertson magnet that moves the beam horizontally. The septum of the Lambertson magnet is 10 mm thick and is located 32 mm away from the central orbit in order not to restrict the required physical acceptance. The deviation generated by the kicker is large enough to extract the full beam at all energies. The main parameters of the magnetic extraction components are given in Table 3.3.1. To reduce the required kicker strength, it is proposed to use the steering magnets in the long extraction straight to create a local vertical bump that can be turned on slowly, after which the kicker is fired to extract the beam. This technique will be more useful at high energies, where the beam dimensions are small. The rise time of the kicker magnet is about 150 ns, with dimensions and field strength as specified in Table 3.2.2. Since the bunch spacing at extraction is about 20 ns, it is necessary to create before injection a gap in the beam of about 7 empty buckets to match the kicker rise time. The undesired bunches can be removed at the exit of the ALPI with a beam chopper or a modulated deflector which can send them to other areas where they can be used for a low energy experimental program. After extraction, by means of a switching magnet, the beams can be directed on a target to generate exotic fragments or sent in the experimental area to be used for nuclear physics ( see Figure 3.3.1). Beam abort can be accomplished in the same way, through the same extraction channel: a pulsed magnet when turned on will direct the beam to the required underground area for dumping in a dedicated target.

**Table 3.3.1: Magnetic Element Specifications for the Extraction Channel.**

Lambertson Magnet		
(Horizontal Bend)		
Length	3.5	m
Field	1.0	T
Aperture (H×V)	5×5	cm <sup>2</sup>
Kicker Magnet		
(Vertical Bend)		
Length	3.5	m
Field	0.04	T
Aperture (H×V)	10×15	cm <sup>2</sup>
Rise Time	150	ns

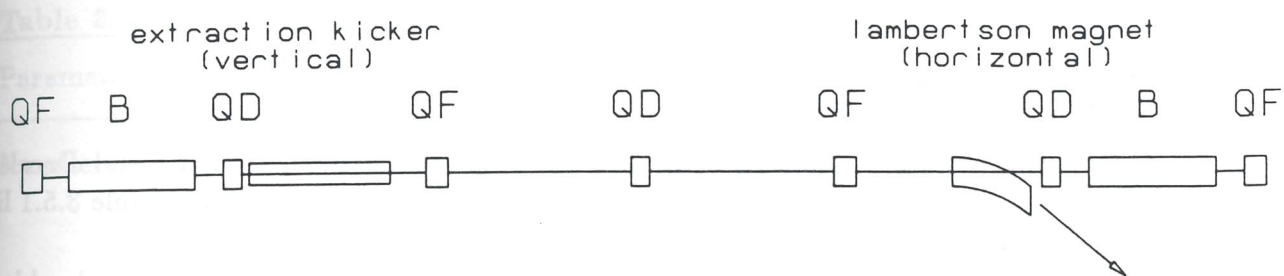


Figure 3.3.1. Extraction Line from the Booster.

## 3.5 The Magnet System

The Booster lattice consists of 24 cells with 24 horizontally focussing quadrupoles (QF), 24 horizontally defocussing quadrupoles (QD) and 32 bending dipoles (2 bending dipoles for each of the 16 cells in the arcs). The beam envelopes in Figure 3.1.3 shows a maximum beam dimension of 100 mm in the dipoles, and imply a dipole vertical aperture of 100 mm. The magnetic length of the dipole magnet is 3.46 m and the bending angle per magnet is  $11.25^\circ$  (0.1963 rads). The radius of curvature is  $\rho=17.6216$  m, and the designed maximum bending field is  $B_{max}=1.26$  T. The bending magnets are of sector type and are curved to accommodate the sagitta of 84.8 mm. As a consequence the vacuum chamber and the coils are also curved. The QF and QD focussing elements have a magnetic length of 0.6 m and 0.5 m respectively, their bore diameter is 140 mm and the maximum design field gradient is  $G=\pm 8.77$  T/m with a field at the pole tip of 0.62 T. The high repetition rate of the machine requires a high dipole field rate of change  $\dot{B}=38$  T/s which, to avoid eddy current effects in the iron core, implies thin laminations for all the magnetic elements in the ring.

### 3.5.1 Dipole Design.

The H-type bending magnet design has been chosen for both Booster and Decelerator [1]. The cross-section of a dipole magnet is shown in Figure 3.5.1, while Table 3.5.1 lists the fundamental parameters.

To achieve the correct curvature, lamination foils are packed in 14 rectangular blocks 250 mm long (except for the two external ones of a shorter length to be determined after a more detailed design) which, to obtain the overall bending angle of  $11.25^\circ$ , are assembled with an angle of  $0.9375^\circ$  between each other. The blocks are kept together by straps welded on the top and bottom edges and by two stainless steel end plates. The straps will not shunt the eddy currents because of their small size and their position in a low field region. Each dipole weights 15 tons. The laminations, 0.35 mm thick, are made of iron characterized by a low remanent field in order to obtain high field quality at low excitation, and with good saturation properties. They are stacked randomly to minimize the effect of magnetic and construction imperfections. The coils are arranged in four pancakes, two around the upper pole and two around the lower one, with 5 turns each for a total of 20 per magnet. Each conductor has a rectangular cross-section of  $18.0 \times 80.0$  mm<sup>2</sup>, each of 10 subconductors  $8.0 \times 15.0$  mm<sup>2</sup> with a central cooling hole 3.5 mm diameter, carrying a maximum current density of 4.61 A/mm<sup>2</sup>; the mean density, which sets the Joule losses, is 2.9 A/mm<sup>2</sup> (see Figure 3.5.1). The inductance of the dipole is 5.50 mH and the corresponding maximum peak stored energy is  $\frac{1}{2}LI^2=71$  kJ. The ohmic resistance is 2.9 m $\Omega$  per dipole. The current range is between  $I_{min}=287$  A and  $I_{max}=5086$  A. The maximum current rate of change is  $\dot{I}_{max}=151.1$  kA/s. These numbers correspond to the 10 Hz operation rate. The total dissipated power in the dipole system is 1.3 MW.

### 3.5.2 Quadrupole Design

The lengths of the quadrupoles in the Booster ring are adjusted to equalize the excitation

currents in the two families as closely as possible. The QF and QD quadrupoles have 0.6 m and 0.5 m magnetic length respectively, and have a maximum design gradient of 8.77 T/m. The calculated beam envelopes (Figure 3.1.3) give a bore diameter of 140 mm which, together with the design gradients, gives an easily achieved magnetic field at the pole tip of 0.62 T. The laminations are 0.35 mm thick, as for the dipoles. The quadrupole laminations, being four-fold symmetric, are cut in four identical pieces for convenience. The proposed design has four turns per coil. The cross-section of the conductor is  $18.0 \times 52.0 \text{ mm}^2$ , formed by two subconductors with  $16.0 \times 25.0 \text{ mm}^2$  cross-section with a central cooling hole with 6.5 mm diameter. With this design the same subconductor can be used for both the quadrupole and dipole coils.

The bore aperture of 140 mm implies a maximum excitation current of 4.42 kA (QF). The total power dissipated in the quadrupole system (QF+QD) does not exceed 0.3 MW.

The quadrupole parameters are given in Tables 3.5.1. The cross-section of the quadrupole magnets is shown in Figure 3.5.2.

**Table 3.5.1: List of parameters for the Booster magnets.**

Parameter	Unit	Dipoles	Quad F	Quad D
Number of Magnets		32	24	24
		sector magnet curved with sagitta 8.5 cm		
Bending Radius	m	17.62	—	—
Magnetic Length	mm	3460	600	500
Pole Tip Radius	mm	—	70	70
Pulse rep.Frequency	Hz	10	10	10
Maximum Field	T	1.26	—	—
Maximum Gradient	T/m	—	8.7	8.7
Maximum Current	A	5086.	4419.	4419.
Max Current Density	A/mm <sup>2</sup>	4.6	6.0	6.0
DC Resistance/magnet	mΩ	2.910	0.764	0.655
Inductance/magnet	mH	5.50	0.34	0.34
Dissipated Power (total)	MW	1.315	0.160	0.135
Copper Weight	ton	1.45	0.185	0.160
Iron Weight	ton	13.6	0.680	0.550

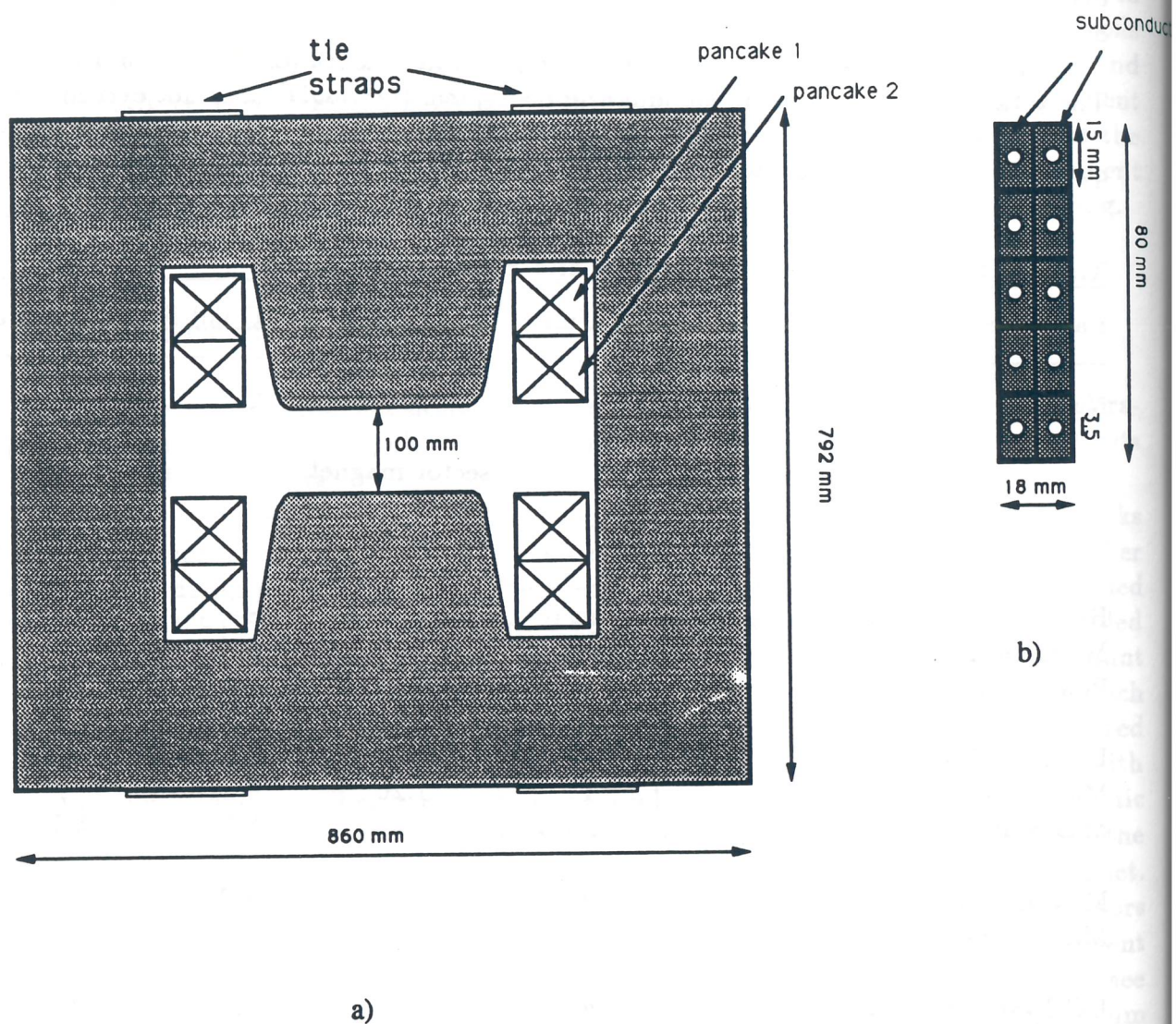
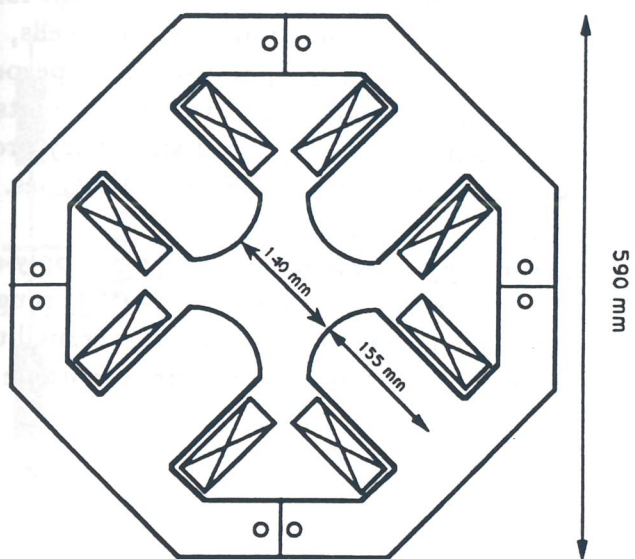
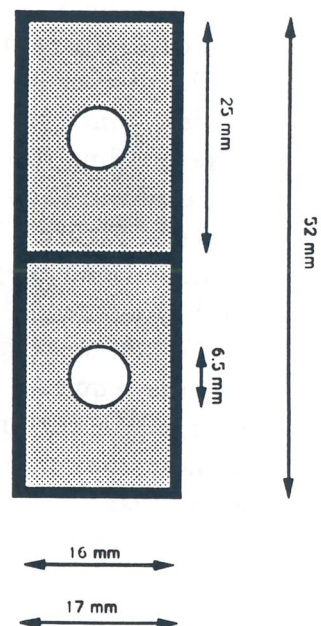


Figure 3.5.1: a) Cross-Section of the Dipole Magnets; b) Cross-Section of the Dipole Conductors



a)



b)

Figure 3.5.2: a) Cross-Sections of the Quadrupole Magnets and b) of the Quadrupole Conductor.

### 3.6 Power Supplies

The high operating frequency of 10 Hz can be easily achieved with a resonating power supply in which the inductances of the magnets are made to resonate in parallel with a capacitor bank. A programmed (digital) mode of operation is also possible, where the guiding field is ramped in steps with the aid of a low-level program; this mode of operation would allow the inclusion of flat-field period for instance for injection and slow spill extraction. The possibility of a resonating power supply is here examined. The proposed solution is to provide three power supply busses, one each for the QF and QD quadrupoles and one for the dipoles separately. Figure 3.6.1 shows the magnet and circuit arrangement for the dipoles. Since the load is large, the dipole circuit is divided into four identical cells, each corresponding to a superperiod of the magnet lattice, with all 8 dipoles of the superperiod connected to the same bus transformer. There are four virtual ground reference points. As shown in Figure 3.6.2, the quadrupoles are arranged similarly, except that since they provide a smaller load they can be included in only two cells, one each for QF and QD types. The total power required to operate the Booster magnets is 1.7 MW.

When magnets are ramped on different power supply busses, good power supply regulation is required. In order to maintain a betatron tune stable to less than 0.01 throughout the cycle, a current regulation of one part in  $10^4$  is required between the different busses. Similarly power supply ripple is of the same magnitude or less to avoid unacceptable tune oscillations.

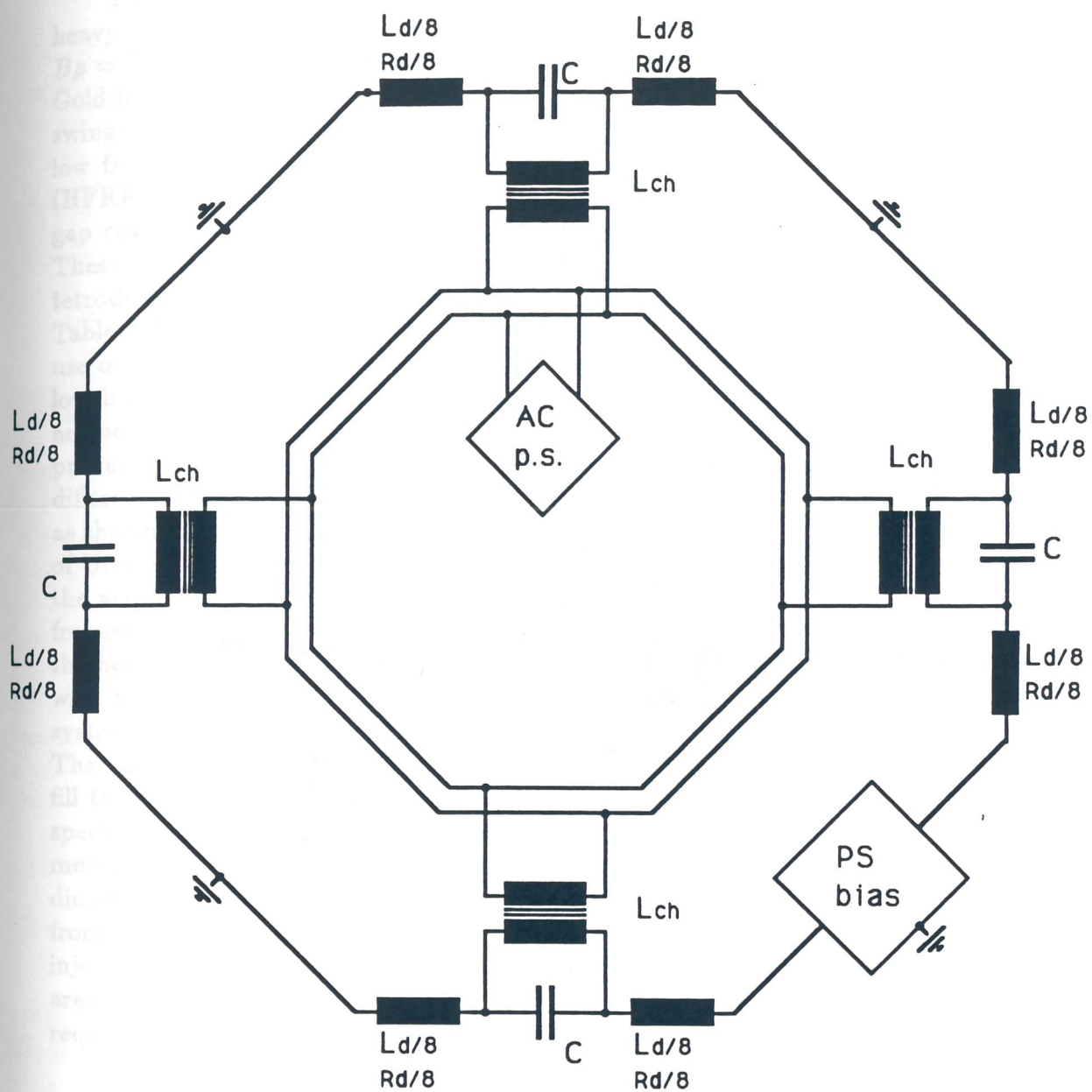


Figure 3.6.1: The Magnet and Circuit Arrangements for the Dipole Magnet.

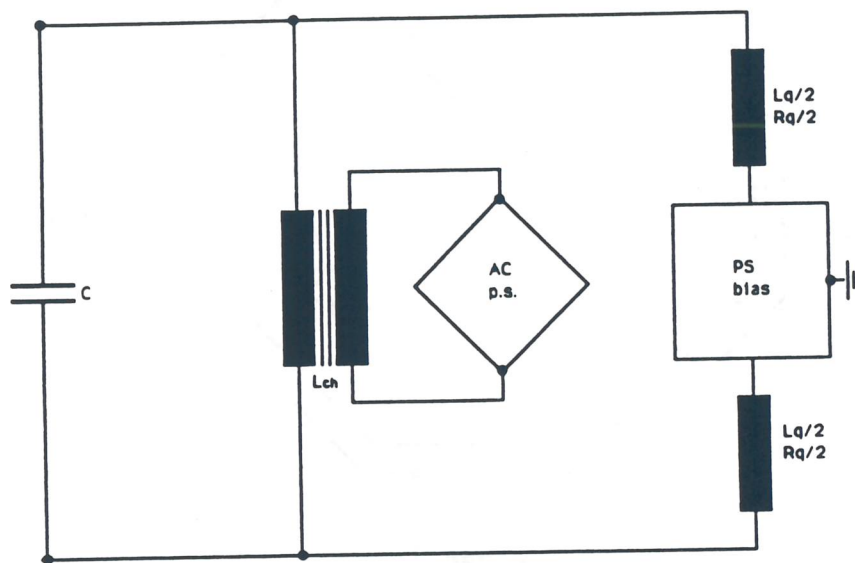


Figure 3.6.2: The Magnet and Circuit Arrangement for a Group of Quadrupole Magnets (QD or QF)

## 3.7 The rf System

The purpose of the rf system in the Booster is the acceleration of different species of heavy ions from ALPI to an energy which corresponds to the maximum magnetic rigidity  $B\rho = 22.25 \text{ Tm}$  of the ring, at a repetition rate of 10 Hz. This corresponds to 1 GeV/u for Gold ions and to 2.5 GeV/u for ions as light as Carbon. To cope with the large frequency swings required for the acceleration of heavy ions, the operating range is covered by: a low frequency system (LFRF) sweeping from 5 to 32 MHz and a high frequency system (HFRF) ranging from 30 to 47 MHz [1]. Both LFRF and HFRF systems use several double-gap cavities, tuned by applying a longitudinal biasing field to a set of Ni-Zn ferrite rings. These resonators are characterized by quality factors typically below 100, and are driven by tetrodes housed inside the cavity structure with an output power of the order of 100 kW. Table 3.7.1 summarizes the rf requirements for the acceleration of different ion species. The use of a constant harmonic number is the most convenient mode of operation, in which a low bunching factor and space-charge tune-depression are obtained, since all the buckets are occupied. The rf frequency at injection is always 5 MHz, the frequency of the ALPI prebuncher; the resulting bunch separation at injection is then 200 ns for all species. Since different ions are injected with different velocities, appropriate harmonic numbers are chosen as shown in Table 3.7.1. The largest rf swing is required for the very heavy ions: in the case of Uranium, the ratio between frequencies at extraction and at injection is 9.4, whereas for the acceleration of Sulfur a ratio of only 5.2 is required. Elements up to Copper require a frequency swing of only 5 to 32 MHz; the total gap voltage required is about 200 KV. For the heavier ions like Iodine, Gold and Uranium the frequency required is from 5 to 47 MHz, with voltages not exceeding 220 KV. This is taken into account in the choice of the two rf systems. The peak voltage depends on the acceleration rate and on the size of the rf buckets. The bucket area is determined by the painting techniques used with multi-turn injection to fill the buckets uniformly. Since the bucket length is about 200 ns, the bucket area is then specified by the bucket height, which is chosen to be at least a factor of 3 larger than the momentum spread of the bunches injected from ALPI. Table 3.7.1 gives a summary of their dimensions and the required bucket area and height. In absolute energy units, the variation from one species to another is small, as one would expect from the operation of the ALPI injector, while in specific energy units, there is a very substantial variation. The bucket area is only 0.0024 eV/u-s for Uranium and 0.086 eV/u-s for Sulfur. Most of the voltage is required for the acceleration proper and only a small fraction to generate the bucket area.

### 3.7.1 The rf Cavities

Both the LFRF and the HFRF use double-gap cavities, in which the Transit Time Factor (TTF) is a concern. The distance between the two gaps is chosen to accommodate the widest spectrum of accelerated ions.

The TTF is the parameter that indicates how efficiently particles of velocity  $\beta$  are accelerated through two gaps a distance  $L$  apart. When the two gaps are exactly  $\pi$  radians apart, the TTF is:

$$TTF = \sin \frac{\pi L}{\beta \lambda} \quad (3.7.1)$$

where  $\lambda$  is the rf wavelength. The same expression can be also written to show its dependence on the harmonic number  $h$  as:

$$TTF = \sin \frac{\pi L h}{2\pi R} \quad (3.7.2)$$

where the denominator is the circumference of the ring. It is clearly desirable to have a TTF as close as possible to unity for the widest range of species. In the case of a double-gap cavity in which the two gaps are exactly in phase (the so called 0 mode) the expression for the TTF becomes:

$$TTF = \cos \frac{\pi L h}{2\pi R} \quad (3.7.3)$$

Since the cavities are proposed to be run on a 0 mode, their TTF is ranging between 0.75 and 0.99, depending from the ion species.

### 3.7.2 The Low and High Frequency rf Systems

The low frequency rf system (LFRF) consists of cavities operating between 5 and 32 MHz [6,7] and the voltages required are of the order of 20 KV/gap. This scenario has been calculated assuming that 6 double-gap cavities are used. The gap-to-gap distance is 0.8 m, as required by the TTF considerations described above, and each cavity is therefore about 1.6 m long. This implies that the LFRF system occupies 3 drift regions, each 5 m long; two cavities will be installed in each drift space, leaving enough room for diagnostics, vacuum ports and instrumentation. The high frequency rf system (HFRF) [8] ranges from 30 to 47 MHz; it is used to accelerate heavy ions with a voltage of 23 KV/gap. To reach the desired TTF the gap distance is 1.6 m and the cavities are run in a  $\pi$  mode. The voltage requirement of above has been calculated assuming the use of 6 double-gap cavities, which will occupy 3 drift regions. Concerning the power delivered to the beam, this is modest compared to losses in the cavities.

### 3.7.3 The Cavity Arrangement

The variation of the ratio  $\nu_s$  of the synchrotron frequency to the revolution frequency for Gold ions is largest soon after injection but never exceeds 0.08, which is considered safe from the beam dynamics point of view. The proposed locations of the rf cavities in the Booster are shown in Figure 3.7.1, and are in zero-dispersion regions. The two types of cavities (HFRF and LFRF) are grouped together so they can be more directly served and operated by the common power supply utility.

**Table 3.7.1: rf Parameters for some Heavy Ion Scenarios.**

	S	Cu	I	Au	U	
Mass Number	32	63	127	197	238	
Charge State	16	27	40	51	54	
Kinetic Energy						
@ injection	16.40	10.39	6.11	4.58	3.86	MeV/u
@ extraction	2.53	2.08	1.37	1.03	0.85	GeV/u
$\beta$						
@ injection	0.1853	0.1483	0.1140	0.0988	0.0908	
@ extraction	0.9632	0.9509	0.9143	0.8802	0.8516	
Orbit Period						
@ injection	4.8	6.0	7.8	9.0	9.8	$\mu$ s
@ extraction	0.9235	0.9354	0.9729	1.0106	1.0445	$\mu$ s
Harmonic No.	24	30	39	45	49	
rf Frequency						
@ injection	5	5	5	5	5	MHz
@ extraction	25.99	32.07	40.09	44.53	46.91	MHz
Full $\frac{\Delta p}{p}$ Bucket						
@ injection	0.038	0.031	0.026	0.022	0.022	%
Bucket Area						
@ injection	8.6	5.5	3.5	2.6	2.4	(meV/u)-s



### 3.8 The Vacuum System

The time spent by the beam in the accelerator is at most 50 msec, corresponding to the 10 Hz repetition rate; thus vacuum requirements are not expected to be very stringent. The most important effects during the acceleration of heavy ions are the loss, and the capture, of electrons by scattering on residual gas. These effects have a pronounced dependence on ion velocity, as shown by the cross-sections [9]:

$$\sigma_{loss} = 4\pi a_o^2 \left(\frac{\alpha}{\beta}\right)^2 \frac{1}{B_n} Z_g(1 + Z_g) f_n \ln\left[\frac{(2\beta\gamma/\alpha)^2}{0.048 B_n}\right] \quad (3.8.1)$$

for electron loss, and

$$\sigma_{capture} = \frac{X_b[(\gamma - 1) + B_n/m_e c^2]^2 \sigma_o}{(\gamma + 2B_n/m_e c^2)^2 - 1} \quad (3.8.2)$$

for electron capture. Here  $\alpha$  is the fine structure constant,  $a_o$  the Bohr radius of the Hydrogen atom,  $Z_g$  is the atomic number of the gas atomic species,  $B_n$  the binding energy of an  $n$ -shell electron in units of Rydbergs (1 Ry  $\sim$  13.6 eV),  $f_n$  is a constant times the oscillator strength for transitions from the  $n$ -shell to the continuum, and  $\beta$  and  $\gamma$  are the relativistic kinematic factors. In Equation (3.8.2)  $m_e c^2$  is the rest energy of the electron,  $\sigma_o$  the photoionization cross section, and  $X_b$  the fraction of the shell of the projectile atom (in the beam) which is unoccupied. The depletion rate is given by

$$\lambda(t) = \beta(t)c \sum_i n_i \sigma_i \quad (3.8.3)$$

where  $n_i$  are the densities of the atomic species in the vacuum gas, and  $\sigma_i$  is the sum of the two cross-sections given by Equations (3.8.1 and 3.8.2). The worst case is represented by Uranium ions, which thus set the vacuum requirement. In order to estimate the overall beam loss, one integrates Equation (3.8.3) over the whole accelerating cycle. Assuming a gas composition of 50% CO and 50%  $H_2$ , a nitrogen equivalent vacuum pressure of  $10^{-8}$  mm Hg is required to keep the overall beam losses to less than 3%.

#### The 3.8.1 The Vacuum Chamber

A vacuum of  $10^{-8}$  mm Hg can be achieved and maintained in a stainless steel vacuum chamber which also provides very effective electro-magnetic shielding of the beam from the magnet laminations. It does however present problems associated with eddy currents. Field distortions, mostly sextupole and decapole components, can be compensated by pole-face windings properly located between the vacuum chamber and the magnet poles of the magnet. The other problem is the power deposited as heat in the vacuum chamber. About 10 kW is dissipated in a full 3.5 m length of 2 mm thick stainless steel vacuum chamber with a width of 15 cm and a height of 10 cm. To absorb the heat dissipation water cooling of the vacuum chamber may be required. The metallic vacuum chamber solution is the most appealing in comparison with other possible solutions, since it provides good vacuum operation conditions and subtracts only marginally from the physical aperture.

## The 3.8.2 The Vacuum Pumps and Valve System

A vacuum of  $10^{-8}$  mm Hg can be obtained with conventional pumping systems. Baking and conditioning of the vacuum chamber may not be required. The rectangular magnet aperture of  $10 \times 15$  cm<sup>2</sup> has a good conductance over the 3.5 m length. Dipole magnets are connected by a cylindrical pipe of 7 cm radius which extends through the quadrupoles. The vacuum chamber in the 22 metre straight sections is also cylindrical with the same radius of 7 cm.

Vacuum ports are located about 5 metres apart next to each of the 48 quadrupoles, with an opening of about 10 cm to which conventional sublimation pumps are attached. Vacuum pressure gauges can be located in the wall facing the vacuum port, in principle at every location, though probably two readings per arc and one per straight section will be sufficient. One or at most two gas analyzers are needed to determine the residual gas chemical composition.

Vacuum valves are located to provide easy access and operation, and to leave sections of beam pipe under vacuum when specific sections are open to atmospheric pressure for maintenance or repair. Considering the size of the ring and its geometry, it is sufficient to provide high quality remotely controlled vacuum valves at each end of the four long straight sections, for a total of eight vacuum valves.

## 3.9 Diagnostics and Instrumentation

The basic unit of the Booster ring is the half-cell, which includes a dipole magnet with a half-quadrupole at each end. There is a drift 0.78 m long between dipoles and quadrupoles. The vacuum chamber is rectangular in the dipole magnets, and circular in the quadrupoles and drifts. Bellows about 10 cm long are located next to the dipole ends. On one side of the quadrupole there is room for a beam position monitor (BPM) and a vacuum port, and on the other side there is a steering dipole. All these elements are about 20 cm long. The BPMs and steering magnets next to QF quadrupoles work in the horizontal plane while those next to QDs operate in the vertical. This layout is also maintained in the long straight sections.

The most fundamental function of the beam diagnostics is to detect beam lateral displacement. This is done with the BPMs, which are essentially pairs of strip lines. The sum of the induced voltages on each plate gives a signal proportional to the beam intensity, and the difference a signal proportional to the beam displacement. The sensitivity of the strip lines has to be adequate to detect each bunch individually; this corresponds to at least  $10^8$  Gold ions with charge state 51, with an order of magnitude difference in the total bunch charge. Sensitivity requirements correspond to a fraction of a millimetre in beam displacement.

The steering magnets are required to correct detectable closed orbit distortions. For this purpose they are individually powered to a maximum current of 100 A, which yields a maximum field of 500 Gauss.

Other useful devices for beam instrumentation are: one longitudinal wide-band detector for measurements of individual bunch length, and a few monitors of the beam transverse dimensions, e.g. multi-wire ionized gas chambers or flying wires.

## References

- [1] "Feasibility Study of a Hadron Facility", Conceptual Design Report, LNL report, February 1992.
- [2] K. Reich, K. Schindl, H. Schönauer. "An Approach to the design of space-charge limited high-intensity synchrotrons", 12th Int. Conf. on High energy Accelerators, Fermilab, 1983.
- [3] L. J. Laslett, "On intensity limitations imposed by transverse space-charge effects in circular particle accelerators", Proc. of 1963 summer study on Storage Rings, BNL-Report 7534 (1963) 324-367.
- [4] B. Zotter, "Proc. of the CERN Accelerator School", Gif-sur-Yvette, September 1984, CERN 85-19.
- [5] J. Wei and S. Y. Lee, Booster Technical Note No. 102/ Dec. 8, 1987/ BNL.
- [6] H. Allen, et al., "Design and operation of the Princeton-Pennsylvania Proton Synchrotron", Proc. of the Intern. Conf. on High Energy Accelerators, Dubna 1963.
- [7] J. Kirchgessner, et al., "The rf system for the Princeton-Pennsylvania Accelerator", Proc. of the Intern. Conf. on High Energy Accelerators, Dubna 1963.
- [8] J. Griffin, "rf summary talk", XV Workshop on the European Hadron Facility, Lecce, October 1989.
- [9] H. Gould et al., Phys. Rev. Lett. 52 No. 3 (1984) 180-183.

## 4

# Transfer Line

An important part of the complex turns out to be the Transfer Line between the two rings, which has been designed to transfer heavy ions, to be capable of producing, collecting and selecting exotic beams.

The production of exotic beams requires a complex system of targeting and of beam species selection that leads to an elaborate design. In fact, the Transfer Line is a replica of half of the Booster ring, with suitable insertions for obtaining specified beam sizes and dispersions, for the location of the ion fragmentation target and for the degrader system for the mass separation of different species. The Transfer Line can be operated at a maximum magnetic rigidity of 22.25 Tm.

The physical location of the Line in the complex is dictated by the position of the experimental hall, which will be north of the rings, and by the position of the rings with respect to the injector. Extraction from the Booster is on the west straight section of the ring, and injection into the Decelerator ring is on the opposite one, about 2.5 metres above the Booster. The Line lies between the two rings, and combinations of kickers and bending magnets bring the beam from the Booster to the Line, and from the Line to the Decelerator. The horizontal distance between the Transfer Line and the rings is large enough ( $\sim 40$  m) to allow space for radiation shielding.

### 4.1 Secondary Beam Production

Heavy-ion beams of energy  $\sim 1$  GeV/u have attractive features (compared to lower energies) for producing exotic nuclei and studying them after separation in an energy loss achromat like the one described below. These features are:

- production targets as thick as  $1\text{-}2\text{ g/cm}^2$ ,
- full stripping, even for very heavy products, with unambiguous isotope separation and assignment,
- strong forward peaking for projectile fragments from peripheral collisions. The last feature is of particular importance, since it means that ion fragments are produced at essentially the velocity, and therefore the specific energy, of the primary particles.

For beam energies of the order of 1 GeV/u, the total cross-section for the fragmentation process depends essentially on the interaction radii according to

$$\sigma_I = \pi[R_p^2 + R_t^2] \quad (4.1.1)$$

where the subscripts  $p$  and  $t$  stand for projectile and target. The interaction radius of a nucleus with mass number  $A$  is  $R \sim A^{1/3} \times 10^{-13}$  cm independent of the energy [1]. Typical values of  $\sigma_I$  are of the order of few barns.

A great variety of fragments with different mass and charge values are produced in the process. The cross-section for a single isotope of given  $A$  and the most probable  $Z$  is of the order of ten to one hundred millibarns. Detailed calculations of the cross-section, performed within the framework of the abrasion-ablation model and Giant Dipole Resonance excitation followed by one evaporation stage, describe some of the principal features of the mass and charge distribution of the fragments, but slightly overestimate the experimental data [2,3]. The cross-section is simply given by

$$\sigma(A, Z) = \pi R^2 \frac{\binom{Z_1}{z} \binom{N_1}{n}}{\binom{A_1}{a}} \quad (4.1.2)$$

where  $A_1$ ,  $Z_1$  and  $N_1$  are respectively the total number of nucleons, protons and neutrons in the target nucleus before interaction and  $a$ ,  $z$  and  $n$  are respectively the number of nucleons, protons and neutrons removed in the interaction, so that  $A = A_1 - a$  and  $Z = Z_1 - z$  (J. O. Rasmussen et al., unpublished, see ref. [2]). Typically, a fragment nucleus has the same overall dimensions as the projectile, i.e.  $z \ll Z_1$  and  $a \ll A_1$ . Thus, the secondary beam is likely to have a specific energy not very different from that of the primary beam.

The longitudinal momentum dispersion of the fragments in the projectile rest frame is well described by a Gaussian distribution of width given by

$$\Delta p_{\parallel} = \sigma_o \sqrt{\frac{A_f(A_p - A_f)}{A_p - 1}} \quad (4.1.3)$$

where  $A_p$  and  $A_f$  are the numbers of nucleons in the projectile and fragment nucleus [4]. The constant  $\sigma_o$  is related to the Fermi momentum  $p_F$  of the nucleons in the projectile by  $\sigma_o = p_F/\sqrt{5}$ . The experimental value of  $\sigma_o$  is  $94 \pm 5$  MeV/c. It has also been shown [5] that, to within 10% error, the transverse momentum dispersion is given by:

$$\Delta p_{\perp} = \Delta p_{\parallel} . \quad (4.1.4)$$

## 4.2 Targetry

The Transfer Line and the fragment collection system are designed for the capture and transfer of a full momentum spread of 0.7%, which corresponds to the capture of almost all the ions of the required species. Similarly the production angle is taken to be 7.5 mrad, corresponding to a transverse momentum spread which matches the momentum width. The expected yield can then be as large as  $10^{-3}$ , and typically  $10^8 \div 10^9$  fragments per second of assigned mass number  $A$  and atomic number  $Z$  can be collected.

The production target is placed at a waist in the Transfer Line where  $\beta \sim 1$  m. The full emittance of the primary beam being about  $5 \pi$  mm-mrad, the beam size at the target is 2.3 mm. The production target is no more than 10 mm long, and therefore the emittance of the secondary beam is given by the product of the size of the primary beam and the

maximum angle at which secondaries are emitted; this implies a full value of  $17 \pi$  mm-mrad. Based on these figures, the betatron acceptance of the Transfer Line and of the Decelerator ring is set conservatively to  $40 \pi$  mm-mrad, and the momentum aperture to 2%.

The production target is located in a dispersion-free insertion to avoid correlations between the energy and position of an event; this improves fragment selection and secondary beam emittance. Looking backward at the target, the Transfer Line is to be matched to the beam phase-space ellipses; thus the Transfer Line must be able to tune the section preceding the production target and the section following independently, with different matching values of  $\beta^*$ 's.

### 4.3 Description of the Line

Extraction from the Booster ring is by a vertical kicker followed by a horizontal Lambertson magnet located  $90^\circ$  downstream in vertical phase [6]. The Transfer Line, shown in Figure 4.3.1, starts with two doublets separated by a horizontal bending magnet similar to the lattice dipoles, to direct the beam orbit parallel to the ring straight section. The two doublets provide dispersion suppression and a waist in the horizontal and vertical planes at the fragmentation target, which is placed at the centre of a 3 metre long drift. The  $\beta^*$  value at the waist is 1 metre in both planes. The horizontal bending dipole, similar to the lattice dipoles, can be designed with a wider vacuum chamber to allow the passage of the undeflected primary beam towards experimental halls for the 1 GeV/u physics and the  $\pi$ ,  $\mu$  and electron test beams production.

An insertion about 20 metre long overall is required to match the lattice parameters of the two standard FODO cells that follow. These provide the initial bending of the beam back towards the rings, and a phase advance of  $180^\circ$  in the horizontal plane between the fragmentation target and the selection region.

Momentum selection of the fragments is done with pairs of collimators and slits in an 8 metre long drift, which follows the two bending cells and has a large dispersion ( $\sim 5$  m). There is a double waist at the centre of the drift with  $\beta^* \sim 1$  m, where the degrader is located. This has a variable thickness in the horizontal plane [7], and it is located in a large-dispersion region. Thus particles with different momenta will cross different thicknesses of the degrader material and lose different amounts of energy depending on their velocity. For the given momentum dispersion the degrader is shaped to match the velocity dispersion for only one mass number, in such a way that the subsequent arc, made of two FODO cells, will exactly realize the achromaticity condition (compensation of the previously produced velocity dispersion) only for the required species. At the centre of the 20 metre drift, half way along the transfer line, there is a waist with a large  $\beta^*$  ( $\sim 10$  m) where additional slits are located for the final selection of the required ion fragment.

The second half of the Line has two empty insertions corresponding to the degrader and to the target locations, which can be used for other applications. The latter insertion is long enough to accommodate the dipoles for the vertical displacement of the beam from the elevation of the Booster to the elevation of the Decelerator ring; vertical dispersion can also be corrected locally by means of properly placed quadrupoles.

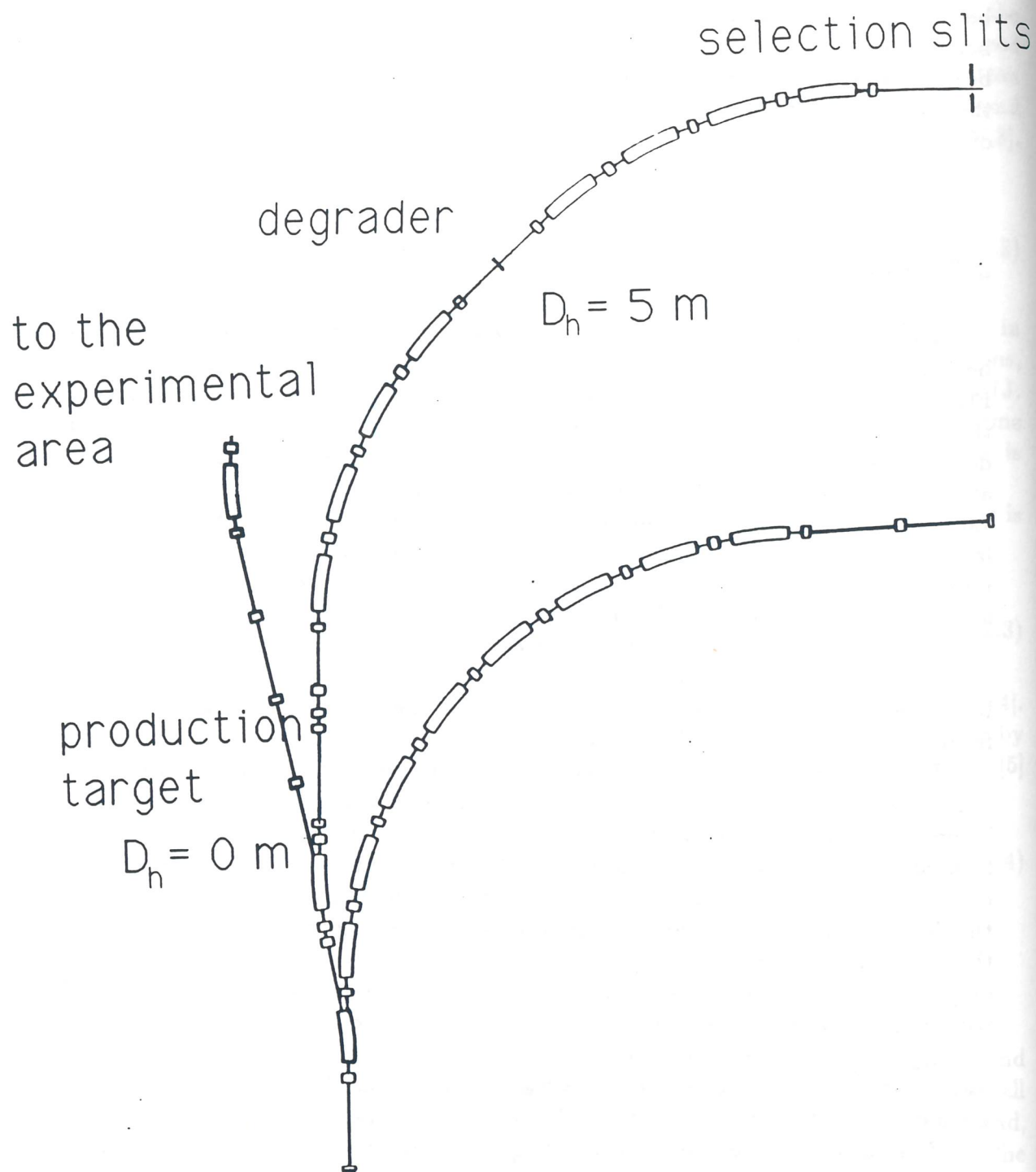


Figure 4.3.1: The Isotopes Selection Line and the extraction channel.

## References

- [1] H. Sato et al., Phys. Rev. C 34, (1986) 2171.
- [2] D. J. Morrissey et al., Phys. Rev. C 18 no. 3, (1978) 1267.
- [3] L. F. Oliveira et al., Phys. Rev. C 19 no. 3, (1979) 826.
- [4] A. S. Goldhaber, Phys. Lett. 53B, (1974) 306.
- [5] D. E. Greiner et al., Phys. Rev. Lett. 35 no. 3, (1975) 152.
- [6] "Feasibility Study of a Hadron Facility", Conceptual Design Report, edited by LNL, February 1992.
- [7] J. P. Dufour et al., Nucl. Instr. and Meth. A248, (1986) 267-281.

# 5

## Decelerator Ring

### 5.1 Lattice and Operation Cycle

The main functions of the Decelerator are the accumulation and storage of many pulses of ion fragments, the cooling of the stored beam, and the deceleration of the beam down to energies corresponding to the Coulomb Barrier. Moreover the ring can be used for fast extraction operation or as a Stretcher, in all the working energy range.

#### 5.1.1 The Lattice of the Decelerator.

To accommodate all these functions, the lattice of the Decelerator has to provide space for injection and extraction, dispersion-free locations for the rf cavities, and a drift space at least 10 metres in length for electron cooling. Moreover the ring must be able to match the rigidity of the Booster of 22.25 Tm. The estimated cost and the space available on the LNL site suggest a solution where both rings are housed in the same tunnel, on the top each other. A convenient solution is to have exactly the same circumference and geometry for the two rings [1].

Like the Booster, the Decelerator has a superperiodicity of four, each superperiod being mirror symmetric and consisting of an arc and a straight section, as shown in Figure 5.1.1. The arc is identical to the Booster arc, with a basic FODO cell which parameters are listed in Table 3.1.2. The straight section of the Decelerator has the same length as the one in the Booster, about 22 metres; a different quadrupole configuration is used to provide a 11 metres long magnet-free central region for electron cooling. The main parameters of the lattice of the Decelerator are listed in Table 5.1.1, and the lattice functions for a superperiod (one fourth of the ring) are shown in Figure 5.1.2. As can be seen, the long straight sections are essentially dispersion-free.

In addition to the QF and QD quadrupole families in the arcs, quadrupoles Q1, Q2 and Q3 are provided at the ends of each long straight section to allow tuning and matching of the lattice. The phase advances in the FODO cells are about  $90^\circ$  and  $60^\circ$  in the horizontal and vertical planes respectively, and the total betatron tunes are set to  $\nu_h = 5.8$  and  $\nu_v = 3.8$  as in the Booster. The transition energy has the same value as in the Booster ring. The positions of other components, for injection, extraction, RF acceleration, and electron and stochastic cooling are shown in Figure 5.6.1.

The momentum aperture required for the stacking of several beam pulses is a total of 2% while the requirement on the betatron acceptance is  $40 \pi$  mm-mrad in both planes.

Taking a linear combination of the two contributions to the beam size, the beam envelope in the ring is plotted in Figure 5.1.3.

### 5.1.2 The Operation Cycle

The two-second operation cycle is shown schematically in Figure 5.1.4, as an example. In practice, the operation cycle as well as the extraction energy can be adjusted to match the user requests. Twelve pulses of ion fragments are transferred to the Decelerator ring, separated by 100 ms. The bunches of each pulse are captured in stationary buckets which are then rotated in longitudinal phase space. The momentum spread of the beam will therefore change from 0.7% at capture to 0.1% after the rotation. The beam bunches are then displaced by a second system of rf cavities to a new momentum trajectory where they are stored. On the stacking orbit, electron and stochastic cooling operate on the beam, and continue for another 0.5 sec after all 12 pulses have been accumulated. Figure 5.1.5 illustrates the use of the momentum aperture, the location and relative dimensions of the beam during the cycle.

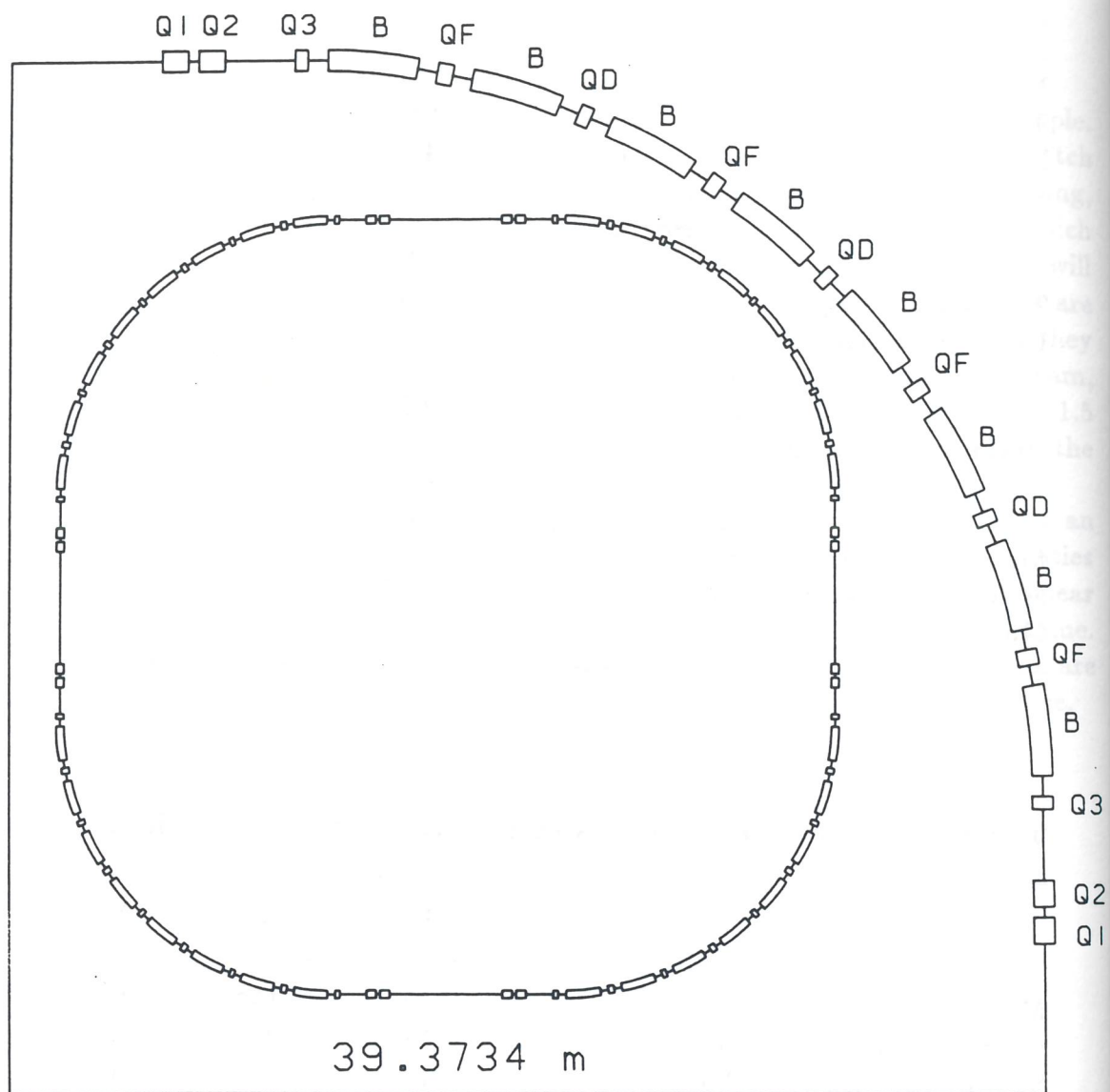
The cooling reduces the beam momentum spread and the betatron emittances by an order of magnitude. Finally, the beam stack is captured by one more system of rf cavities which decelerates it down to energies of about 5 MeV/u. The deceleration stage is linear and lasts 0.3 sec; during the subsequent 0.1 sec the guiding field is reset to its initial value. The cycle then repeats. The main beam parameters at injection into the Decelerator are listed in Table 5.1.2 where some stable fully stripped species has been taken as reference.

**Table 5.1.1: Parameters of the Decelerator.**

Ring Length	266.6667	m
Lattice Periodicity	4	
Maximum Magnetic Rigidity	22.25	Tm
Magnetic Bending Radius	17.6216	m
Total Number of Cells	24	
Number of Cells per Arc	4	
Phase Advance per Cell		
Horizontal	90°	
Vertical	60°	
Transition Energy ( $\gamma$ )	4.6	
Betatron Tunes		
$\nu_h$	5.8	
$\nu_v$	3.8	
Natural Chromaticity		
$\xi_h$	-5.5	
$\xi_v$	-5.98	
Max. Horizontal Dispersion	4.95	m
Max. Hor. Beta Function	17.50	m
Max. Vert. Beta Function	31.0	m

**Table 5.1.2: Beam Parameters at Injection into the Decelerator.**

	S	Cu	I	Au	U	
Mass Number, A	32	63	127	197	238	
Charge State, Q=Z	16	29	53	79	92	
Specific Kin. Energy	2.53	2.08	1.37	1.03	0.85	GeV/u
$\beta$	0.963	0.951	0.914	0.880	0.852	
Number of Bunches	24	30	39	45	49	
Bunch length (rms)	0.5	0.5	0.5	0.5	0.5	ns
Momentum spread	0.7	0.7	0.7	0.7	0.7	% (full)
Intensity	$4.0 \cdot 10^9$	$1.6 \cdot 10^9$	$5.0 \cdot 10^8$	$1.5 \cdot 10^8$	$1.5 \cdot 10^8$	ions/s



Decelerator : General layout of magnetic lattice

Figure 5.1.1: The Layout of the Decelerator.

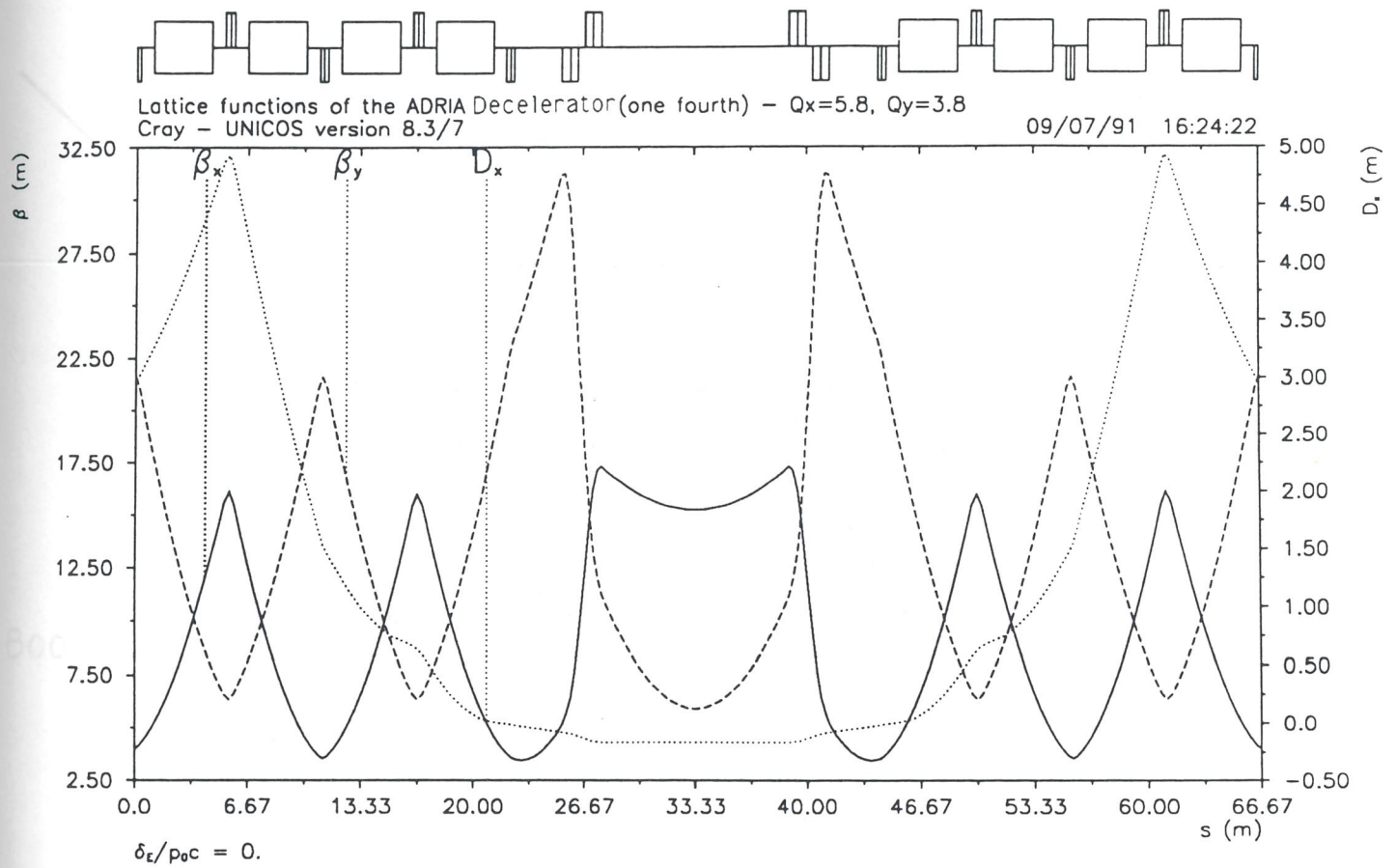


Figure 5.1.2: Lattice Functions of the Decelerator.

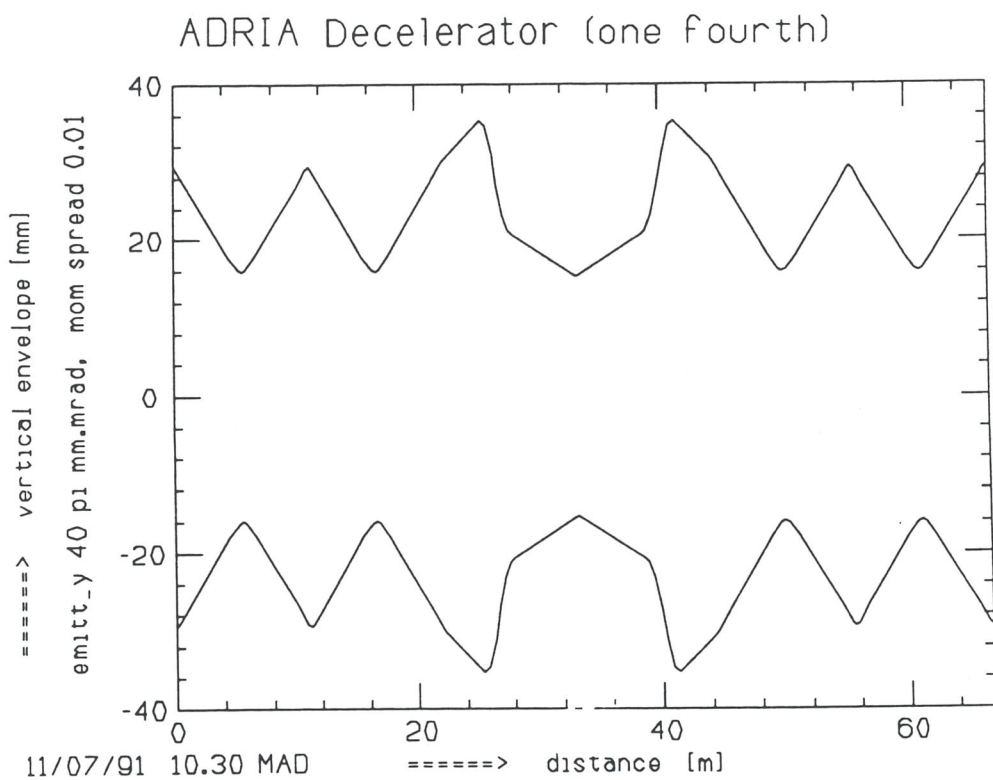
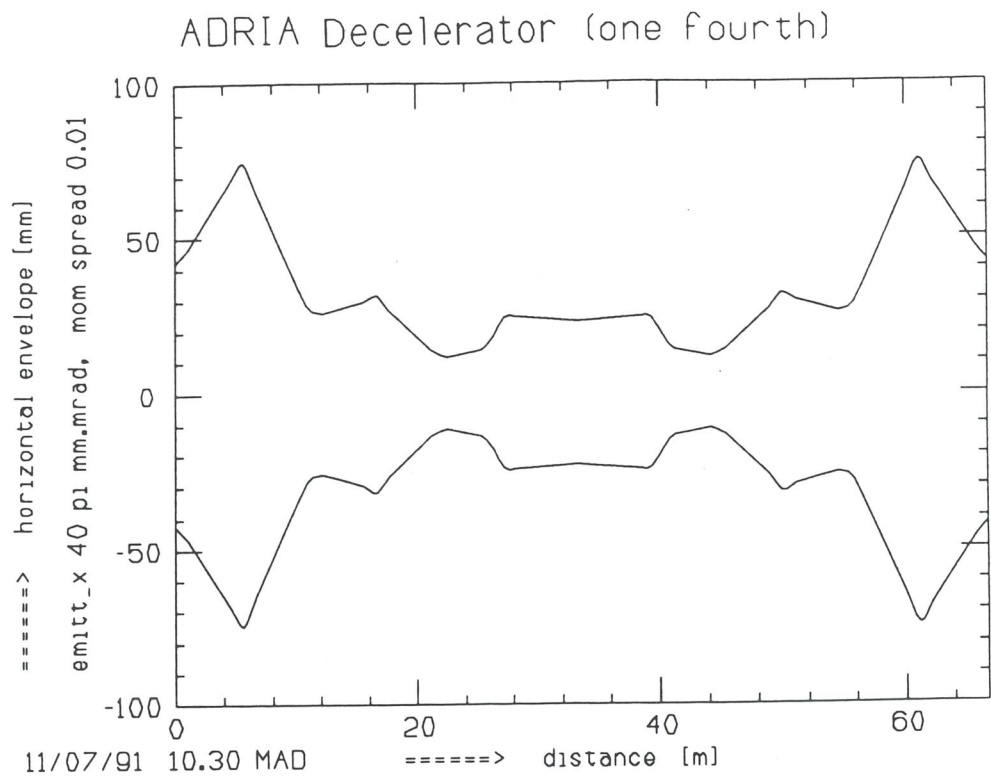


Figure 5.1.3: Beam Envelopes in the Decelerator.

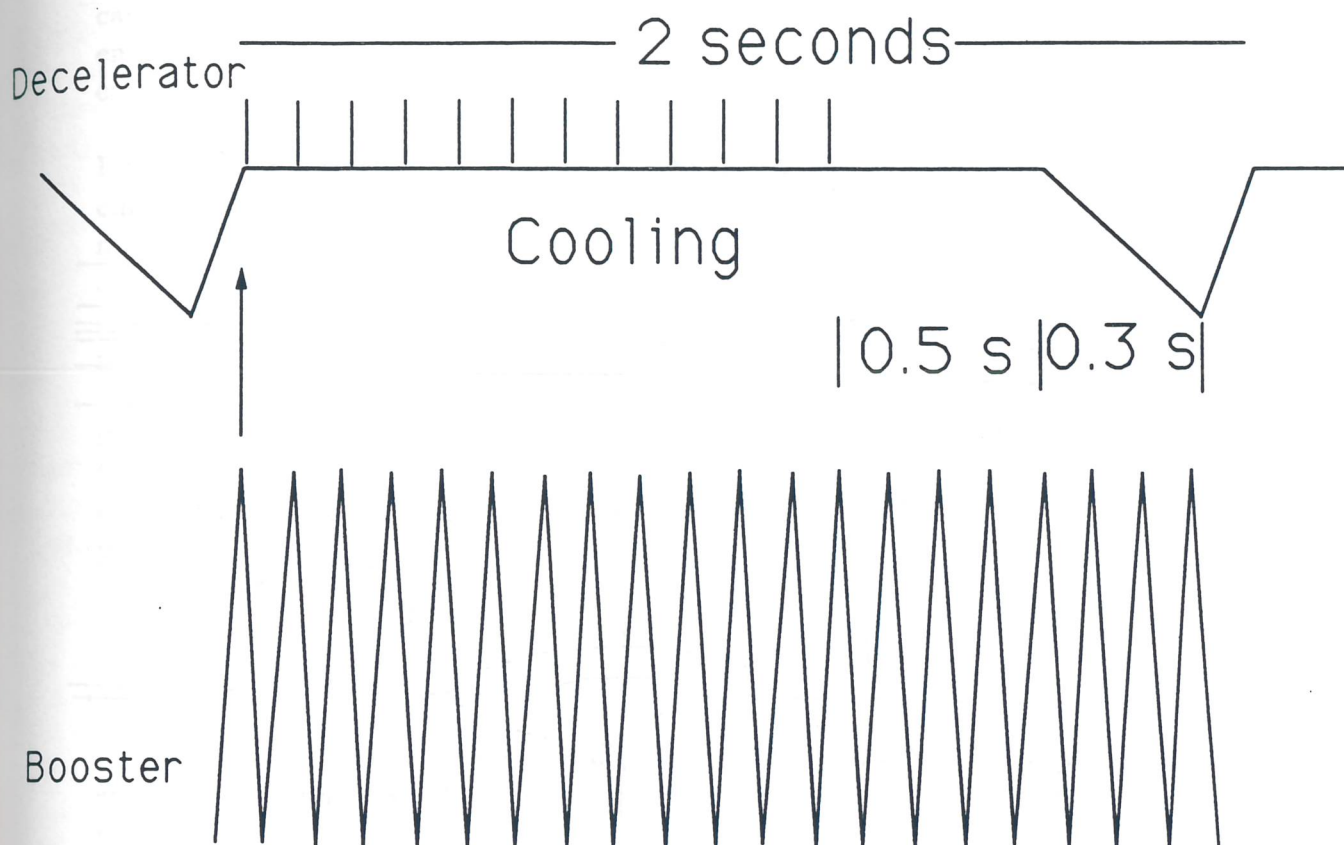


Figure 5.1.4: Magnetic Cycle of the ADRIA Complex.

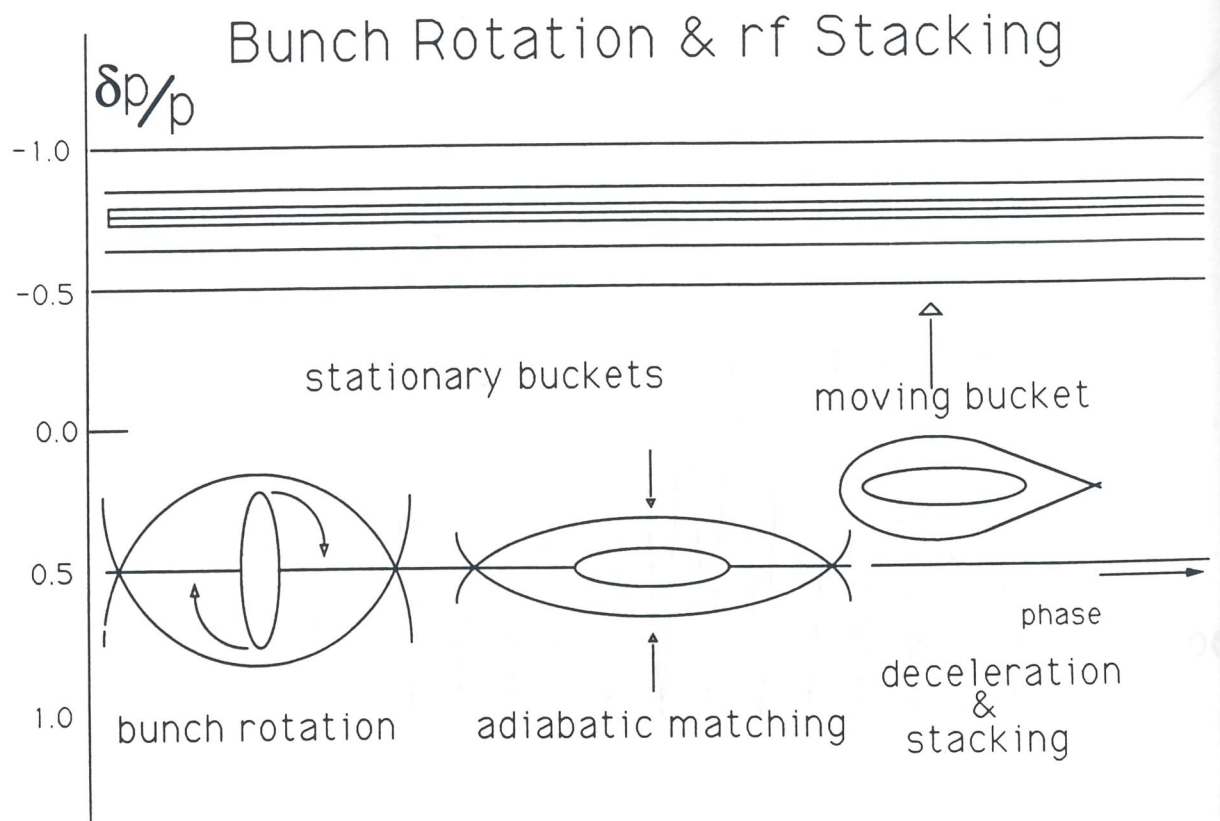


Figure 5.1.5: The momentum aperture of the Decelerator ring.

## 5.2 Injection

Injection into the Decelerator ring is the exact converse of extraction from the Booster; because the rings are the same size, one turn is injected at a time. The magnets are identical in all to those used from extraction from the Booster and have the same parameters. The beam enters the Decelerator with a vertical pitch; the septum magnet moves the beam vertically inside the ring and places it on the median plane 65 mm close to the reference orbit. The kicker magnet finally kicks the beam horizontally onto the reference orbit. One can take advantage of the smallness of the transverse beam dimensions at the transfer energies and locate the 10 mm thick septum 35 mm away from the central orbit; this is enough to preserve the required betatron acceptance in the Decelerator.

With the typical cycle described in section 5.1.2, beam pulses are transferred to the Decelerator at intervals of 100 ms. After electron cooling, the circulating beam has smaller emittances than the injected pulse. It is then preferable that injection of the new pulse does not perturb its dimensions and that, eventually one allows the kicker to dilute the emittances of the stack. This is accomplished by first moving the circulating beam by up to 30 mm on a bumped orbit which is prepared slowly just before injection of the new pulse. As soon the new pulse is injected, the kicker is turned off in 150 ns, and the local bump is also turned off over a longer time corresponding to several revolutions. With this method the stack will initiate coherent oscillations which will dilute the beam emittances to the initial value, while the emittances of the injected beam are unchanged. Electron cooling will then reduce the emittances of the total beam down to a value acceptable for the injection of the subsequent pulse.

## 5.3 Extraction

Depending on the experimental program, the beam may be extracted from the Decelerator in a single turn ( fast extraction ), or over many turns to provide 100% duty cycle ( resonant extraction ).

The Decelerator can be operated as a Stretcher at the Booster extraction energy, or, after deceleration of the accumulated fragments, at energies as low as 5 MeV/u. The duration of the spill may vary from 100 ms to a few seconds depending on the energy and the mode of operation.

For fast extraction the procedure is similar to the one used for extraction from the Booster, and the septum and kicker magnets have similar characteristics, as described above. The only relevant change, with marginal consequences, is that the lattice of the long straight section in the Decelerator ring is different.

To accomodate resonant extraction from the Decelerator, a large horizontal beta function is required in the long straight section where the electrostatic septum is to be installed. A beta function value of about 50 m can easily be obtained by tuning the triplets at both ends of the insertion. Resonant extraction can then be done with either a half-integer or a third-order resonance.

The beam spill can be obtained with a half-integer resonance by adjusting the horizontal tune to a value just bigger than 5.5 and then approaching the resonance from above. A diametrically opposed pair of perturbing quadrupoles, powered oppositely so as to create an 11th harmonic perturbation without exciting a 0th harmonic signal, is used to create

a narrow stop-band centred about  $\nu_h = 5.5$ . At the same time a pair of octupoles are powered so as to make the tune amplitude-dependent. During extraction the perturbing quadrupoles are ramped up while the octupoles are fixed in strength. Particles with large betatron amplitude will enter the half-integral stop-band first; their motion will be unstable and move away from the central orbit towards the electrostatic deflector. Parameters are adjusted so that, between two consecutive turns, a particle has a better than 99% chance to be extracted cleanly without hitting the wires of the electrostatic septum.

Resonant extraction can also be performed by means of a third-order resonance. In this case, the betatron tune is first adjusted to just above the third-order value  $\nu_h = 5.667$ , and the resonance is created with a pair of sextupoles located in such a way to generate the 3  $\nu_h = 17$  harmonic. If the sextupoles which compensate for the natural chromaticity are turned off, the particles will acquire a betatron tune which is momentum dependent. During the spill, the sextupoles are ramped up so that the stable region shrinks; first the particles with lower momentum, i.e. higher tune, will leave the stable region. Seen from the electrostatic septum, the particles will move away from the centre along one of the separatrices towards the septum wires.

## 5.4 The Magnet System

The Decelerator lattice consists of 32 bending magnets, 16 horizontally focussing quadrupoles (QF) and 12 vertically focussing quadrupoles (QD). In addition there are 8 quadrupoles of Q1, Q2 and Q3 type, respectively of length 1 m, 1 m and 0.5 m. The magnet cycle of the Decelerator operation is shown in Figure 5.1.4. The flat top of the cycle, which lasts 1.6 seconds, accommodates multi-turn injection and time to cool the secondary beam coming out of the target in the Transfer Line. The magnetic rigidity of the beam is reduced following the charge state ratio before and after the production target; according to different species the injection magnetic field ranges between 0.74 T (Uranium) and 1.26 T (Sulfur). After deceleration down to a few MeV/u the required magnetic field is reduced to 0.12 T for the Uranium case and to .069 T for the Sulfur ion. Deceleration takes place in 0.3 sec and the reset time is 0.1 sec. A possible choice for the magnet design, driven by both economic and technical considerations, is to make use of the Booster design; because of the lower frequency, the number of the dipole subconductors is reduced to 3, as shown in Figures 5.4.1 and 5.4.2, maintaining the same coil dimensions. Consequently the specifications are the same as those described in section 3.5. Parameters for the bending magnets and the quadrupoles are listed in Tables 5.4.1.

**Table 5.4.1: List of parameters for the Decelerator Magnets.**

Parameter	Unit	dipoles	Quad F	Quad D
Number of Magnets		32	16	12
		sector magnet curved with sagitta 8.5 cm		
Bending Radius	m	17.62	—	—
Magnetic Length	mm	3460	600	500
Pole Tip Radius	mm	—	70	70
Maximum Field	T	1.26	—	—
Maximum Gradient	T/m	—	8.7	8.7
Maximum Current	A	5086.	4419.	4419.
Max Current Density	A/mm <sup>2</sup>	4.6	6.0	6.0
DC Resistance/magnet	mΩ	2.910	0.764	0.655
Inductance/magnet	mH	5.50	0.34	0.34
Dissipated Power,total	MW	2.10	0.214	0.132
Copper Weight	ton	1.45	0.185	0.160
Iron Weight	ton	13.6	0.680	0.550

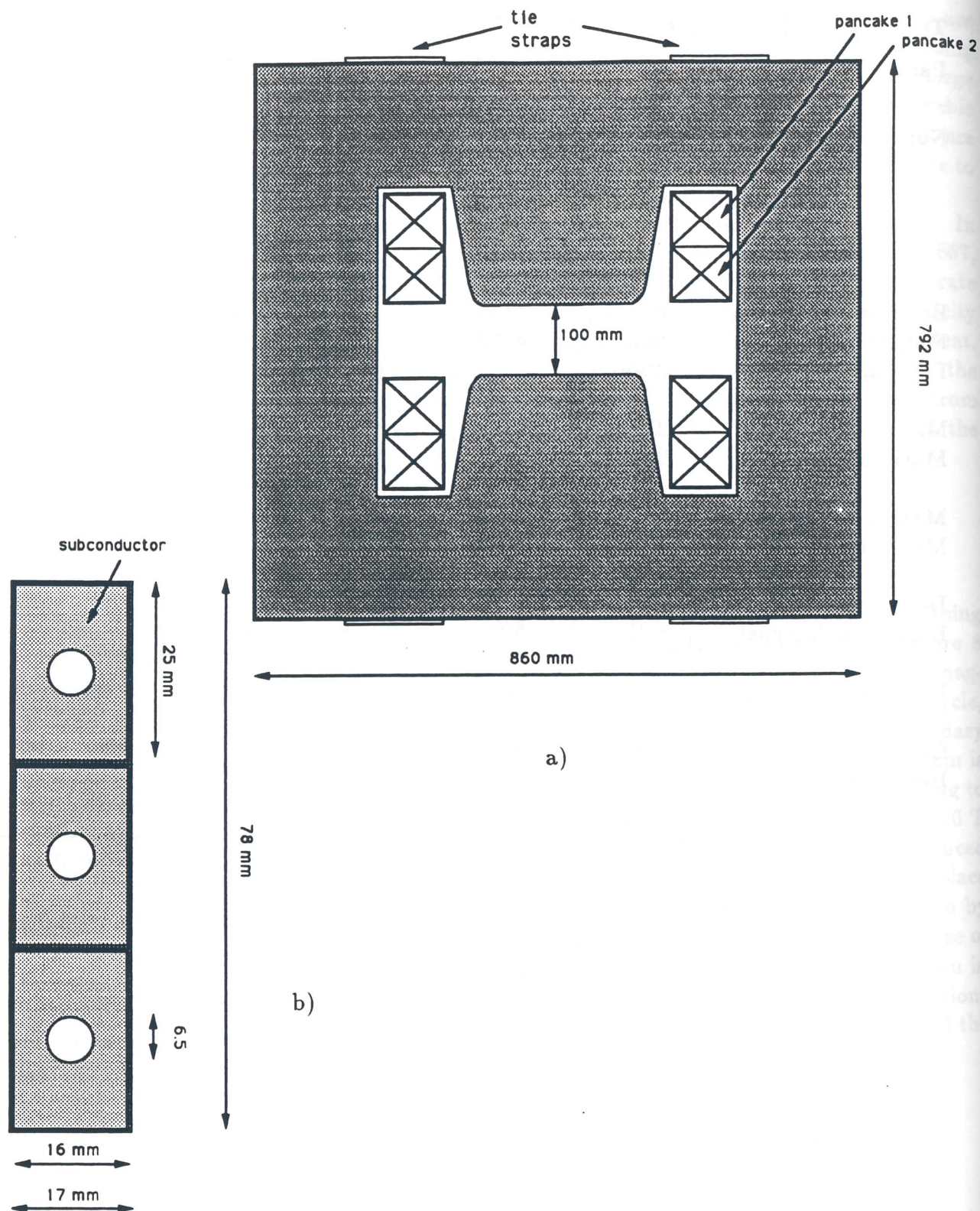


Figure 5.4.1: a) Cross-Section of the Dipole Magnets;  
 b) Cross-Section of the Dipole Conductor.

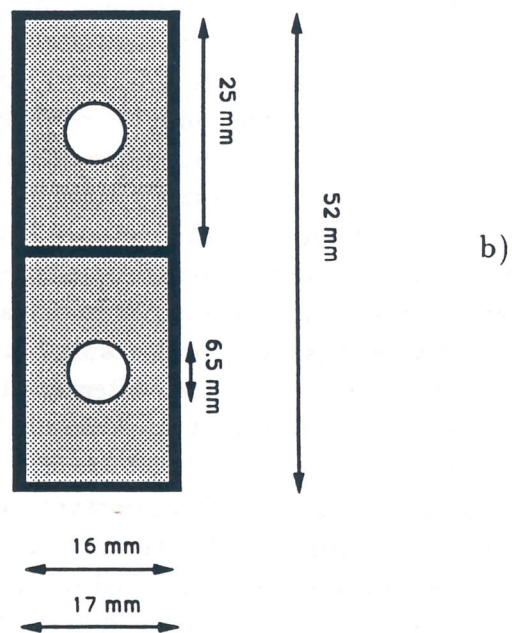
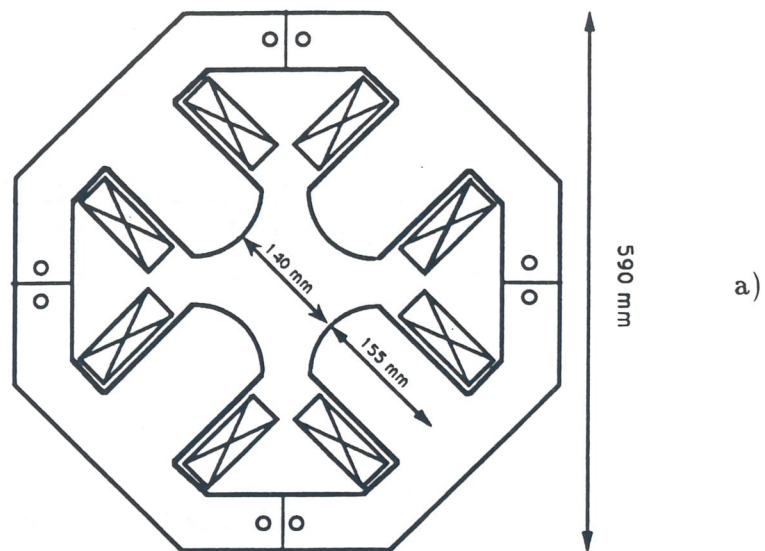


Figure 5.4.2: a) Cross-Section of the Quadrupole Magnets;  
b) Cross-Section of the Quadrupole Conductor.

## 5.5 Power Supply

Because of the special magnet cycle, the Decelerator is ramped with a digital power supply. A resonating system seem unsuitable because of the relatively slow variation of the guide field, and because of the form of the cycle.

## 5.6 rf System

The rf system in the Decelerator has to fulfill three purposes: capture and bunch rotation, rf stacking, and deceleration. All these functions are accomplished with a dedicated rf system as explained below.

### 5.6.1 Bunch Rotation

After being produced at the target in the Transfer Line between the Booster and the Decelerator, bunches of heavy ion fragments are injected into the Decelerator in a single turn. The corresponding beam parameters are listed in Table 5.1.2. The nominal kinetic energy is roughly equal to that of the primary beam. The bunches are 0.5 ns long (rms) for all species, the same length as the bunches of primary particles before they hit the target. Fragments are captured with a full momentum spread of 0.7% for all species. Because the selected species have mass numbers fairly close to that of the primary beams, the operation can be described with reference to the isotopes listed in Table 5.1.2, fully stripped; there is indeed no requirement to accumulate exotic elements with mass number below 30.

After injection, the beams are captured in a sequence of stationary buckets, with a height chosen so that a mismatch will result between the shape of the bunches and the buckets. The bunches then rotate and, after one quarter of a synchrotron oscillation, they have traded momentum spread for bunch length; they are now longer and have a smaller momentum spread [2].

For efficient bunch rotation, it is important to select a bucket height that optimizes the reduction of the momentum spread without introducing unnecessary nonlinear distortions. Experience has shown that a bucket height 1.4 times the momentum spread is a good choice. If the frequency of the rf buckets is chosen equal to the bunch spacing then a reduction of the momentum spread, or equivalently an increase of the bunch length by a factor of seven can be expected.

The required frequencies and voltages for different ion species are ranging between 26 - 47 MHz and 0.15 - 1.4 MV, respectively. The most demanding case corresponds to the heaviest ions. The 'Rotation Period', i.e. the time needed to accomplish the rotation efficiently, it is about one third of one synchrotron period. Towards the end of the rotation, the rf voltage must be quickly reduced to the smaller value required for matching the rf buckets to the shape of the bunches.

The tuning range required for bunch rotation ( 26 to 47 MHz ) can be achieved with a

set of tuners at proper locations along the cavity.

A critical task is to turn off the cavities in a very short time. This is done by abruptly inverting the loadline of the amplifier so that the tetrodes run at very high peak currents for a few cycles and absorb most of the energy from the cavity [1]. Since for the operation of the Decelerator it is necessary to turn the rf off in about  $10\ \mu\text{s}$ , some improvements of the present technology are required. For instance, it will be necessary to design in a proper way the loop that couples power into and out of the cavity: the rate at which the cavity can be turned off depends upon the rate at which flux is coupled into the driving loop. This is limited by current, voltage and series inductance. Should an optimum trade-off between these parameters prove to be insufficient, a further improvement may be obtained with a dedicated loop activated by fast switching devices.

It is reasonable to assume two cavities for bunch rotation, each capable of producing 700 KV. It is then necessary to turn the voltage down to a low value of a few tens of kilovolts so that the rf buckets are matched in shape to the bunches at the end of rotation. After this point, to avoid problems with multipactoring, the voltage is maintained on each cavity; yet the total effective voltage as seen by the beam can be reduced essentially to zero in few milliseconds by driving the two cavities at opposite phases.

The cavities are about 1.5 metres, allowing two of them to fit comfortably in one of the long straight sections of the Decelerator as shown in Figure 5.6.1.

## 5.6.2 rf Stacking

Once the beam bunches have been rotated, they must be slightly decelerated to an inner orbit where they are released on top of the previously stored pulses. On this orbit the beam is cooled by an electron beam and by stochastic cooling. The operation of rf displacement is performed by a second rf system.

The rf displacement decelerates the beam by an amount corresponding to a momentum variation of -1.2%. The momentum spread of the beam at the end of bunch rotation is about 0.1 - 0.2% for all species, and the bunch length spans almost the full rf bucket length. As the bunch rotation system is turned off, the new rf system is turned on at the same frequency so that the beam bunches remain trapped by stationary buckets. By changing the synchronous phase angle of the second rf system, the rf buckets move and decelerate the beam. To minimize the amount of rf voltage, the synchronous phase is kept as low as possible; the deceleration to the inner orbit takes a time which is typically several milliseconds. At the end of the displacement, the rf cavities are turned off adiabatically, releasing the bunches. The rf cavities required for this operation are similar to that used for the bunch rotation. This system must be able to run at all the frequencies at which bunch rotation is done, to capture the beam and to decelerate it to a 1.2% lower momentum, which corresponds to a frequency swing of a fraction of one percent. To do this the stacking cavity uses a tuner that provides the frequency shift, in addition to the tuner used to set the initial frequency as done for the bunch-rotating cavities. This is possible because the voltage required is now considerably lower (less than 84 KV).

The total voltage required can be provided with two cavities, again 1.5 metres long, which are located as shown in Figure 5.6.1. To turn effectively the voltage off and to vary the synchronous phase angle, the two cavities are operated at opposite phases.

### 5.6.3 Deceleration of Heavy Ions

The third system of rf cavities, with frequency ranging from 5 to 47 MHz, is required for the deceleration of beams at the end of the stacking and cooling process. A final momentum spread of about  $10^{-4}$  for all ion species is expected after cooling. The rf is turned on adiabatically to bunch and capture the coasting beam, at the same harmonic number selected in the corresponding acceleration process in the Booster. The beam is decelerated from the initial specific kinetic energy of few GeV/u to about 5 MeV/u, which corresponds to the Coulomb barrier. The magnetic field cycle of the Decelerator during the deceleration proper, the field varies linearly over a period of 0.3 sec. The beam parameters and the rf requirements are listed in Table 5.6.1, the voltage and frequency requirements are approximatively the same for all ion species and a total of 50 KV is needed. Deceleration stops at the lowest rf frequency of 5 MHz.

The rf cavities for deceleration are similar to those employed for acceleration in the Booster since the same voltage per gap and frequency modulation are required. It is estimated that four of these cavities are needed, two of the LFRF and two of the HFRF type; their location is shown in Figure 5.6.1.

**Table 5.6.1: Parameters of the Deceleration Ramp**

	S	Cu	I	Au	U	
Harmonic No.	24	30	39	45	49	
Bunch area (rms)	0.0073	0.0062	0.0043	0.0034	0.0029	eV/u-s
Normal. Emittance	12.8	10.5	7.9	6.7	6.0	$\pi$ mm-mrad
<u>Top of Cycle</u>						
Kinetic Energy	2.53	2.08	1.37	1.03	0.85	GeV/u
$\beta$	0.963	0.951	0.914	0.880	0.852	
Magnetic Field	1.263	1.176	0.953	0.815	0.741	T
RF Frequency	25.99	32.07	40.09	44.53	46.91	MHz
Emittance	3.56	3.43	3.50	3.59	3.68	$\pi$ mm-mrad
<u>Bottom of Cycle</u>						
Kinetic Energy	16.45	10.43	6.13	4.59	3.87	MeV/u
$\beta$	0.186	0.148	0.114	0.099	0.091	
Magnetic Field	0.0665	0.0574	0.0485	0.0437	0.0416	T
RF Frequency	5.00	5.00	5.00	5.00	5.00	MHz
Emittance	67.6	70.1	68.7	67.0	65.4	$\pi$ mm-mrad

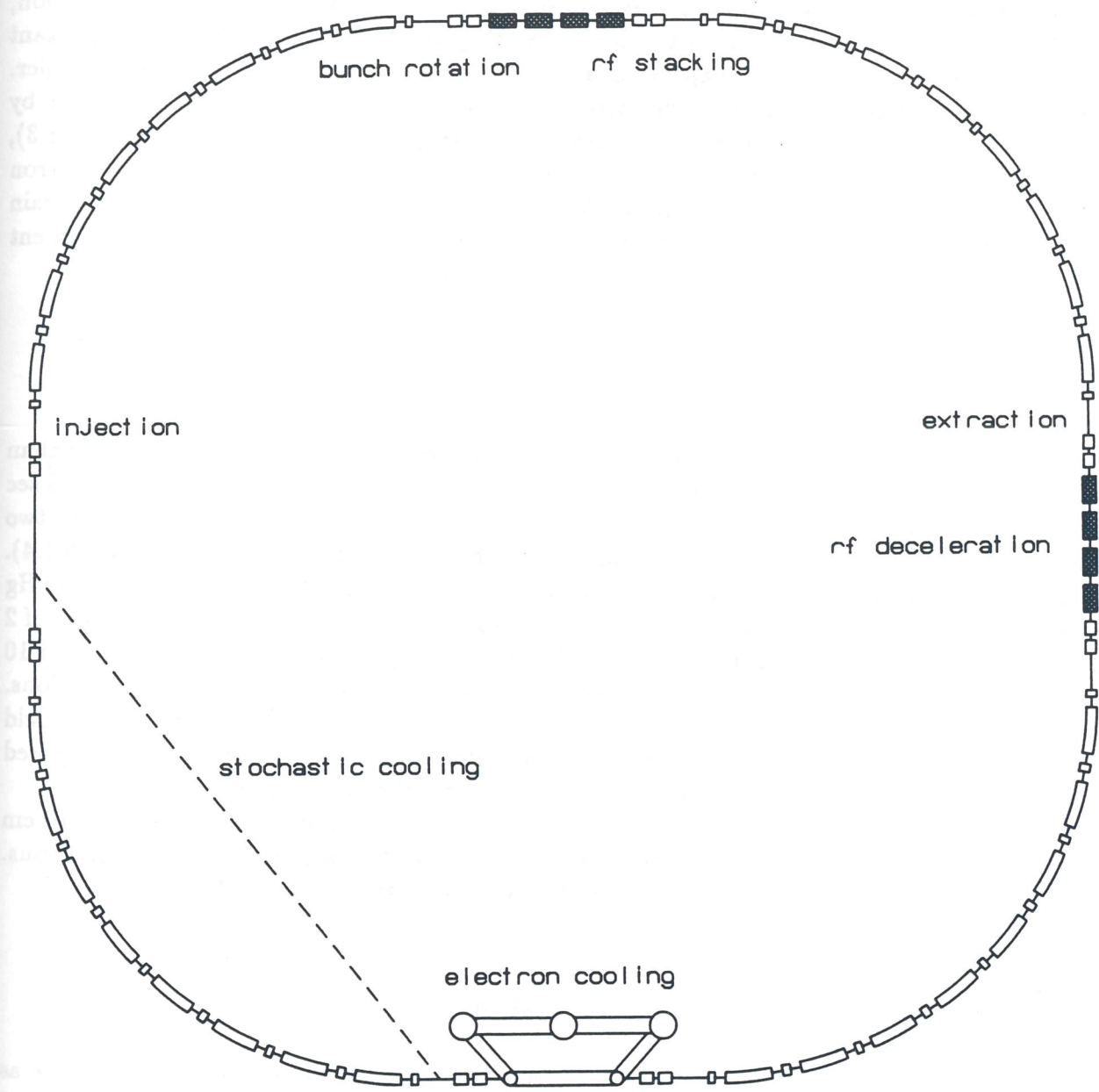


Figure 5.6.1: Components Arrangement in the Decelerator.

## 5.7 The Vacuum System

The same considerations that applied to the vacuum in the Booster also apply to the vacuum in the Decelerator. Heavy ions are stored in the Decelerator ring for as long as 2 seconds. For most of this time the particles circulate at maximum energy, but then they are decelerated down to about 5 MeV/u over a time of 0.3 sec; at the end of the deceleration, the velocity  $\beta$  is only  $\sim 0.1$ . Since the ions are completely stripped, the most important vacuum related effect is electron capture from the residual gas and from the electron cooler. The first process has already been discussed in section 3.8; the cross-section is given by Equation (3.8.2) and the rate of the beam loss is estimated with the help of Equation (3.8.3), which can be integrated over the entire cycle to calculate the beam depletion. The electron capture from the cooler's beam is comparable with the capture from the residual gas. Again the heaviest ions demand the hardest vacuum. It is estimated that a nitrogen equivalent vacuum in the range of  $10^{-9}$  mm Hg will keep the beam loss below 3%.

### 5.7.1 The Vacuum Chamber

The variation of the guide field with time in the Decelerator is considerably slower than in the Booster. The field is constant for about 1.6 sec and then varies over a period of 0.3 sec for beam deceleration. The maximum rate of change is 13 T/s, occurring once every two seconds when the field is reset at the beginning of each accumulation cycle (see Figure 5.1.4).

The most convenient way to achieve and maintain a vacuum in the range of  $10^{-9}$  mm Hg is to employ a metallic vacuum chamber, made of either stainless steel, with a thickness of 2 millimetres. This vacuum chamber subtracts little from the vertical magnet aperture of 10 cm, and provides good electromagnetic screening of the beam from the magnet laminations. Because of the lower rate of field variation during the deceleration cycle, heating and field distortions due to eddy currents are relatively small and can be tolerated. The required level of vacuum can be achieved baking and conditioning the vacuum chamber.

As in the Booster, the vacuum chamber inside the dipole magnets is rectangular, 10 cm vertically  $\times$  15 cm horizontally; elsewhere the vacuum chamber is circular with 7 cm radius. The two vacuum chamber profiles are joined by bellows at the dipole ends.

### 5.7.2 The Vacuum Pumps and Valve System

The arrangement of the vacuum pumps, flanges etc. in the Decelerator is the same as in the Booster and is described in section 3.8.2; having the two rings the same geometry and size. The required level of vacuum can be achieved by means of the same kind of pumping components with the addition of a backing system, if needed.

## 5.8 Diagnostics and Instrumentation

The Decelerator and the Booster have the same geometry and size; the lattices are similar with the same arc configuration, differing only in the quadrupole arrangement in the long straight sections. It is thus reasonable to expect that both rings can be equipped with the same diagnostics and instrumentation, which is already described in section 3.9. To be more specific, one can opt for the same distribution of beam position monitors and closed orbit correctors, all located next to the quadrupoles and divided into two families. However, in the Decelerator, beam position monitors have a larger dynamic range, since they have to measure beam positions with a beam intensity as low as  $10^7$  heavy ions per pulse.

The components for stochastic cooling can also be valuable additions to the beam instrumentation; for fast cooling, a beam Schottky signal has also to be available.

## 5.9 Cooling Techniques

Two cooling techniques are planned for the Decelerator: electron [3] and stochastic cooling [4]. Both are needed since they have features which complement each other. Electron cooling does not depend on the beam intensity, is very effective at low energy, and affects mostly the core of the beam. Stochastic cooling works at any energy; it depends on the number of particles in the beam, and it effectively brings the tails to the centre of the distribution. Electron cooling is limited by the electron beam density and its temperature, stochastic cooling by the available electronic bandwidth and power. Electron cooling operates on the beam momentum spread and both betatron emittances at the same time; three different stochastic cooling systems are required for momentum and betatron cooling.

### 5.9.1 Cooling Requirements

The requirements for beam cooling in the Decelerator are as follows: the beam momentum spread has to be continuously reduced to make room for twelve pulses of fragments during the accumulation process. The beam momentum spread must be sufficiently small at the end of accumulation to allow it to be captured and decelerated by a reasonable amount of rf voltage. During deceleration the beam momentum changes by a factor of ten, so that momentum spread and betatron emittance will increase by the same factor; as a consequence the cooled beam must be small enough to avoid excessive growth during deceleration. Cooling may also be useful at the end of the cycle, to obtain a smaller momentum spread if required by users.

The most demanding requirements for cooling are imposed by the accumulation process. The momentum spread  $\delta$  of the stack varies according to the following equation:

$$\frac{d\delta}{dt} = -\lambda\delta + D$$

where  $\lambda$  is the cooling rate and  $D$  is the increase of 0.2% in momentum spread due to the addition of a new pulse to the stack every 100 ms. By setting the overall cooling time to 150 ms, the average momentum spread in the stack during the accumulation procedure

is maintained to 0.3%. To achieve the required cooling rate, both electron cooling and momentum stochastic cooling are required, each providing a cooling time of 0.3 sec. With a second cooling period of 0.5 sec at the same rate after the stacking cycle, the total beam momentum spread is finally reduced to about  $10^{-4}$ .

Electron cooling alone is adequate for the reduction of the beam emittance. Betatron cooling proceeds at twice the rate of momentum cooling; thus, over a period of 0.5 sec, the betatron emittance can be reduced by at least an order of magnitude. Betatron stochastic cooling is not required; it is in any case more difficult to achieve because of the bad mixing situation due to the relatively small momentum spread of the beam.

## 5.9.2 Electron Cooling

The electron cooling apparatus is located in the ring as shown in Figure 5.6.1 and has similar characteristics to the device at present operating at LNL [5]. The design is based on the following formula for the cooling rate

$$\lambda = \frac{4\pi Q^2 r_e r_p L \eta J / e}{A \beta^4 \gamma^5 \theta^3}$$

where  $r_e$  and  $r_p$  are the electron and proton classical radii [6];  $Q$  is the charge state and  $A$  the mass number of the particles being cooled;  $\eta$  is the ratio of the electron beam length to the ring circumference;  $L$  is the Coulomb logarithm;  $\beta$  and  $\gamma$  are respectively the velocity and the energy relativistic factors of the beam;  $J$  is the electron beam density

$$J = \frac{I}{\pi a^2}$$

with  $I$  the electron beam current and  $\pi a^2$  the cross-section. Finally,

$$\theta^2 = \theta_{ion}^2 + \theta_{electron}^2$$

where  $\theta_{ion}$  and  $\theta_{electron}$  are the relative velocity spreads in the ion and electron beams. For each, there are two contributions: a longitudinal one  $\theta_{\parallel}$  and a transverse one  $\theta_{\perp}$ , so that:

$$\theta^2 = \theta_{\parallel}^2 + \theta_{\perp}^2$$

Because of the high intensity of the electron beam, it is confined to the required dimensions by a solenoidal field along the entire interaction length. If the field is strong enough the trajectories of the electrons are essentially parallel lines directed along the main beam axis and the transverse divergence is effectively reduced, that is  $\theta_{\perp} \sim 0$  for the electron beam. Further, with a reasonable cathode design we can expect  $\theta_{\parallel} = 0.001$  rad. The longitudinal divergence of the ion beam is given by its momentum spread

$$\theta_{\parallel} = \frac{1}{\gamma} \frac{\Delta p}{p}$$

and the transverse one by the beam emittance

$$\theta_{\perp}^2 = \frac{\epsilon}{\beta^*}$$

where  $\beta^*$  is the value of the lattice function at the centre of the interaction region.

The parameters corresponding to a cooling time of 0.3 sec are given in Table 5.9.1. The most important condition to be satisfied is that the electron beam velocity equals in magnitude and direction the velocity of the ion beam. For instance, to cool 1 GeV/u ions, the electron energy must be about 550 keV, which is the largest so far conceived for any application. Moreover, if one considers that the beam current is 12.5 A, it is seen that the beam power is 7 MW continuous; this is a very large value which places severe constraints on the energy recovery, system which requires an efficiency of better than 99%.

### 5.9.3 Stochastic Cooling

Momentum stochastic cooling is required to operate in parallel with electron cooling. Both systems are designed for a cooling time of 0.3 sec. The components for stochastic cooling are shown schematically in Figure 5.6.1. The Schottky current signal is detected by pick-ups consisting of pair of striplines located where the dispersion is zero [7]; the signal is amplified and filtered through a device called a "notch filter": a cable with length equal to half the ring circumference, shorted at the far end. The signal then travels to the next location, half of the ring circumference away, where it is distributed equally to a system of kickers which are also made of pairs of striplines identical to the pick-ups, and are located in dispersion-free zones.

An important parameter which describes the performance of stochastic cooling is the frequency bandwidth of the electronic system. This is chosen to optimize "mixing" between pick-ups and kickers; it depends on the ring transition energy  $\gamma_t$  and on the beam momentum spread. For the ADRIA Decelerator the optimum bandwidth is 1-2 GHz, since the width of the Schottky band in the middle of this range is about half the revolution frequency, and there is overlapping between neighbouring Schottky bands at the upper end of the amplifier bandwidth.

The main parameters of the stochastic cooling system are given in Table 5.9.2. Between pick-ups and kickers there is an optional cable delay of up to 150 ns to synchronize the kicker signal with the particle arrival at the kicker. The total power requirement of 1 kW is due to the Schottky signal after amplification; thermal power due to thermal noise at the exit of the pick-ups is low and of no consequences to the cooling performance.

**Table 5.9.1: Electron Cooling Parameters**

Specific Kinetic Energy	1.0	GeV/u
$\beta$	0.88	
Mass Number	200	
Charge State	80	
Beam Emittance (rms)	3.2	$\pi$ mm mrad
Momentum Spread (rms)	0.047%	
$\beta^*$ (h,v)	17, 6	m
Length of e-beam	8	m (3%)
Coulomb Log	20	
Beam Radius	10	mm
e-beam Current	12.5	A
e-beam Current Density	4	A/cm <sup>2</sup>
$\theta$ , Total	1.33	mrاد
Cooling Time	0.3	s
e-beam Energy	0.55	keV
e-beam Power	6.9	MW
Energy Recover Eff.	99%	
Final Momentum Spread (rms)	$\pm 0.0017\%$	

**Table 5.9.2: Stochastic Cooling Parameters**

Number of Ions	$5 \cdot 10^7$	
Mass Number	200	
Charge State	80	
Specific Kinetic Energy	1.0	GeV/u
$\beta$	0.80	
Bandwith	1-2	GHz
Method	Notch Filter	
No. of Pickups	16	
No. of Kickers	32	
Schottky Power (initial)	1.0	kW
Thermal Power	negligible	
Amplifier Gain	160	dB

## References

- [1] "Feasibility Study of a Hadron Facility", Conceptual Design Report, LNL report, February 1992.
- [2] J. Griffin et al., "Time and Momentum exchange for production and collection of Intense Antiproton Beams at Fermilab", IEEE tr. on Nu. Sci., NS-30, no. 4, August 1983.
- [3] G. I. Budker and A. N. Skrinsky, Sov. Phys. Usp. 21 (1978) 277.
- [4] D. Möhl, G. Petrucci, L. Thorndahl and S. van der Meer, Phys. Rep. 58, (1980) 75.
- [5] L. Busso et al., "An Electron Cooling Device in the One MeV Energy Region", Proc. of the XIII International Conference on High Energy Accelerators, Novosibirsk 6 - 13 August 1986, Ed. A.N. Skrinsky, Publ. House Nauka 1987 (344).
- [6] T. Ogino and A.G. Ruggiero, "Theory of Electron Cooling with Magnetic Field and Space Charge", Particle Accelerators 10, (1980) 197-205.
- [7] A.G. Ruggiero and J. Simpson, "Momentum Precooling in the Debuncher Ring for the Fermilab Tevatron -I project", IEEE Trans. on Nucl. Sc., NS-30 No. 4, (1983).

# 6

## Control System

### 6.1 Control requirements

A first approach to the control system design should concentrate on the definition of the basic functional tasks; a schematic, bottom-to-top, classification could be the following:

- a. Physical Device Control;
- b. Control Interconnect;
- c. Data Base Management;
- d. Operator interface.

The Physical Device Control is performed by a large number of specific controllers or processors that directly interact with the accelerator components; the hardware implementation is strongly dependent on the device's characteristics, in terms of input/output requirements and response-time constraints.

Concerning with the Control Interconnect, a certain number of computers must be dedicated to collect and route data to/from the low-level device controllers. These computers must be linked together through a high speed network; multiple network levels can be used to provide the system with fault tolerance capability, and to improve the overall performance by means of a more efficient distribution of data traffic.

In the Data Base Management function many types of data need to be handled. One class is constituted by the data directly related to the operation of device control processors, i.e. device calibration tables, settings of trip points for monitored parameters, etc.; another class is made by data concerning with the beam optics and accelerator tuning. The control system must also periodically record all significant machine parameters, in particular those related to exceptional events like alarms, etc.

The Operator Interface function has to provide a set of graphical facilities for the setting and monitoring of each accelerator component. Physically, the operator interface is implemented by means of graphic workstations placed in the control room, and a certain number of remote consoles for maintenance purposes.

Among the accelerator control tasks, a special emphasis must be given to the beam transport control, as it involves a large quantity of critical functions (synchronization with

the Linac injection, beam extraction timing, beam cooling, etc.). For this purpose an adequate set of hardware and software tools must be provided, including off-line simulation and on-line diagnostics.

There are other aspects in the accelerator control development that must be taken into account, even if they are not directly involved in beam production. A very important example is the fault diagnosis and equipment protection system; this term indicates a set of utilities designed to detect a malfunction of a device or a subsystem, and disable its operation to avoid possible damage propagation. An adequate level of redundancy in the control system equipment should in many cases allow the accelerator to recover from a failure without interrupting the operation.

The complexity of the tasks to be carried out makes necessary to have the possibility of simulating the operation of all the accelerator components, either in the normal or in a fault condition. For this reason it is important to foresee a Development Support Structure, in which Software Engineering tools, including Artificial Intelligence techniques, will be widely used to define and test behavioral models of all the accelerator subsystems.

## 6.2 System implementation

The above considerations are purely functional and do not imply any direct constraint on hardware implementation; in any case it is evident that a highly distributed architecture is the only practical solution to meet the different requirements of a very large number of devices. The high-level components of the control system should be isolated as much as possible from details of the low-level devices; this is possible only if each device, or group of devices, has an intelligent controller associated with it.

The Figure 6.2.1 shows a possible architecture of the control system. At the highest level there are the workstations dedicated to the Operator Interface function; at the same level one computer should operate as file server to provide a centralized Data Base Management function. These machines should be linked, through bridges, by one side to a central computing facility for beam dynamics calculations and simulation and, by the other side, to the Control Interconnect network.

At the second level there are the computers dedicated to physically implement the Control Interconnect; each accelerator ring will have its own network. These computers could be VME based machines, without mass storage devices, and should be loaded with a real-time operating system; the link will be based on optical fiber technology.

At the lower level there are the device controllers, directly operating on the accelerator hardware. Such controllers will be of different types, depending on the complexity of the task to be carried out. For a simple application (i.e., temperature monitoring or vacuum read-out) an intelligent controller linked through a RS-232 interface will be sufficient for the purpose. In other cases, when the number of I/O channels is very high, an entire VME crate - or even multiple crates linked through a vertical bus - will be filled with interface boards.

The hardware choice is strictly related to the development of electronics technology. As already mentioned, the popular VME standard still seems to be the most suitable solution because of its flexibility and the availability on the market of high performance boards. For

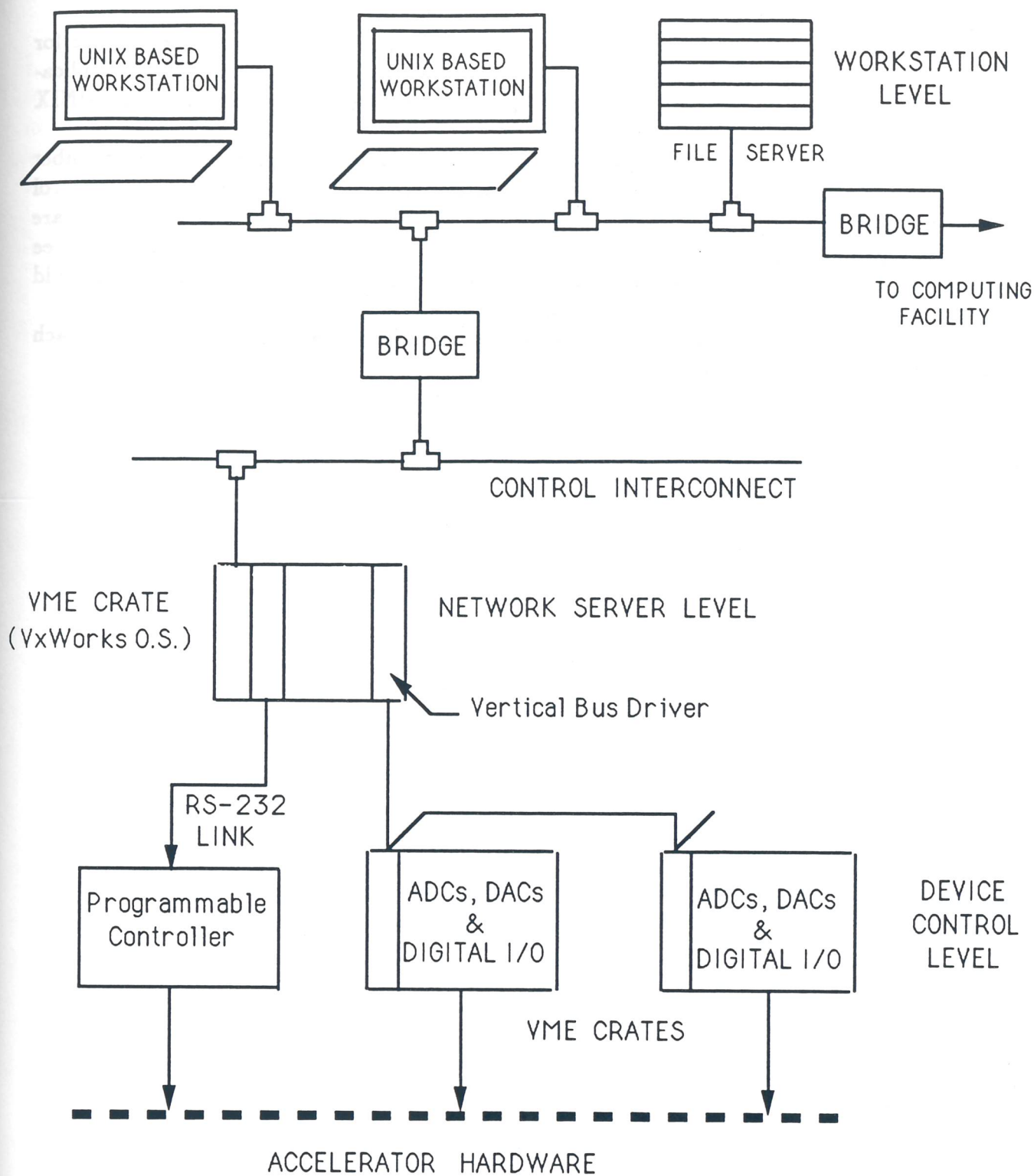


Figure 6.2.1 Control System Architecture

the control interconnect, the 100 Mbit/s FDDI LAN seems to be the most attractive for the network implementation.

Concerning with the software, UNIX and X-windows are an almost obliged choice for the workstations; for the Control Interconnect computers, and for the real time applications, VxWorks seems a good candidate because of its natural integration in the UNIX environment.

To define the size of the control system for the ADRIA complex the total number of control channels can be evaluated by comparison with existing machines. A control channel can be defined as an independent way to execute a simple action on a hardware element. This means that a simple device such as a power supply, which needs at least three control channels (a status command, and setting values in control and acquisition), should be accounted for four channels, allowing one for redundancy.

Following the above considerations we can foresee about 5000 control channels for each ring and 2000 for the transfer line between them.

# 7

## Civil Engineering

The ADRIA complex is planned to be located in the south-west side area of the Legnaro Laboratory ( Figure 1.1.2 ). Because of radiation protection considerations, the Booster and the Decelerator beams axis are at 3.8 and 1.3 metres underground, respectively. An adequate tunnel is required to house the ADRIA complex. The experimental area is located at the north side of ADRIA. The utilities plants like the electrical and the hydraulic ones are located in a building at the center of the rings and in containers located around it.

### 7.1 Tunnel Enclosure

All the ADRIA components, from the ALPI post-accelerator exit to the experimental area, are housed in a 5 metres underground tunnel. The tunnel develops a total length of about 500 metres, as shown in Figure 7.1.1. In the transfer lines and in the bending section the tunnel is 4 metres large, while in the straight section regions is 8 metres large to allow the installation of several devices like injection/extraction systems, rf cavities, electron cooling system etc. The tunnel cross-section is shown in Figure 7.1.2. Both rings are housed in the same tunnel, one on top of the other and the ground floor have to support 10 ton/m<sup>2</sup> For radiation protection considerations the tunnel is shielded by 3 metres of earth.

### 7.2 Experimental Area

The experimental area covers about 2400 square metres and is 11 metres high. Its location is at the north side of the ADRIA complex. The ground floor of the building is also 5 metres underground, as for the tunnel. In this building several beam lines for high and low energy experiments will find place. Electron, muon and pion test beams also will be located in the same area. The building will be equipped with suitable services as electrical power, water cooling, compressed air, crane,..... Data acquisition and control rooms also will find place in the same building.

## 7.3 Utilities

The utilities for both ADRIA complex and experimental area are placed in a building at the center of the rings (see Figure 7.1.1). This building develops 600 square metres surface and 6 metres high. Utilities like water refrigerators and electrical cabins will be installed in containers located around it. The building itself will be divided into two parts, respectively the one for electrical plant ( magnet power supplies ect. ) and the one for the hydraulics plant.

### 7.3.1 Power Requirements

The demands of electrical power are summarized in Table 7.3.1.

**Table 7.3.1: Cooling Plant Parameters.**

ITL Transfer Line	0.5	MVA
Booster		
Dipoles + Quads	1.8	
Injection/Extraction Kickers	0.25	
RF Cavities	0.8	
Instrumentation	0.3	
ISL Line	1.0	
Decelerator		
Dipoles + Quads	3.0	
Injection/Extraction Kickers	0.25	
RF Cavities	0.8	
E-cooling	0.5	
Refrigerators + General Services	5.0	
Total		13.85 MVA

Four electrical cabins of 3.5 MVA each, for a total of 14 MVA, will be installed in containers and located around the Service Building at the center of the ADRIA rings. Two generator groups of 2 MVA each have to be installed in the Service Building.

### 7.3.2 Hydraulic Plant

To cool the ADRIA components ( bending magnets, quadrupoles, rf cavities, deflector magnets and related power suppliers ) a plant with characteristics described in Table 7.3.2 is proposed.

**Table 7.3.2: Cooling Plant Parameters.**

Temperature of Circulating Water	22-23	°C
Flow	150	mc/h
Maximum Pressure	12	bar
Refrigerating Power	8.5	MFrig/h
pH	7	
Inlet Conductivity	<1	μS/m

The de-ionized water production plant will be housed in the Service Building, while water refrigerators can be installed in special containers.

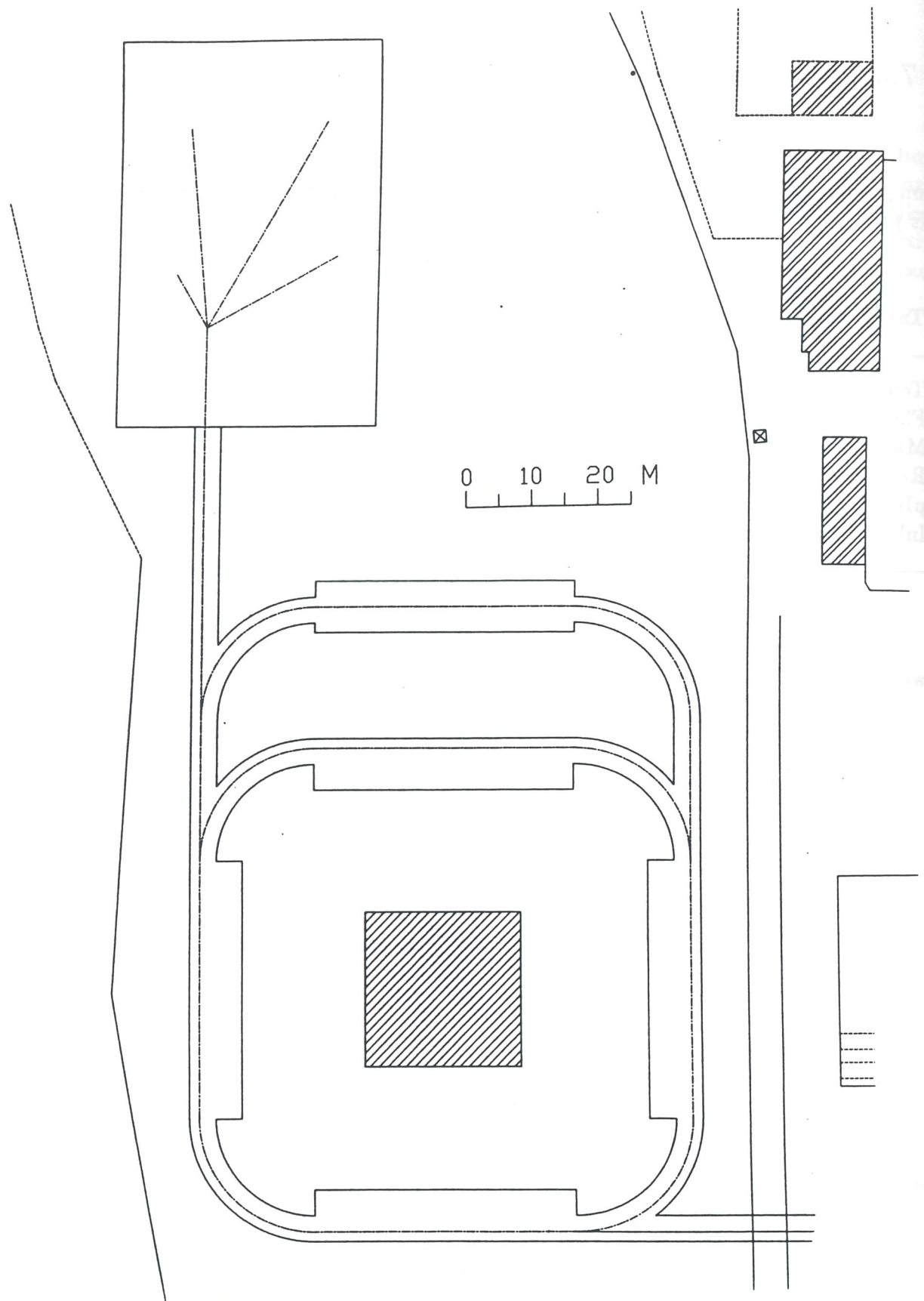


Figure 7.1.1: Tunnel and Buildings for the ADRIA Complex

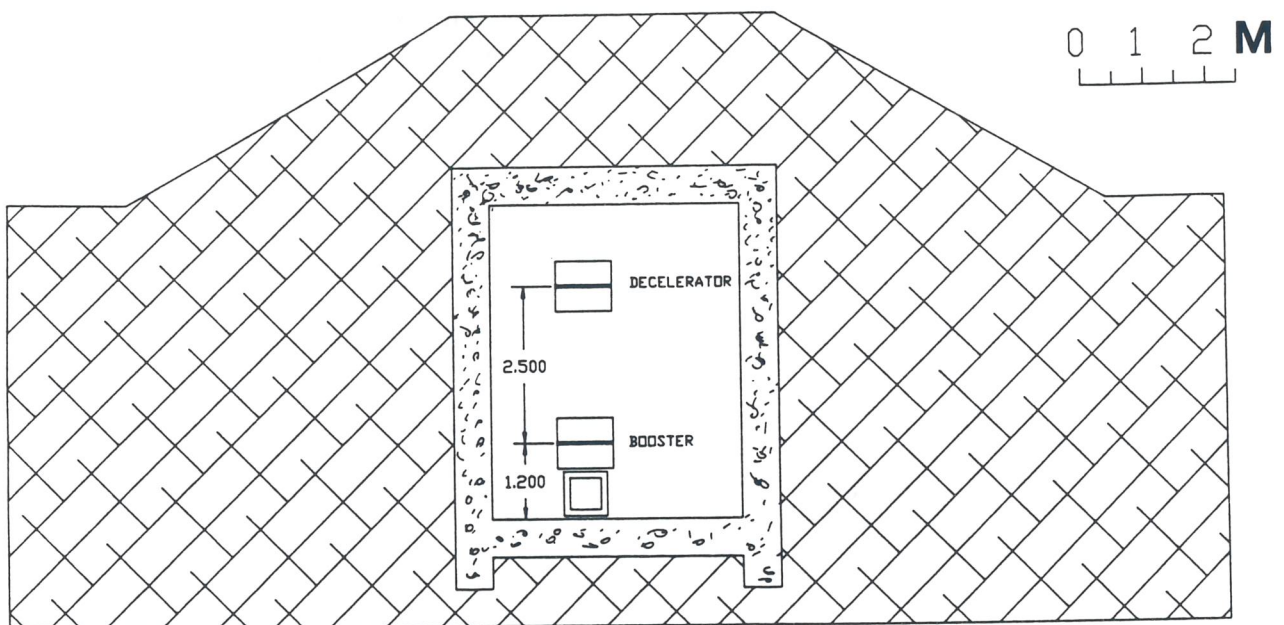


Figure 7.1.2: Tunnel Cross-section and Arrangement of the Rings

# 8

## Radiation Protection

The main constraints on Radiation Protection for the ADRIA complex are determined by the heavy ion beams with specific energies in the GeV/u range and intensities in excess of  $10^{12}$  ions/s. It is clear that the acceleration of such high intensity heavy ion beams sets stringent constraints on all Radiation Protection items.

A preliminary analysis on the Radiation Protection can be carried out by taking into account the three classical main items, i.e. Active Shielding, Induced Radioactivity and Radiation Damage.

### 8.1 Active Shielding

An approximate evaluation of the Active Shielding can be based on the following assumptions:

- In the worst possible accident, up to 2 pulses of  $2 \times 10^{11}$  ions at the maximum energy of 1 GeV/u may be lost before the aborting of the acceleration cycle;
- Short term local losses at any place in the ring, due to the tuning, may reach values of the order of  $10^{-2}$  of the beam.
- Continuous losses of the order of  $10^{-5}$  of the beam intensity in each metre of the vacuum chamber and of the order of  $10^{-2}$  at some localized place, i. e. on a dedicated scraper in the injection section or on a septum magnet at the extraction;
- The maximum dose rate at the surface must be limited to  $10^{-2}$  mSv/h or to  $10^{-2}$  mSv per accidental event.

The concrete thickness necessary to shield the accelerator housing has been modelled by J.B. McCaslin et al. [1]. The Dose Equivalent for the angle  $\theta$  between the beam axis and the point of interest is given by the following semi-empirical equations:

for  $0^\circ < \theta < 20^\circ$

$$H(\theta) = 12.0 \times 10^{-12} N e^{-0.20 \theta} r^{-2} e^{-l^*(\theta)/\lambda^*} \quad (Sv) \quad (8.1.1)$$

for  $20^\circ < \theta < 120^\circ$

$$H(\theta) = 0.48 \times 10^{-12} N e^{-0.038 \theta} r^{-2} e^{-l^*(\theta)/\lambda^*} \quad (Sv) \quad (8.1.2)$$

H is the Dose Equivalent in Sv, r is the distance from the target (on the beam axis) to the point of interest in metres, N is the number of ions stopped in a target,  $l^*(\theta)$  is the shield thickness in the direction  $\theta$  in  $\text{g cm}^{-2}$  and  $\lambda^*(\theta)$ , the attenuation length for concrete in  $\text{g cm}^{-2}$ , is given by:

$$\theta < 75^\circ \quad \lambda^*(\theta) = 115.0 e^{-0.01\theta} \text{ g cm}^{-2} \quad (8.1.3)$$

$$\theta > 75^\circ \quad \lambda^*(\theta) = 55.0 \text{ g cm}^{-2} \quad (8.1.4)$$

For the loss of 2 pulses ( $2 \times 10^{11}$  ions) on a single spot, the Dose Equivalent has a maximum at  $\theta = 50^\circ$ . The required concrete shield thickness needed to reduce the Dose Equivalent 8 metres far from the beam axis to  $10^{-2}$  mSv per accident event is 60 cm.

For short term local losses, of the order of  $10^{-2}$  of the beam, at any place in the ring, the Dose Equivalent rate has a maximum at  $\theta = 60^\circ$ . The required concrete shield thickness needed to reduce the Dose Equivalent Rate 8 metres far from the beam axis to  $10^{-2}$  mSv/h is 180 cm.

Continuous losses at of  $10^{-2}$  of the beam produce the maximal Dose Equivalent rate at  $\theta = 60^\circ$ . The required concrete shield thickness needed to reduce the Dose Equivalent Rate 8 metres far from the beam axis to  $10^{-2}$  mSv/h is 180 cm.

Active shielding will be of paramount importance in the Fragment Production Area, where the primary beam of heavy ions hits the target with a current of  $10^{12}$  ions/s. For the complete beam lost and the Dose Equivalent Rate of  $10^{-2}$  mSv/h 8 metres far from the beam axis in the lateral direction the concrete thickness is 290 cm, and in the forward direction the required thickness is 880 cm.

Concerning the radiation shielding, the beam stop is the main radiation source. Considering 5-10% of the beam to be converted into fragments in the target and assuming a beam intensity of  $10^{11}$  ions/s, as reported in the internal GSI proposal protocol, for Ne of energy of 1 GeV/u stopped in Fe, roughly  $10^{12}$  neutrons in the energy range of 50-500 MeV are produced. Due to the long free path ( $\sim 46$  cm for concrete and  $\sim 18$  cm for iron), and the angular distribution (peaked in the forward angles and exponential decreament at larger angles), about 6 m thick concrete wall is recommendable in the forward direction.

Roof shielding of target area will be dictated by skyshine radiation. The Dose Equivalent Rate of  $10^{-3}$  mSv/h can be taken as a limiting value outside the laboratory fences at about 1 Km (the only data available) from the source. Using semi-empirical model as described in ref. [2] the source term comes out to be about 20 fSv/h per 1 neutron/ $\text{m}^2$ . For a roof area of  $100 \text{ m}^2$  the Dose Equivalent Rate outside it will be 0.2 Sv/h. However, this level should be reduced by about two order of magnitude as shown by experience at PSI. A roof shielding of about 170 cm is good enough to reduce the Dose Equivalent Rate to 2 mSv/h at the top of the roof and just outside the shielding.

## 8.2 Induced Radioactivity

The lateral neutron dose attenuation length is identical to the proton value for heavy ion beams, nevertheless, heavy ion reactions yield much more neutrons than proton interactions at the same specific ion energy [3,4]. Regarding radiation protection, this means that at the same specific ion energy and identical beam intensity, a GeV heavy ion accelerators

requires more shielding than a proton machine. Whereas for Proton accelerators numerous semiempirical calculations of shielding against neutrons exist, negligible few comparable data exist for heavy ion machines.

The target handling might results in extra radiation problems, since the low energetic target fragments are stopped in the target itself. However, for light particles with  $Z \leq 11$ , e.g. beryllium or carbon, no radioactive isotopes are produced with half lives between hours and years, except  $^7\text{Be}$ . In fact, light targets yield the highest production rates of projectile fragments and are thus preferable. The materials, which show the lowest activation, could possibly be utilized in the target area and in the beam stop.

After the irradiation of the target, the activity could reach as far as  $10^8$  to  $10^9$  Bq. Experimental data coming from GSI experience show that, for Ne with a beam intensity of  $10^9$  ions/s and energy of 1.2 GeV/u, exposure near the target is about 500  $\mu\text{Sv/h}$ . Also other parts of the accelerator not expected to be activated showed exposures up to 100  $\mu\text{Sv/h}$ . This because of the large beam loss rates along the accelerator. In view of the residual radioactivation problems that accrue from relatively low fractional beam loss rates, good beam diagnostics and spill control will be a requirement for the ADRIA facility.

The target zone find itself under standing-air (air-activation). A further activation problem is activation of concrete wall (Na). Marble (essentially pure calcite  $\text{CaCO}_3$ ) could be used to shields parts becoming radioactive under neutron bombardment. Although the major part of the activity is within solid materials, cooling water systems surrounding targets and beam stops also suffer considerable induced radioactivity. The activity in the cooling water systems can be controlled by passing part of the circulating water through deionization columns. In case of leaks, a drain system must be provided.

## 8.3 Radiation Damage

According to previous empirical calculations [2,3,4] beams line components are supposed to be exposed to dose rates ranging from few Gy/h upto  $10^5$  Gy/h, depending on continuous or full beam loss respectively, during the operation of the machine. Continuous losses of the order of  $10^{-5}$  of the beam per metre of the vacuum chamber, and local losses of the order of  $10^{-2}$  can be lethal for conventional installations. The local shielding, as described above, also play important role in reducing the radiation damage. They will reduce the radiation dose rate in surrounding components (cable, electronics, etc.) inside the accelerator tunnel to about  $10^5$  Gy in 10 years of operation (5000 h/year). Special care has to be taken for the components at the fragmentation part. In particular the magnets downstream of the production target and the profiled degrader (see chapter 4) have to be shielded from the radiation source. Further, magnet coils in the high radiation regions have to be made with mineral insulated cable.

## 8.4 Other Risks

Dedicated studies must be devoted to the understanding of correlated risks of activation such as:

- Cooling Water activation
- Soil/Ground Water activation
- Air activation

Due to the possible induced radioactivity of the cooling systems for primary target and other irradiated components, modest local shielding (max up to 1 m concrete) might be required. The activity of fast-neutron irradiated cooling water is caused principally through the production of  $^7\text{Be}$  ( $T_{1/2} = 53$  d) with a cross-section of  $\sim 5$  mb.

Radioactivity produced in earth and ground-water can represent few percent of total radioactivity produced by high intensity accelerator [2]. In particular soil/ground-water activation can be an important item to study, since the peculiar geological and hydrological aspects of the site of Legnaro and the respective elevated underground water level demands careful attention to these facts. According to Weisse [4], anyway, radiation exposure of the public due to activated ground water was found to be of no concern. Concerning the air activation produced by short lifetime isotopes coming out from the interaction of primary and secondary particles directly with constituent target nuclei of the air, only a few gaseous radionuclides are of radiological importance. The most important reactions and their effective cross sections are summarized in Table 8.4.1 for  $\sigma_{eff} (\geq 15 \text{ MeV})$  [4]. Because of the production of these radionuclides a closed circuit of air refilling must be foreseen.

**Table 8.4.1: Effective cross sections (mbarn) of some relevant radionuclides.**

Projectile Fragment ( $T_{1/2}$ )	Air Target nuclide		
	$^{14}\text{N}$	$^{16}\text{O}$	$^{40}\text{Ar}$
$^7\text{Be}$ (53.3 d)	2.9	2.5	-
$^{11}\text{C}$ (20.4 min)	16.0	8.2	-
$^{13}\text{N}$ (9.96 min)	17.0	3.4	-
$^{15}\text{O}$ (2.03 min)	-	34.0	-
$^{41}\text{Ar}$ (1.83 h)	-	-	660

## References

- [1] J. B. McCaslin, P. R. LaPlant, A. R. Smith, "Neutron production by Ne and Si ions on a thick Cu target at 670 MeV/u with application to radiation protection", IEEE Trans. Nucl. Sci. NS-32 No. 5 (1985) 3104-3106.
- [2] R. H. Thomas and G. R. Stevenson, "Radiological safety aspects of the operation of proton accelerators", International Atomic Energy Agency, Vienna, 1988.
- [3] H. P. Weise, "Shielding of High Energy Heavy Ion Accelerators", Proceeding of the 20th Midyear Topical Symposium of the Health Physics Society on "Health Physics of Radiation Generating Machines", Reno, Nevada, Feb. 8-12, 1987, pp. 459-465.
- [4] H.P. Weise, "Shielding of high Energy Heavy Ion Accelerators", Proceedings of 7th International Conference on Radiation Shielding, Bournemouth, U.K., Sept. 12-16, 1988, pp. 903-911.

# 9

## Cost Estimate and Schedule

### 9.1 Cost Estimate for the ADRIA Proposal

The conceptual design described in this report is adequate to provide a baseline for a cost estimate of the project. The estimate is also based on comparisons with similar projects, notably the 1.5 GeV AGS Booster at Brookhaven National Laboratory and the Fermilab Booster. In particular, the cost estimate of the rf system, which is a crucial component of the proposal, is drawn from experience with the rf system of the Fermilab Booster, as well as from recent developments for the Superconducting Super Collider injectors, from the TRIUMF II and LAMPF II proposals. Finally, experience gained in the design and construction of the ALPI post-accelerator has also been useful for the estimation of the cost of many components, in particular the Ion Transfer Line joining the ALPI injector to the ADRIA Booster.

Four main technical components constitute the ADRIA proposal, namely the Ion Transfer Line (ITL) between ALPI and the Booster, the Booster itself, the Transfer Line between the two rings, and the Decelerator. The detailed costs estimate of the main components are shown in Tables 9.1.1-4 and summarized in Table 9.1.5. It is assumed that the project is developed in three phases. During the first phase, most of the civil engineering, plants and enclosures is built together with the Transfer Line between ALPI and Booster, the Booster itself and half of the Transfer Line between the two rings, including targeting and selection of unstable isotopes. The second phase follows with the completion of the Transfer Line itself and the installation of the Decelerator. In the final, third phase electron cooling is added to the facility. The total cost is 66.6 billion Italian Lire in 1992 estimate, of which 42.6 billion Lire are required for the completion of the first phase, 19.0 for the second phase and 5.0 for the addition of the electron cooling. During the first phase, the cost of civil engineering ( items E. to H. ) add to 19.1 billion Lire, about 45% of the cost of the first phase; it provides a good investment for the subsequent phases.

**Table 9.1.1: Cost Breakdown of the Ion Transport Line (ITL)**

Magnets:	0.2	GLit
Power Supply	0.1	
Vacuum	0.3	
Diagnostics	0.1	
ITL Total	0.7	GLit

**Table 9.1.2: Cost Breakdown of the Booster**

Magnets:	32 dipoles	7.0	GLit
	48 quadrupoles		
	48 steering dipoles		
Power Supply		3.0	
Injection/Extraction		0.8	
Vacuum		2.3	
Diagnostics		1.0	
RF System:	6 cavities LFRF	3.0	
	6 cavities HFRF		
Booster Total		17.1	GLit

**Table 9.1.3: Cost Breakdown of the Transfer Line (ISL)**

Magnets:	18 dipoles	2.3	GLit
	34 quadrupoles		
	34 steering dipoles		
Power Supply		0.5	
Targetry		0.2	
Vacuum		0.5	
Diagnostics		0.2	
ISL Total		3.7	GLit

**Table 9.1.4: Cost Breakdown of the Decelerator**

Magnets:	32 dipoles	7.0	GLit
	52 quadrupoles		
	52 steering dipoles		
Power Supply		1.2	
Injection/Extraction		0.8	
Vacuum		2.3	
Diagnostics		1.0	
RF System:	2 cavities Bunch rot.	2.0	
	2 cavities RF stack.		
	4 cavities Deceler.		
Stochastic Cooling		1.0	
Decelerator Total		15.3	GLit

**Table 9.1.5: Total Cost of the ADRIA Proposal**

<b>First Phase</b>		
A. ITL	0.7	
B. Booster	17.1	
C. Transfer Line (for targetry only)	3.7	
D. Control System	2.0	
Technical Components, First Phase		23.5 GLit
E. Tunnel Enclosure	5.0	
F. Utility Building	0.6	
G. Experimental Area	3.5	
H. Engineering Plant	10.0	
Sub-total E to H		19.1 GLit
Total of First Phase		42.6 GLit
<b>Second Phase</b>		
I. Decelerator	15.3	
L. Completion of Transfer Line	3.7	
Total of Second Phase		19.0 GLit
<b>Third Phase</b>		
M. Electron Cooling	5.0	
Total Cost of the Project		66.6 GLit

## 9.2 Construction Time Schedule

The scale of the project is such that the first phase can be built over four-year period. It is proposed that construction begins January 1995, with the schedule shown in Figure 9.2.1. The funding profile, shown in Figure 9.2.2, is expected to peak in 1996. This profile is valid as long as it is supported by a Research and Development program with a cost also shown in Figure 9.2.2. Commissioning of the complex would begin in January 1998, followed by operation in the middle of the same year. At the end of the construction period the operational funding should be assigned to the project.

By 1993 the ALPI project will have begun operations, and the present scientific and technical staff of the Laboratori Nazionali di Legnaro will then have acquired valuable experience with the design, construction and commissioning of the ALPI post-accelerator.

## 9.3 Accelerator R&D Program

A program of Research and Development is required to reduce the number of options, to freeze the design, to assess the hardware capability and to resolve performance issues. About three years of R&D is expected to be necessary for the ADRIA project. This could begin a year before the start of construction, i.e. in 1994, and it could overlap the initial two years of construction, which is devoted to civil engineering and the installation of established components. The funding required is shown in Figure 9.2.2 and amounts to about 2.5 GLit for the first and the last year and to 3 GLit for the year 1995.

The areas of uncertainty which require additional studies have been identified and are shown in Figure 9.3.1.

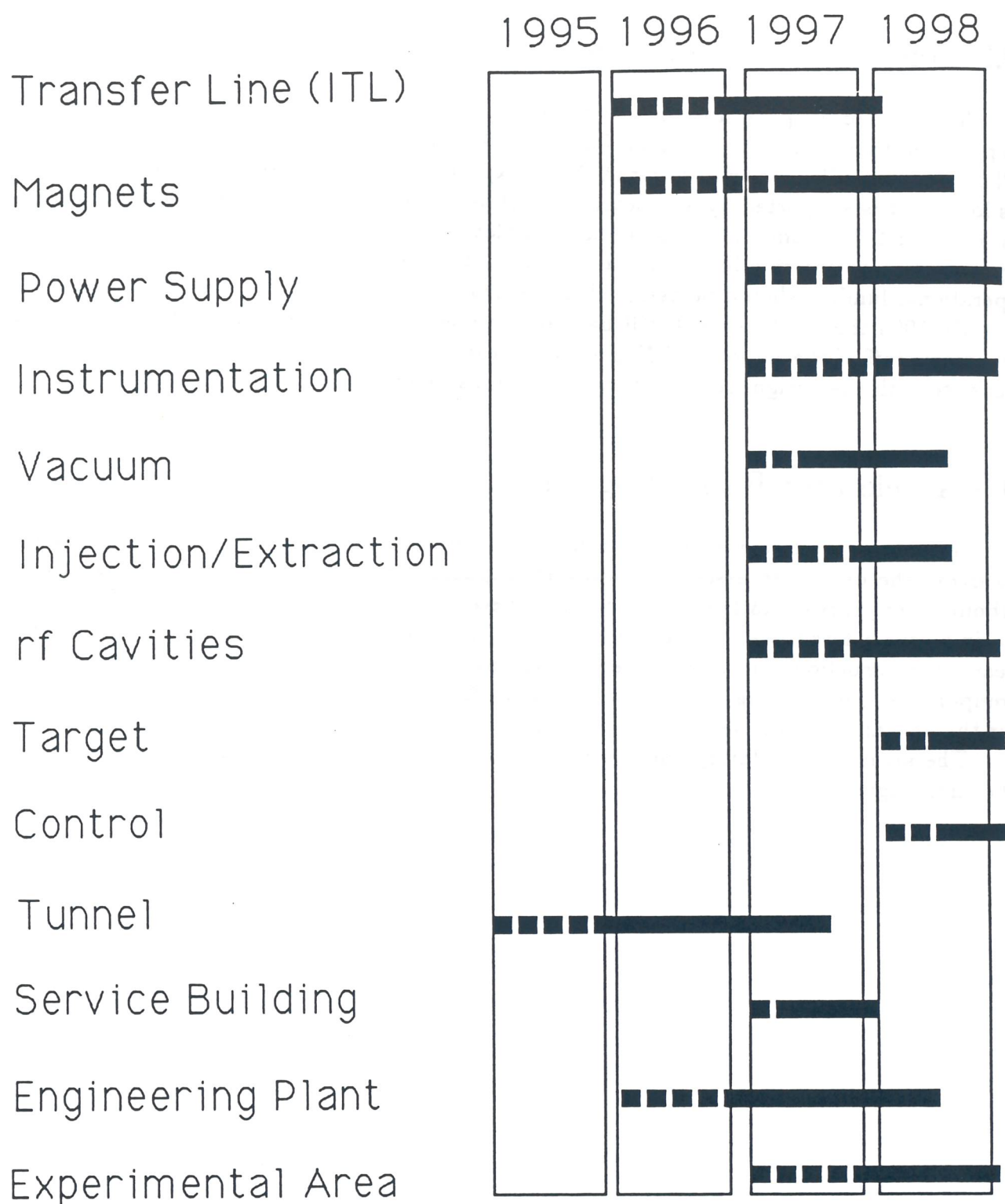


Figure 9.2.1: Construction Schedule of the ADRIA Complex.

GLit

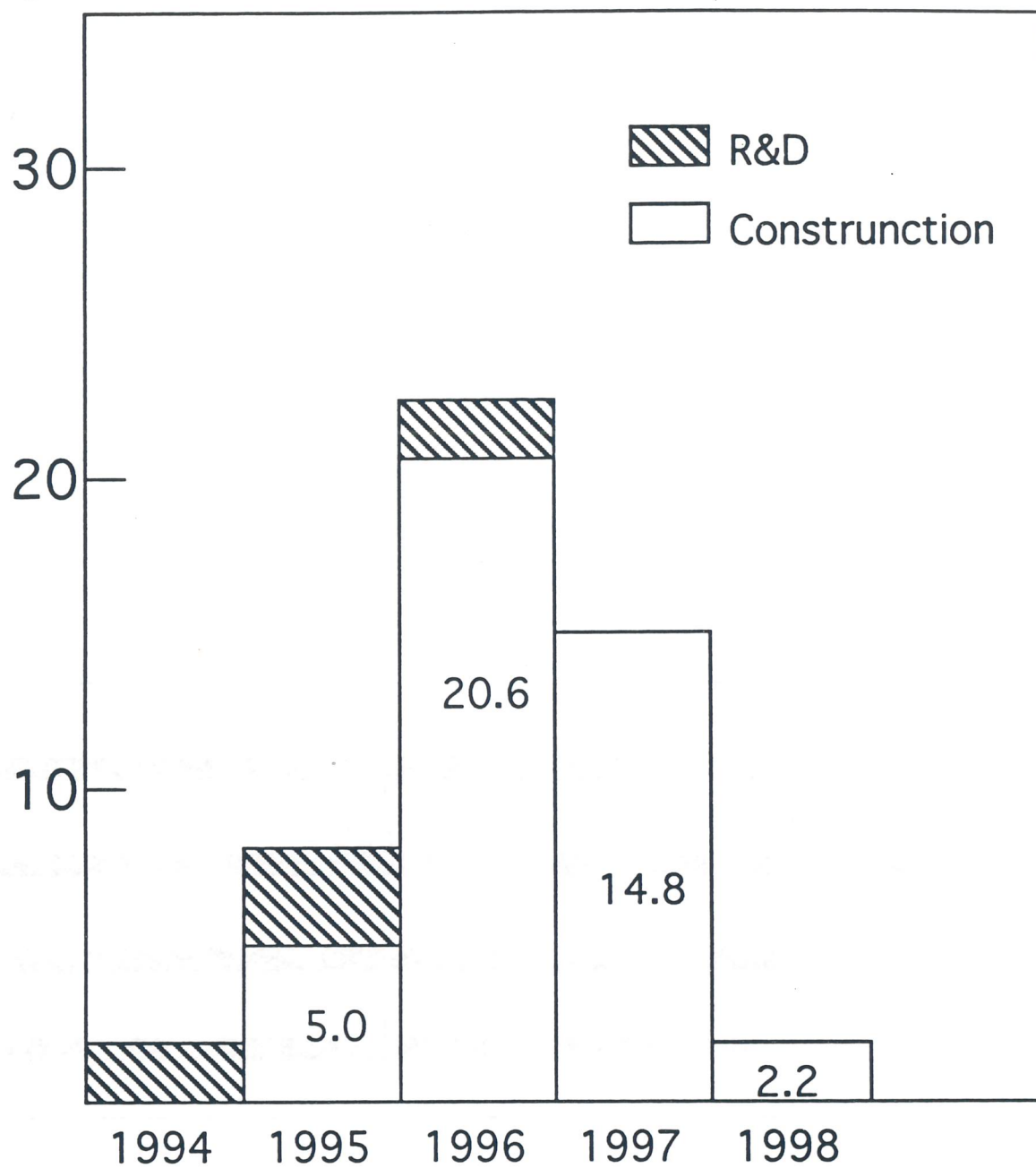


Figure 9.2.2: Funding Distribution for Construction of the ADRIA Complex.

## R&D Schedule and Costs [ Glit]

	1994	1995	1996
Design Finalization	0.5	0.5	0.5
Magnet, Power Supply, Vacuum	0.5	1.0	0.5
rf Cavity System	1.5	1.0	1.0
Beam Transfer Line & Targetry	—	0.5	0.5
Total per Year	2.5	3.0	2.5

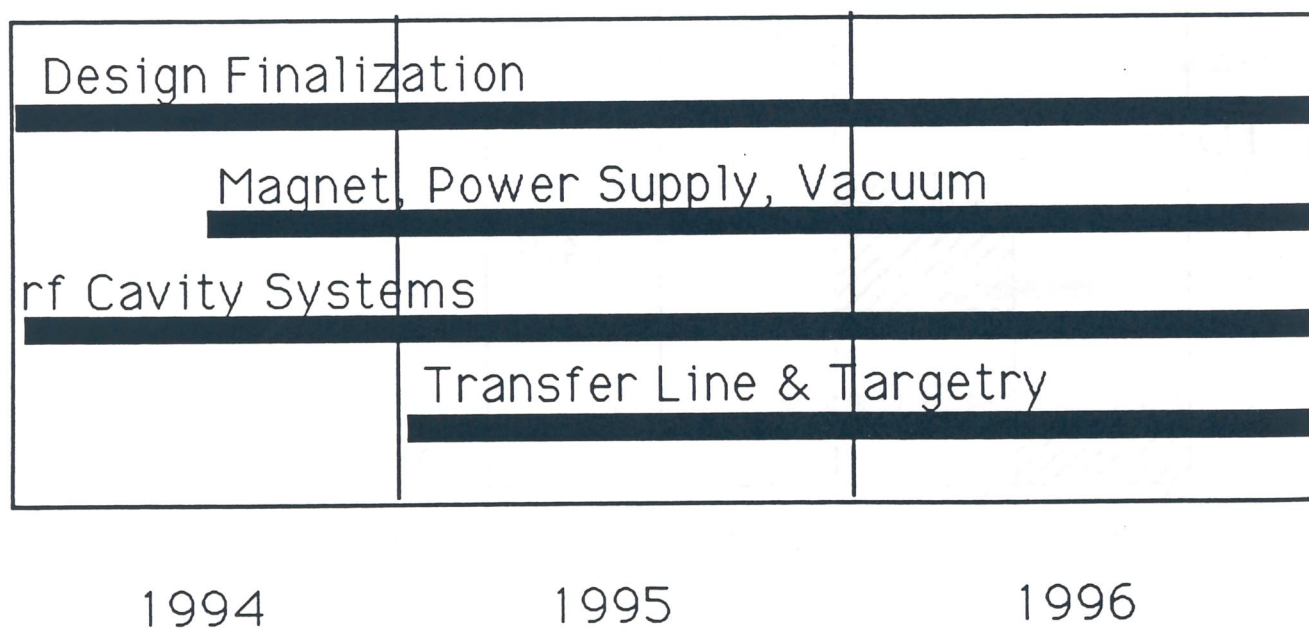


Figure 9.3.1: R&D Schedule and Costs.

## Appendix

### Acceleration of Protons

There is considerable interest in the acceleration of beams of protons in the ADRIA facility described in this report. This is indeed possible with modifications and additions that do not alter the main function of the complex to accelerate and accumulate heavy ions. A study was also performed to demonstrate feasibility and compatibility of proton acceleration in ADRIA [1]. Polarized protons can also be accelerated in the Booster.

The following is needed to accelerate protons: a 211 MeV proton linac as the injector, modifications of the rf system and a proton injection system. Protons are injected and accelerated in the Booster with the same repetition rate of 10 Hz. The final kinetic energy at extraction will be 5.8 GeV, corresponding to the unchanged maximum rigidity of 22.25 Tm. The number of protons being accelerated is  $5 \times 10^{12}$  per pulse, corresponding to the average current of 8  $\mu$ A in output. A summary of the proton beam parameters is given in Table A.1.

The design of the proton linac was thoroughly studied by an international group of experts; the technical findings can be found in the forementioned report; the project was found interely feasible and can be eventually build with a wider collaboration with other foreign institutions.

The rf system for the acceleration of protons has to cover the range from 30 to 56 MHz. This will require modification of the design of the second rf cavity system for heavy ions to cover the range from 30 to 50 MHz, and the addition of four more cavities of this type. A third rf system has to be added, just for the acceleration of protons, in the range from 50 to 56 MHz. The entire rf system capable to accelerate both heavy ions and protons is described in Ref.[1].

To inject protons in the Booster, an independent system is required, also described in Ref.[1]. Injection takes place according to the charge-exchange method where negative ions are stripped of their electrons by traversing a thin carbon foil. Extraction of protons can use the same magnet components of the heavy ion beams.

It is also possible to accelerate protons at a larger repetition rate and to a lower kinetic energy: for instance 1.2 GeV at 50 Hz. This mode will provide also a larger average intensity, that is 40  $\mu$ A, which can be injected in a subsequent larger accelerator or can be used as

a neutron spallation facility. Intense proton beams can also be used to impinge a target for the production of unstable isotopes by the method of Isotope Separator On-Line. This mode of operation will require a modified power supply system for the magnets; essentially, the excitation current will have to switch to a new capacitor bank for cycling at 50 Hz. The magnets of the Booster have a lamination thin enough to be cycled also at 50 Hz.

In the proton cycle the Decelerator can be used as a Stretcher where the proton beam is transferred to and let to debunch. The beam is then extracted with a slow spill of 100 % duty cycle over a period of time equaling the repetition period of the Booster. The components for the slow resonant extraction are to be added.

It is also possible in a subsequent phase to upgrade the Proton Linac to an energy of 535 MeV. This will allow an increase of the average current to  $88 \mu\text{A}$ , corresponding to  $1.1 \times 10^{13}$  protons per cycle. Radiation shielding will need then to be upgraded.

The acceleration of protons is a feature that can be included at the start of the project or included later in a second phase. It is also possible to stimulate interest in Europe to create conditions for an international collaboration in the development of the project. The cost estimate for the inclusion of the acceleration of protons is summarized in Table A.2, in 1992 value of Italian Lire.

## Reference

- [1] "Feasibility Study of a Hadron Facility", Conceptual Design Report, edited by LNL, February 1992.

**Table A.1: General Parameters for Proton Acceleration.**

Repetition Rate	10	50	Hz
Injection Energy	211	211	MeV
Extraction Energy	5.8	1.2	GeV
Number of Protons per Cycle	$5 \times 10^{12}$	$5 \times 10^{12}$	
Average Current	8	40	$\mu\text{A}$
Space-Charge Tune-Shift	0.2	0.2	
Harmonic Number	50	50	
rf Frequency	30-56	30-51	MHz
rf Voltage	330	520	kVolt
Normalized Emittance	25	25	$\pi$ mm-mrad
Bunch Area	0.05	0.05	eV-s

**Table A.2: Additional Cost for Acceleration of Protons.**

Proton Linac (211 MeV)	25.0	GLit
50 Hz Power Supply	1.0	
RF System	1.5	
Injection/Extraction	1.5	
Transfer Lines Modifications	0.5	
Total	29.5	GLit

